UPPSALA
UNIVERSITET

Digital Comprehensive Summaries of Uppsala Dissertations from the Faculty of Science and Technology 1993

Criticality of fast failures in the High Luminosity Large Hadron Collider

BJÖRN LINDSTRÖM

ACTA
UNIVERSITATIS
UPSALIENSIS
UPPSALA
2020

ISSN 1651-6214
ISBN 978-91-513-1081-7
urn:nbn:se:uu:diva-426416

Dissertation presented at Uppsala University to be publicly examined in Siegbahnsalen, Ångströmlaboratoriet, Lägerhyddsvägen 1, Uppsala, Wednesday, 27 January 2021 at 13:00 for the degree of Doctor of Philosophy. The examination will be conducted in English. Faculty examiner: Dr. Annika Nordt (ESS - European spallation source).

Abstract
Lindström, B. 2020. Criticality of fast failures in the High Luminosity Large Hadron Collider. *Digital Comprehensive Summaries of Uppsala Dissertations from the Faculty of Science and Technology* 1993. 115 pp. Uppsala: Acta Universitatis Upsaliensis. ISBN 978-91-513-1081-7.

Each of the two Large Hadron Collider (LHC) beams contain 362 MJ of energy. This will be further increased to 678 MJ in the upcoming upgrade to the High Luminosity LHC (HL-LHC). In the event of an uncontrolled beam loss, a significant hazard occurs, that can damage the machine components. This thesis is focused on failures that can lead to a fast increase of beam losses, with a focus on the new optics and equipment in the HL-LHC. The criticality for a number of failure scenarios is studied, under different optics configurations of the machine. Mitigation strategies, involving dedicated interlocking and a reduction of the impact that the failures have on the beam are proposed for the most critical scenarios. For a number of less critical failures it is determined that current interlock strategies are sufficient.

Failures involving the magnet protection and the crab cavities constitute the most severe hazards. The former consists of quench heaters and a new system known as coupling loss induced quench (CLIQ). A new connection scheme is proposed for these, in order to limit their effect on the beam. Dedicated interlocks for detecting spurious discharges of these systems are also found to be necessary. The perturbation of the beam orbit caused by the extraction of only one beam is another source of uncontrolled beam losses. A fast hardware linking of the two beams to limit the delay between extracting the two beams of maximum one LHC turn (89 μs) is found to be necessary.

Beam-dust interactions have detrimental effects on the machine performance and availability. Advances are made on the understanding of their dynamics through dedicated experiments combined with theoretical work and simulations.

Superconducting magnet quenches are shown capable of causing fast orbit perturbations. The effects of beam-beam compensating wires as well as coherent excitations by the transverse beam damper are also discussed. Finally, realistic combinations of multiple failures is also discussed.

Keywords: machine protection, failures, beam losses, accelerator physics

Björn Lindström, Department of Physics and Astronomy, FREIA, Box 516, Uppsala University, SE-751 20 Uppsala, Sweden.

ISSN 1651-6214
ISBN 978-91-513-1081-7
urn:nbn:se:uu:diva-426416 (http://urn.kb.se/resolve?urn=urn:nbn:se:uu:diva-426416)

ISBN 978-1-4842-6870-4
https://doi.org/10.1007/978-1-4842-6871-1

List of papers

This thesis is based on the following papers, which are referred to in the text by their Roman numerals.

I **Fast failures in the LHC and the future high luminosity LHC**
B. Lindstrom, P. Bélanger, L. Bortot, R. Denz, M. Mentink, E. Ravaioli, F. Rodriguez Mateos, R. Schmidt, J. Uythoven, M. Valette, A. Verweij, C. Wiesner, D. Wollmann, M. Zerlauth
Phys. Rev. Accel. Beams **23**, 081001, (2020)

II **Dynamics of the interaction of dust particles with the LHC beam**
B. Lindstrom, P. Bélanger, A. Gorzawski, J. Kral, A. Lechner, M. Vaananen, D. Valuch, B. Salvachua, R. Schmidt, C. Wiesner, D. Wollmann, C. Zamantzas
submitted to *Phys. Rev. Accel. Beams*

III **Results of UFO dynamics studies with beam in the LHC**
B. Lindstrom, A. Apollonio, P. Bélanger, M. Dziadosz, A. Gorzawski, L. Grob, E.B. Holzer, A. Lechner, R. Schmidt, M. Valette, D. Valuch, D. Wollmann
Journal of Physics: Conf. Series, **1067**, 022001, (2018)

IV **Machine protection experience from beam tests with crab cavity prototypes in the CERN SPS**
B. Lindstrom, H. Bartosik, T. Bohl, A. Butterworth, R. Calaga, L.R. Carver, V. Kain, T.E. Levens, G. Papotti, R. Secondo, J. Uythoven, M. Valette, G. Vandoni, J. Wenninger, D. Wollmann, M. Zerlauth
Journal of Physics: Conf. Series, **1350**, 012004, (2019)

V **Crab cavity failures combined with a loss of the beam-beam kick in the high luminosity LHC**
B. Lindstrom, H. Burkhardt, V.K.B. Olsen, A. Santamaría García, K.N. Sjobak, M. Valette, D. Wollmann
in *Proc. 9th Int. Particle Accelerator Conf. (IPAC'18)*, Vancouver, B.C., Canada, (2018)

The author's contribution to the papers

Paper I I did all the failure studies, with help from MV, including building most of the simulation models and analyzing the results. MV had the idea of changing QH connection schemes. ER and LB did the magnet simulations for CLIQ and the triplet quench. I was the main driver for the experiments, which were done in collaboration with the co-authors. I did the analysis of the results from the experiments, and interpreted them in close collaboration with MV and DW. I wrote the full paper, with input from the co-authors and DW in particular.

Paper II I devised the method of studying the UFO dynamics with blown-up bunches, executed the experiment and did the analysis of the results, with help from MVaa and RS. Together with PB and MVaa I upgraded the simulation code and did the initial Monte-Carlo simulations. I wrote about half the paper, with the other half written by PB who did the Monte-Carlo simulations presented in the paper, as well as the ICBLM studies.

Paper III The initial proof-of-concept experiment using wire scanners was planned by MV and conducted and analyzed by PB. I designed and executed the UFO experiment with beam and did the analysis of the results using the bunch-by-bunch method explained in more detail in Paper II, which I devised. I wrote the paper and orally presented the results at IPAC.

Paper IV I drove the machine protection part of the experiments, did the initial theoretical studies using simulation models that I wrote, and I did the analysis of the results, in collaboration with MV and DW. I wrote the paper.

Paper V I did the theoretical studies using simulation models that I developed. I analyzed and interpreted the results in close collaboration with MV and DW. I wrote the paper.

Contents

1. Particle Accelerators

Particle accelerators are devices designed to accelerate subatomic charged particles such as protons or electrons, as well as heavier ions. The accelerated particles can then be used for a number of different applications, such as producing new isotopes, as light sources, studying matter on small scales, studying the fundamentals of physics, and even as the main component of old television screens. One important industrial application of accelerators is for ion implantation in semiconductor production. The technological advances made through accelerator development also find various usage in both science and in society in general, such as superconducting magnet technology.

1.1 History of Particle Accelerators

In 1909, Geiger and Marsden performed their famous experiment, where they used a radioactive source to bombard a thin gold foil with alpha particles [1]. From the scattering angles, Rutherford was able to determine that gold atoms consist of a small and heavy core with a positive charge, with electrons around it forming most of the volume of the atom [2]. This partially confirmed the planetary model of the atom previously proposed by Nagaoka [3]. In order to explain how such a system could be stable, quantum mechanics was developed. From this, the wave-particle duality was conceptualized, that is, any object has both particle and wave properties. How small of an object that can be probed, e.g. by the alpha particles in the scattering experiment, depends on the wavelength, λ, of the probe, which can be determined through De Broglie's equation:

$$\lambda = \frac{h}{p}$$

where h is the Plank constant and p the momentum of the particle. From this, it is apparent that in order to probe smaller objects, large momenta, meaning large kinetic energies, are required. In nature, there are particles from radioactive sources as well as cosmic rays. The particles from radioactive sources lack sufficient energy to probe the core of an atom or its constituents, and while cosmic rays can be of sufficient energy, they are unpredictable and have a low flux. This is where particle accelerators come into the picture.

Electrostatic accelerators were the first types of particle accelerators. They use a static voltage to accelerate charged particles across the voltage gap that

they produce. They are the basis for e.g. the cathode ray tube, used for decades to produce television monitors, by accelerating a beam of electrons across the voltage gap and then directing it towards a phosphorescent screen producing images. One type is based on van de Graaff generators, often used today to create x-rays, whereas the Cockroft-Walton generator is still used to power large particle accelerators. Electrostatic accelerators are also used as the beam source in modern accelerators.

The main problem with this kind of accelerators is that they can only accelerate particles once, or twice if charge is changed by stripping electrons from negative ions like the Uppsala University Tandem accelerator. Electric breakdown also puts a limit on the voltage that can be applied. The maximum kinetic energy achievable is thus on the order of 10 MeV[1], which is about an order of magnitude larger than particles produced through radioactive decays.

Inspired by a paper from 1924 written by Ising [4], Widerøe conceived the first accelerator where an alternating voltage was used in 1927. In the accelerator community, this is usually denoted RF, since the frequency of the alternating voltage lies in the radio frequency range. His accelerator consisted of a series of hollow cylinders placed in a line, separated by gaps [5]. This is shown in Fig. 1.1. Applying an alternating voltage to these cylinders, with every other cylinder having the same polarity, one can use a low voltage to accelerate a particle multiple times. If the RF is adjusted to the structure such that it synchronizes correctly with the particles, a particle sees an accelerating electric field when it is inside of a gap. As the particle enters the following cylinder, it is screened from the electric field. In the meantime the polarity of the field is reversed, such that when the particle once again enters the next gap, it sees another accelerating field. Particles can thus be accelerated N times to an energy of N times the effective voltage seen by the particles. Note that the length of the hollow cylinders increases, since the speed of the particle increases. For ultra-relativistic accelerators, they remain the same size. These early accelerators were of a type known as a *linear accelerator*, or *linac* for short.

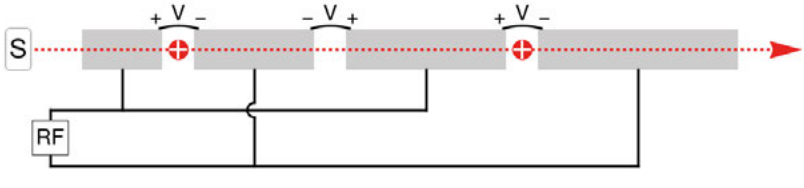

Figure 1.1. Schematic of a Widerøe drift-tube linear accelerator. The particle source is designated by S, and positively charged particles by the encircled +. The drift-tubes are shaded and the voltage between them in the gaps is noted by the V. RF is the power source, providing the alternating voltage.

[1] 1 eV, electron volt, is defined as the energy that a particle of unit charge acquires when traversing a gap of 1 V

Based on this work, Lawrence realized in 1929 how to put this into a more compact version, by only using two half-circular electrodes and an electromagnet to bend the particles into circular orbits [6]. The particles are then accelerated in the gap between the half-circles, and as their kinetic energy increases, the radius of their circular motion increases, perfectly offsetting the increased speed such that the synchronization with the RF is kept. Thus, the *cyclotron* was born. Since its advent, the cyclotron has been used for a variety of things, such as nuclear physics research, radioisotope production, discovery of new elements, isotope separation, cancer treatment and material analysis [7–11].

Due to their compactness and relative simplicity, cyclotrons were the most powerful accelerators until the 1950s. One challenge with the cyclotron is that, as particles become relativistic, their mass increases, and thus also their rigidity in the magnetic field that is bending their paths. This leads to an increase of their paths in a way that they lose synchronicity with the accelerating voltage. These problems can be worked around by e.g. only accelerating short pulses of beam and adjusting the RF frequency during the acceleration. However, another issue with cyclotrons is that there is a limit to how large and strong the magnet can be.

Synchrotrons, first invented by Veksler [12], superseded the cyclotrons as the highest energy accelerators in the 1950s. Synchrotrons are also circular machines, but consist of multiple separate magnets, each with specific functions. One set of magnets with a constant vertically aligned field, *dipole* magnets, are used to bend the beam path. Another set of magnets, *quadrupoles*, with a linear gradient symmetric around the center, are used to keep the beam from diverging. Acceleration can be done by *RF cavities*, that the particles pass once per turn. These RF cavities correspond to the gaps in the Widerøe accelerating structure. During the acceleration process, the current in the dipole magnets is ramped up. This automatically leads to an acceleration in the RF cavities such that the particles remain on the same orbit despite the stronger magnetic fields. The frequency of the RF cavities is also adjusted during the acceleration process to retain synchronization. While the continuous beams available in some types of cyclotrons are not possible in synchrotrons, where beams are instead injected, accelerated and extracted in cycles, synchrotrons can be built arbitrarily large to attain significantly higher beam energies.

Synchrotrons are mainly used in research, such as fundamental physics research where they have been used to discover the majority of both elementary and composite particles, and also as so called synchrotron light sources, where they produce intense light from infrared to gamma, used for research in many branches of the natural sciences.

1.2 Standard Model

The largest accelerator, with the highest beam energy, is the Large Hadron Collider (LHC) at CERN [13]. It is an almost 27 km long synchrotron, with beam energies reaching up to 6.5 TeV for protons (design value is 7 TeV). One of the main goals with the LHC was to discover new particles, in particular the final missing piece of the so called standard model of particle physics. The standard model is a theory describing, with the exception of gravity, the fundamental forces of nature; the electromagnetic, the weak and the strong interactions. It also classifies all known elementary particles and it describes how they interact with each other to form composite particles. A schematic of the elementary particles is shown in Fig. 1.2.

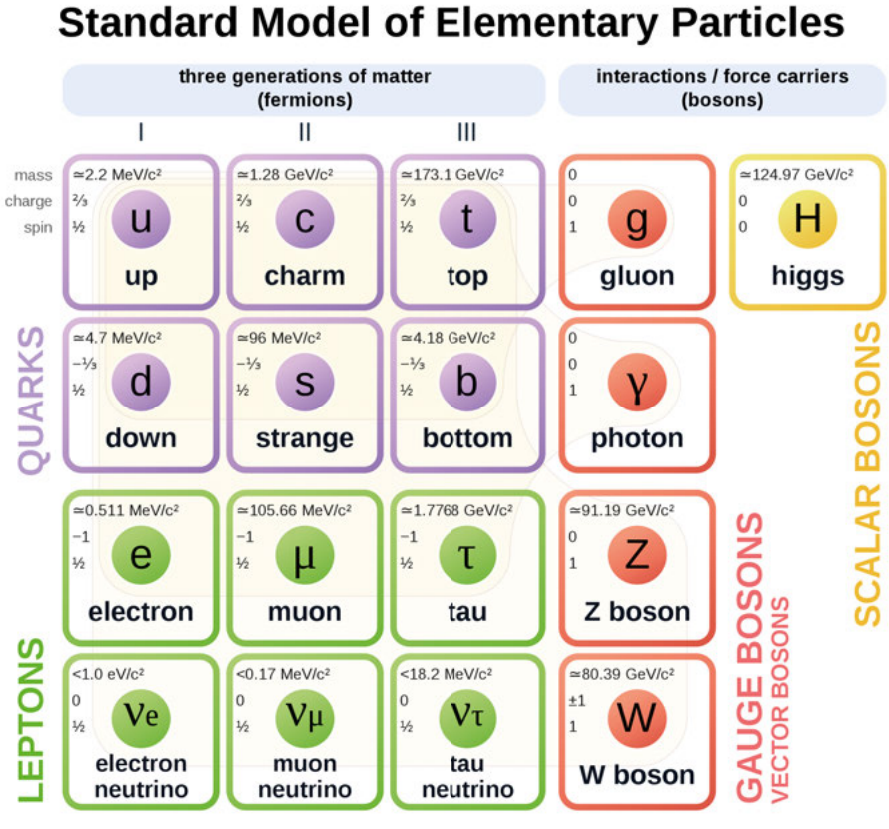

Figure 1.2. The standard model of elementary particles [14]. See the text for explanation.

There are the fermions (quarks, leptons, and their anti-particles) that make up matter, as well as bosons that act as force carriers, mediating interactions

between the fermions. For the fermions, there are three generations, where e.g. the heavier counterparts of the electron are the muon and the tau.

The force carriers consist of vector bosons with a spin of 1 (eight types of gluons, photon, W and Z boson). In addition, the scalar (spin 0) Higgs boson is the quantum excitation of the Higgs field and is responsible for the generation of mass for quarks, charged leptons and the W and Z bosons. Gluons are the force carriers of the strong force, which binds quarks together into hadrons (e.g. protons and neutrons). The strong force is also the source of most of the mass in ordinary matter through nuclear binding energy.

Photons are the quantum excitation of the electromagnetic field, and consequently constitute the force carrier of the electromagnetic force. The W and Z bosons are the force carriers of the weak force, with W bosons being charged and thus capable of mediating charge transfer interactions, e.g. beta decays where the flavor of one down quark is changed to an up quark. The Z bosons are instead neutral and consequently leave the interacting particles unaffected, except for a transfer of spin and momentum. W and Z bosons have a high mass, which limits the range of the weak interaction, while photons instead have zero mass giving the electromagnetic force an infinite range.

When formulated, the standard model predicted three particles yet to be found, the top quark, the tau neutrino and the Higgs boson. The former two were discovered in 1995 [15, 16] and 2000 [17], respectively, before the LHC started construction in 2003. The LHC then successfully confirmed the existence of the Higgs boson in 2012 after a few years of operation, completing the search for particles in the standard model [18, 19].

1.3 Motivation for HL-LHC

With the standard model completed, the question is what comes after. There are still several phenomena in nature that the standard model cannot explain, in particular it does not incorporate gravity. Other examples are:

1. The matter-antimatter asymmetry: In the observable universe, there is a significant predominance of matter over antimatter, despite most processes being symmetric in their respective productions. Some sources of charge parity violations, which could explain this asymmetry, are present in the standard model, but they are not enough to explain the magnitude of the observed asymmetry in the universe.
2. Non-zero neutrino masses: Neutrinos are observed to oscillate between their different lepton flavors, namely the electron, muon and tau neutrinos. This implies that neutrinos have a non-zero mass, however the standard model predicts neutrinos to be massless.
3. Dark matter and dark energy: From observations of the universe, e.g. on gravitational effects and the accelerating expansion of the universe, it appears to contain more matter and energy than is otherwise observ-

able. In fact, the observable mass and energy only contributes a small fraction of the total that should exist. There are however no explanations within the standard model for what this dark matter and energy could be composed of.

One goal of the LHC is to find hints of new physics, beyond the standard model, to guide the theoretical work. The problem is that the sought-after reactions are rare, hidden in a huge background of more common, and already understood, reactions. To maximize the potential of the LHC, it will thus be upgraded to the so called High Luminosity LHC (HL-LHC) [20]. This will allow more precise measurements of known properties, such as properties of the Higgs boson, which can expose anomalies giving hints of new physics. It is also possible that new particles that are necessary for explaining some of the unanswered questions could be found with more data being accumulated.

Luminosity is a figure of merit of a collider, and is proportional to the collision rate for e.g. the protons in two colliding proton beams. Multiplying this by the *cross section*, that is, the probability that a reaction occurs, gives the rate of produced events that one is searching for. In order to see rare events, one needs to accumulate a lot of statistics, which depends on the production rate and thus on the luminosity. In HL-LHC the goal is therefore to maximize the luminosity of the LHC.

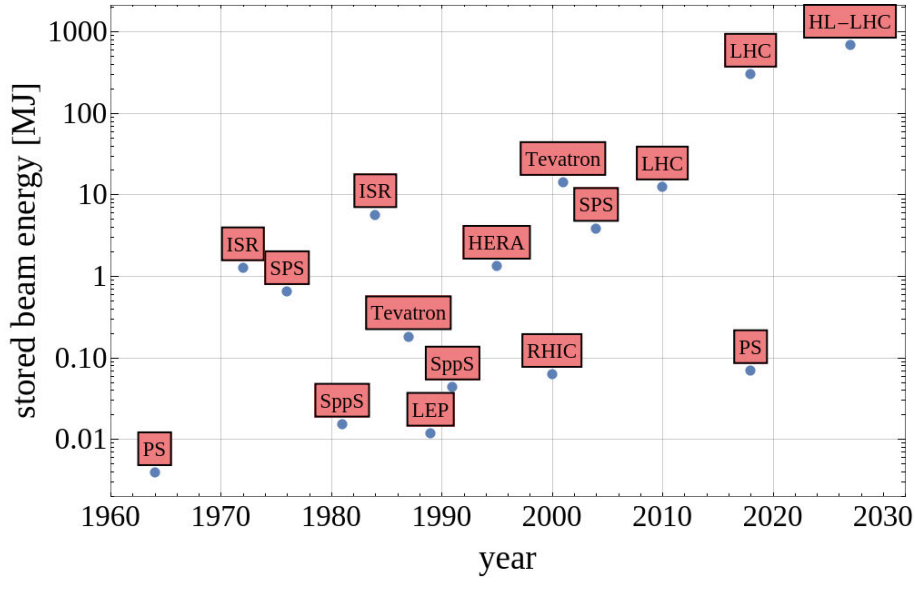

Figure 1.3. Total stored beam energy for some major synchrotrons, plotted against the year that the energy was attained. Some machines are present twice, with the first point being shortly after commissioning when the energy is usually lower than what is possible to achieve.

This comes with a number of technical challenges, as well as an increased stored beam energy. In Fig. 1.3, some major synchrotrons are shown, with their stored beam energy plotted vs the year that that particular energy was attained. Aside from a few exceptions, such as LEP, being a lepton collider, RHIC being a heavy ion collider, and SppS being a proton-antiproton collider, there is a clear trend towards higher stored beam energies. In particular, the LHC with its almost 362 MJ of design energy, per beam, is capable of drilling a 35 m hole through solid copper [21, 22]. This will be further aggravated by the 678 MJ of beam energy in the HL-LHC.

Machine Protection constitutes the field where it is ensured that the energy stored in the circuits, magnets and the beam can always be extracted safely. This is a field where the LHC has been a strong driver, not only because of its unprecedented stored beam energy, and thus destructive power, but also because of the long downtimes and high costs associated with a loss of only a fraction of the full beam. Potential damage mechanisms to the accelerator, e.g. due to beam losses, and how to avoid them is studied. Through this, a highly reliable protection system has been designed, developed and implemented into the LHC.

The topic of this thesis is to study the beam-related machine protection challenges present in the LHC, with a focus on its upgrade to the HL-LHC.

1.4 Structure of the thesis

The thesis starts with an introduction to accelerator physics in the second chapter, briefly explaining all the concepts that are necessary for understanding the work behind the thesis. The third chapter follows with a detailed explanation of the LHC, including its structure, its different components, the detectors used for this work, as well as some of the main machine protection related equipment. The changes introduced by the HL-LHC upgrade are also summarized.

The fourth chapter discusses failures in general terms, what they are, how they can be classified, what can happen with the beam as well as how to scale consequences between different conditions.

The fifth chapter summarizes the specific failure studies that were done and are detailed in the papers that the thesis is built upon. They are discussed in relation to each other and what they mean for the project. Concluding remarks are then made in the sixth and final chapter.

2. Accelerator Physics

The goal of this chapter is to introduce the reader to the basic concepts in accelerator physics necessary to appreciate and understand the studies that laid the framework for this thesis. For a comprehensive introduction to accelerator physics, the reader is referred to text books, such as Ziemann [23], Conte and MacKay [24], and Peggs and Satogata [25], from where inspiration for this work was drawn.

2.1 Coordinate System

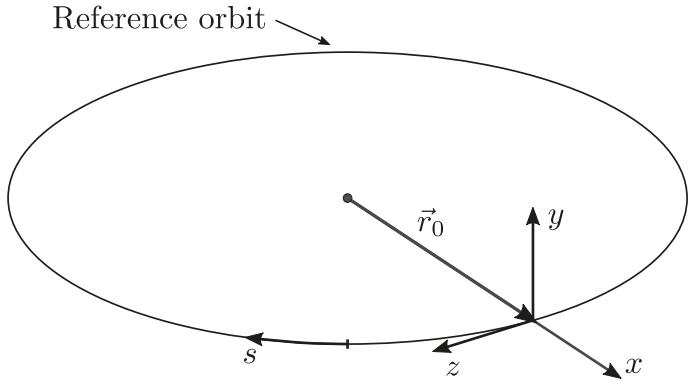

Figure 2.1. Comoving orthogonal coordinate system.

Since the beam particles in an accelerator closely follow a reference trajectory, a comoving orthogonal coordinate system is useful. This is referenced to an ideal particle perfectly following the reference trajectory, and is depicted in Fig. 2.1. $\hat{z}$ is tangential to the beam orbit, $\hat{x}$ points horizontally out from the orbit, and $\hat{y}$ points vertically up from the orbit. The following variables are used for the six-dimensional phase space:

- x: horizontal offset
- $x' = {}^{p_x}/_{p_0}$: horizontal angle
- y: vertical offset
- $y' = {}^{p_y}/_{p_0}$: vertical angle
- z: difference in tangential position
- $\delta t = \frac{\Delta E}{p_0 c}$: energy error

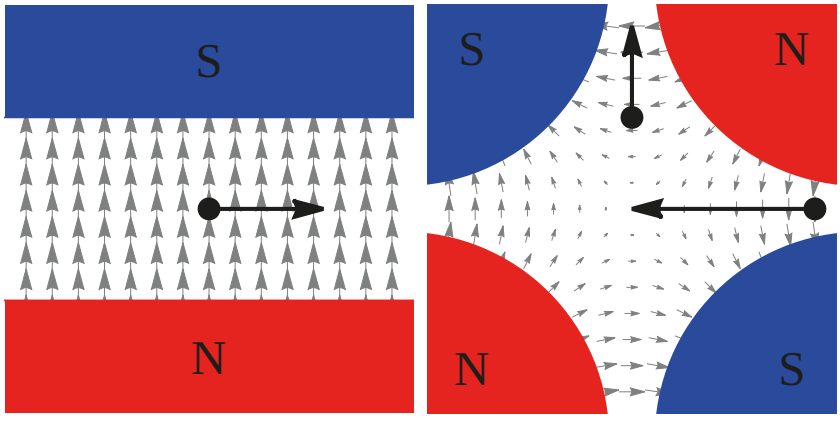

Figure 2.2. Magnetic fields for a dipole (a) and a quadrupole (b)

The horizontal and vertical angles are defined through their respective transverse momenta divided by the reference momentum. s is an independent variable signifying the position along the circumference of the reference orbit, and is different from z in that z is comoving with the reference particle whereas s is referenced to a static position in the accelerator.

The reference particle lies on $(x, x', y, y', z, \delta t) = (0,0,0,0,0,0)$. The actual orbit, known as the *closed orbit* of the beam can however differ from the reference orbit in the transverse coordinates. This is an orbit that upholds periodic boundary conditions and repeats from turn-to-turn.

2.2 Linear Transverse Dynamics

One of the main equations governing the dynamics of particle accelerators is the Lorentz force

$$\bar{F} = q(\bar{E} + \bar{v} \times \bar{B}) \tag{2.1}$$

Electric fields serve two purposes, to provide acceleration in the RF cavities, where they are parallel to the beam direction, and to provide transverse kicks to the beam. The magnetic fields are in general used to keep the beam focused and stable on the correct orbit, but also for providing stronger transverse kicks. Aside from field-free drift spaces, the bulk of an accelerator consists of dipolar and quadrupolar magnets. Their respective magnetic fields are shown in Fig. 2.2. The resulting force on a positively charged particle traveling into the paper is also shown. Note that these are the *normal field* alignments. There are also *skew field* alignments, where the magnet is transversely rotated by π over the number of poles (2 for dipole, 4 for quadrupole, 6 for sextupole...).

The dipolar field is ideally constant across the full beam region and has a perfect cut-off at the ends of the magnets. Most are vertically aligned in order to bend the particles horizontally, along the circumference of the accelerator. Setting a constant vertical magnetic field in the Lorentz force equation and equating it with the centrifugal force gives:

$$qvB_y = \frac{\gamma_r m_0 v^2}{\rho} \tag{2.2}$$

where v is the speed of a particle with charge q, γ_r the Lorentz factor, m_0 the mass of the particle and ρ the radius of curvature. Rewriting this equation with the norm of a general magnetic flux density gives:

$$B\rho = \frac{p}{q} \tag{2.3}$$

where $B\rho$ is the *beam rigidity* and p is the momentum of the particle. This is a convenient formula highlighting the relation between the momentum of a particle and its radius of curvature given a certain magnetic field. For example in the LHC, the nominal dipole field is 8.33 T and the nominal particle momentum 7 TeV/c. This gives a radius of curvature of:

$$\rho = \frac{7 \cdot 10^{12}}{8.33 \cdot 299792458} \frac{Vs}{Tm} = 2803\,\mathrm{m} \tag{2.4}$$

If the LHC only consisted of dipole magnets, it would thus have a circumference of 17612 m. Since each main dipole magnet is 14.3 m long, this means that 1232 dipole magnets are required. This is in fact the actual number in the LHC as built.

The quadrupolar magnetic field (Fig. 2.2) has a linear gradient, zero in the center. Particles that are off-center in the magnet will thus see a kick either towards the center, or out from the center. These are used for focusing the beam and keeping it from diverging. The focusing strength k, or the reciprocal of the focal length f, is given by:

$$k = \frac{1}{f} = \frac{q}{p}\frac{\partial B_y}{\partial x} = \frac{q}{p}\frac{\partial B_x}{\partial y} \tag{2.5}$$

In linear beam optics, transfer matrices are convenient for calculating how particles are transported through an element. Since matrices can be multiplied together, the full accelerator can be expressed using one matrix. The effect of a drift space on the transverse dynamics of a single particle is given by:

$$\begin{pmatrix} x_2 \\ x_2' \\ y_2 \\ y_2' \end{pmatrix} = \begin{pmatrix} 1 & L & 0 & 0 \\ 0 & 1 & 0 & 0 \\ 0 & 0 & 1 & L \\ 0 & 0 & 0 & 1 \end{pmatrix} \begin{pmatrix} x_1 \\ x_1' \\ y_1 \\ y_1' \end{pmatrix} \tag{2.6}$$

where L is the length of the drift space. For dipole magnets, there are different types depending on how their faces are aligned to the reference orbit. A so called *sector dipole* follows the curvature of the reference orbit, such that the beam is incident with a right angle. This is the case for all LHC main dipoles. Their transfer matrix, in the horizontal plane, is given by:

$$\begin{pmatrix} x_2 \\ x_2' \end{pmatrix} = \begin{pmatrix} \cos[\theta] & \rho \sin[\theta] \\ -\frac{1}{\rho}\sin[\theta] & \cos[\theta] \end{pmatrix} \begin{pmatrix} x_1 \\ x_1' \end{pmatrix} \tag{2.7}$$

where the bending radius $\theta = L/\rho$. A focusing of $1/f \approx \theta/\rho$ appears due to the different path lengths within the magnet for particles with different horizontal offsets. In the vertical plane, the effect is zero in the ideal case. However, in reality, there is a small focusing from the fringe fields extending outside of the magnet.

For a quadrupolar magnet:

$$\begin{pmatrix} x_2 \\ x_2' \end{pmatrix} = \begin{pmatrix} \cos[L\sqrt{k_1}] & \frac{1}{\sqrt{k_1}}\sin[L\sqrt{k_1}] \\ -\sqrt{k_1}\sin[L\sqrt{k_1}] & \cos[L\sqrt{k_1}] \end{pmatrix} \begin{pmatrix} x_1 \\ x_1' \end{pmatrix} \approx \begin{pmatrix} 1 & L \\ -k_1 L & 1 \end{pmatrix} \begin{pmatrix} x_1 \\ x_1' \end{pmatrix} \tag{2.8}$$

$$\begin{pmatrix} y_2 \\ y_2' \end{pmatrix} = \begin{pmatrix} \cosh[L\sqrt{|k_1|}] & \frac{1}{\sqrt{|k_1|}}\sinh[L\sqrt{|k_1|}] \\ \sqrt{|k_1|}\sinh[L\sqrt{|k_1|}] & \cosh[L\sqrt{|k_1|}] \end{pmatrix} \begin{pmatrix} y_1 \\ y_1' \end{pmatrix} \approx \begin{pmatrix} 1 & L \\ k_1 L & 1 \end{pmatrix} \begin{pmatrix} y_1 \\ y_1' \end{pmatrix} \tag{2.9}$$

where k_1 is the focusing strength, and L the length of the quadrupole. The left transfer matrix corresponds to a thick quadrupole and the right to a thin quadrupole where the focal length $f = 1/k_1 L$ is much larger than the length of the magnet. In the LHC, the thin lens approximation is usually sufficient.

As can be seen in the transfer matrix for the thin quadrupole, a particle with e.g. a positive offset in x will receive a negative change of its angle, i.e. a negative kick. Likewise, if the particle has a negative offset in x, it will see a positive kick. The particle thus gets kicked back towards the reference orbit, and is *focused* (c.f. Fig. 2.2). Instead considering a particle with a vertical offset, it will get a positive kick for positive offsets and vice versa, meaning that it is *defocused*. This highlights the fact that it is not possible to simultaneously focus a beam both vertically and horizontally using the same quadrupole magnet.

By convention a quadrupole is considered a *focusing quadrupole*, when it focuses horizontally and defocuses vertically. In order to keep the beam from diverging, one thus needs to alternate between focusing and defocusing quadrupoles, as depicted in Fig. 2.3. The figure shows the effect on the beam size (or individual particles with a given offset) in the horizontal plane (blue) and the vertical plane (red). A combination such as this, composed of alternating focusing and defocusing quadrupoles, with either dipole magnets or drift

spaces in between, is known as a *FODO lattice*. The FODO lattice is the basic building block of many accelerators, but other magnet configurations are also possible.

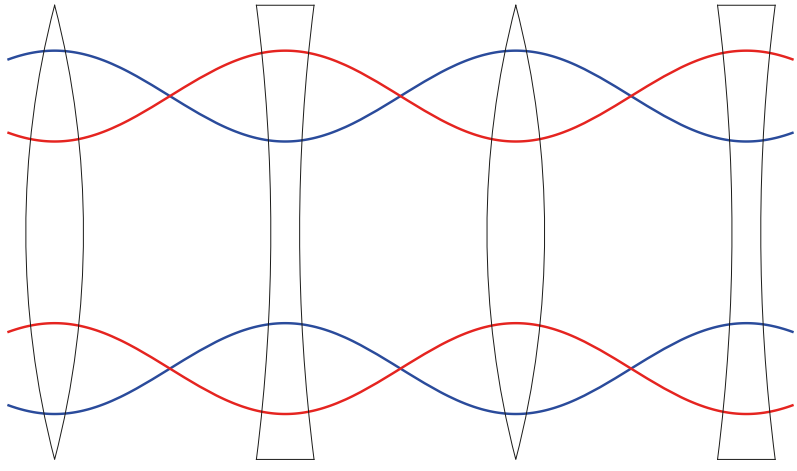

Figure 2.3. Alternating focusing and defocusing quadrupoles forming two FODO lattices. The horizontal beam size (blue) is focused in focusing quadrupoles, whereas the vertical beam size (red) is focused in defocusing quadrupoles.

This works similarly to a linear harmonic oscillator. Figure 2.4(a) shows the displacement and the speed of a particle attached to an oscillator over a few periods. This corresponds to the transverse displacement and angle respectively for a particle in a circular accelerator. The points of maximum displacements correspond to focusing quadrupoles whereas the minimum displacements correspond to defocusing quadrupoles. In between these extrema, where the speed is at a maximum, the particle in an accelerator would have a maximum angle and be between two consecutive quadrupoles.

Figure 2.4(b) shows what this looks like in phase space. The particles remain on the same circle, with x and x' continuously changing into each other.

2.3 Transverse beam distribution

Looking at a cross section of the beam, it consists of many particles. The ideal particle follows the design optics, but in reality particles have certain errors in the six phase space coordinates. In many accelerators, including the LHC, the distribution of particles around their coordinates are approximately normally distributed (Gaussian). For e.g. the horizontal plane, the distribution takes the following form:

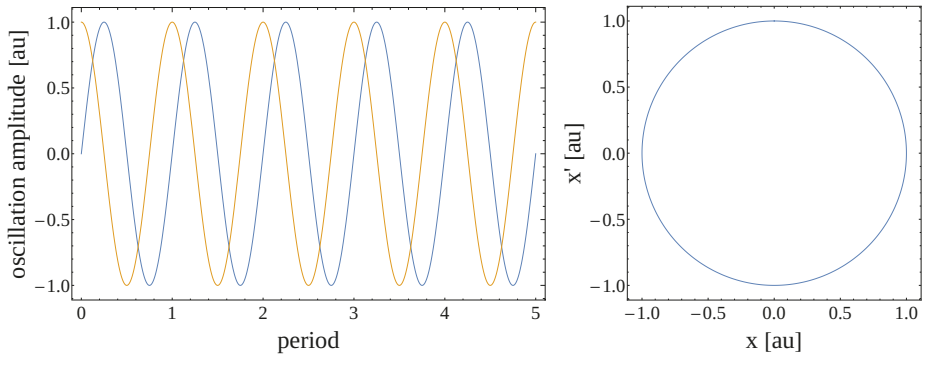

(a) **(b)**

Figure 2.4. Position x and speed x' in a linear harmonic oscillator plotted for a few periods (a) x and x' vs phase (b) phase plot of x and x'

$$\rho(x,x') = \frac{1}{\sigma_x \sigma_{x'} \sqrt{2\pi}} \exp\left[-\frac{1}{2}\left(\frac{x^2}{\sigma_x^2} + \frac{x'^2}{\sigma_{x'}^2}\right)\right] \tag{2.10}$$

where the σ are the first moments, the standard deviation of the spread in x and x'. This is a projection of the full 6D phase space onto the horizontal plane, and looks similar in the vertical plane. Figure 2.5 shows a schematic of this distribution, at three different locations in a FODO lattice (c.f. Fig 2.3). The depicted ellipse in each plot corresponds to one standard deviation. The area of this ellipse is $\pi\varepsilon$, where ε is called the *emittance*. It has dimensions *length* multiplied by *angle*, and usually has the unit $\mu\text{m} \cdot \text{rad}$.

As each particle moves through the accelerator, it stays on a certain ellipse that it started on. Tracing all of them through the accelerator, one thus gets a change of the shape as shown by the three locations. In the left plot, the horizontal offset is at a maximum while the angle is minimized, corresponding to the center of a focusing quadrupole. In the center plot, the ellipse is tilted meaning that the location is in-between two quadrupoles, and finally in the last plot, the horizontal angle is at a maximum while the offset is at a minimum, implying a defocusing quadrupole.

One can see that the depicted ellipse containing a set fraction of the particles, follows the change in shape, but its total area remains constant. This is otherwise known as Liouville's theorem: *The local point density of an ensemble of N particles in the 6d phase space is conserved.* As long as there is no coupling between the transverse planes and the longitudinal plane, this theorem also holds true when considering each plane separately. This implies that a particle beam has an intrinsic size in phase space that cannot be reduced by the focusing lattice.

Liouville's theorem is however breached for non-conservative forces. This includes scattering between particles within the beam that increases the emit-

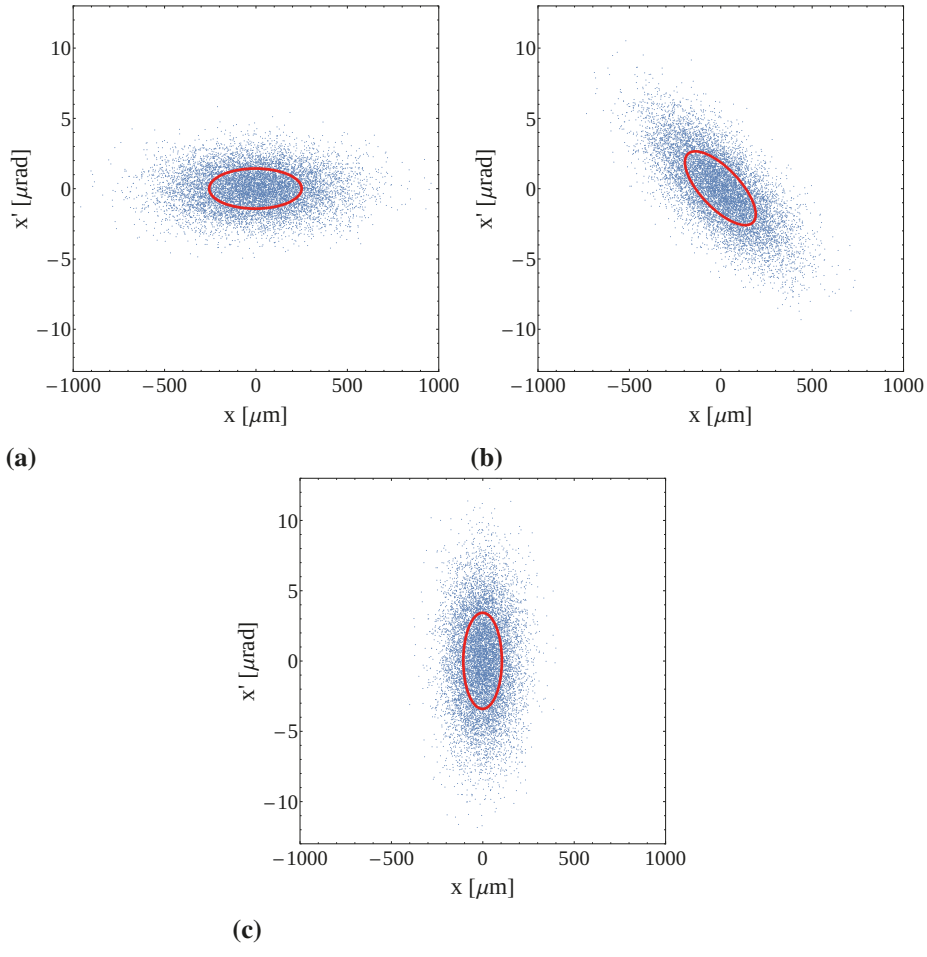

Figure 2.5. Beam cross section, horizontal phase space, at three different locations in a FODO lattice (c.f. Fig 2.3). The red ellipse shows a 68 % confidence region. (a) focusing quadrupole (b) between focusing and defocusing quadrupole (c) defocusing quadrupole

tance, as well as methods of *beam cooling*, where the emittance is decreased. Synchrotron radiation is an intrinsic source of beam cooling for in particular electron machines.

2.4 Twiss Parameters

The equation governing the motion described is known as Hill's equation. It is a differential equation for motions with periodic focusing properties ($k(s)$):

$$x''(s) + k(s)x(s) = 0 \tag{2.11}$$

with the general solution

$$x(s) = \sqrt{\varepsilon}\sqrt{\beta(s)}\cos[\varphi(s) + \varphi_0] \tag{2.12}$$

The emittance ε appears as a constant, signifying its function as an intrinsic beam parameter. $\varphi(s)$ is known as the phase advance, and $\beta(s)$ is the *betatron function*, or beta function for short. These parameters are determined by the focusing lattice; the beta function is large in focusing quadrupoles, whereas in defocusing quadrupoles it is small. The number of betatron oscillations throughout the length L of the full machine, meaning the integrated phase advance, gives the *betatron tune*, or simply the tune:

$$Q = \frac{\varphi(L)}{2\pi} = \frac{1}{2\pi}\int \frac{ds}{\beta(s)} \tag{2.13}$$

The fractional part of the tune, known as the *working point*, determines how the horizontal and vertical phase space coordinates look like from turn to turn. If the fractional part is zero, a particle with a given set of coordinates x_0, x_0', y_0, y_0' not equal to zero, would have the exact same coordinates if observed on the following turn at the same location in the machine. Due to the non-zero fractional tune, there is however an oscillation between the displacements and the angles. Consequently an ellipse is traced out in phase space when the particle is observed over multiple turns at the same location in the machine. A badly chosen fractional tune can lead to problems with resonances, causing beam losses and emittance growth. This is further explained in Sec. 4.1.

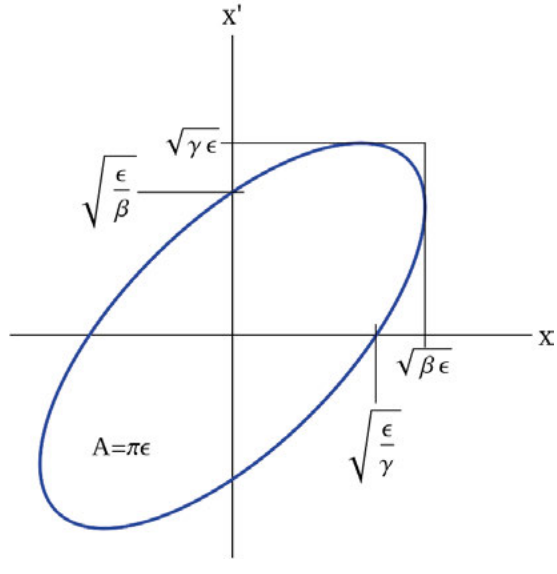

Figure 2.6. Ellipse in transverse phase space with its description by the Twiss parameters.

There are two more parameters,

$$\alpha(s) = -\frac{1}{2}\beta'(s), \quad \gamma(s) = \frac{1+\alpha(s)^2}{\beta(s)} \tag{2.14}$$

These three parameters, β, α and γ are together known as the Twiss parameters, and their relation to the transverse cross section of the beam in phase space is summarized in Fig. 2.6, where e.g. the transverse extent of the beam is given by

$$\sigma = \sqrt{\beta\varepsilon} \tag{2.15}$$

This is the beam size as it depends on the betatron motion of the beam only. As discussed in the following subsection, there is also a dispersive component to the beam size. Together with this, the Twiss parameters can be used to describe the transverse beam properties at any point in the accelerator. Instead of applying transfer matrices to the coordinates of the individual particles, one can transform these parameters directly. This corresponds to mapping a full transverse cross section of the beam from one location to another. Note that these β and γ are not related to the relativistic parameters.

2.5 Off-momentum effects on transverse optics

Similarly to the transverse distribution of particles with small errors around those of the ideal particle, there are also small errors in the longitudinal coordinates, namely z and δt. Recalling Eq. 2.3, and assuming a small deviation in momentum $p = p_0(1+\Delta p/p_0) = p_0(1+\delta)$, the angular kick of a dipole magnet becomes:

$$\theta = \frac{qB}{p} = \frac{qB}{p_0(1+\delta)} \approx \theta_0(1-\delta) \tag{2.16}$$

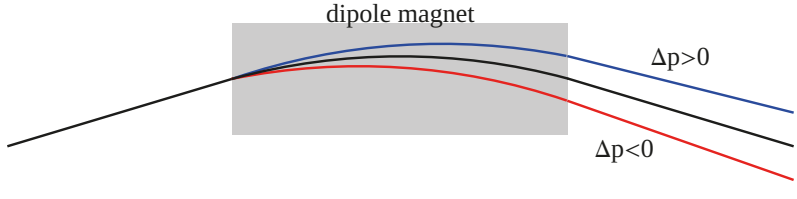

Figure 2.7. Schematic of a dipole magnet with three particles of different momenta, reference particle (black), and a particle with larger (blue) and smaller (red) than reference momentum.

In other words, particles with a larger than nominal momentum ($\delta > 0$) are bent less in the dipole magnet compared to the ideal particle, and particles with

$\delta < 0$ are bent more than the ideal particle ($p = p_0$). A schematic of this is shown in Fig. 2.7. This is known as *dispersion*, and causes off-momentum particles to have slightly different closed orbits throughout the accelerator. Since this causes a transverse spread of the beam particles, the beam size depends not only on the betatron motion, but also on the dispersion. The transverse extent of the beam, known as the *beam size*, is determined by the betatron motion and the dispersion as follows:

$$\sigma(s)_{x,y} = \sqrt{\varepsilon_{x,y}\beta(s)_{x,y} + \left(D(s)_{x,y}\frac{\Delta p}{p_0}\right)^2} \tag{2.17}$$

where $D(s)$ is the *dispersion function*. In the LHC, the RMS relative momentum deviation is approximately 1.1×10^{-4}.

Dispersion is generally more pronounced in the horizontal plane than the vertical plane since it is produced by the dipole magnets. Due to the effect on the beam size, the collision points in a collider are designed to be free of dispersion, which is achieved by special lattices known as *dispersion suppressors*.

The focusing strength of quadrupole magnets is also affected by differences in momentum, an effect known as *chromaticity*. The horizontal focal length is given by:

$$\frac{1}{f} = \frac{q}{p}\frac{\partial B_y}{\partial x} = \frac{q}{p_0(1+\delta)}\frac{\partial B_y}{\partial x} = \frac{1}{f_0(1+\delta)} \approx \frac{1}{f_0}(1-\delta) \tag{2.18}$$

The effect on the off-momentum particles is thus the same as if there was an additional quadrupole magnet with a focal length $-f_0/\delta$. For higher energy particles ($\delta > 0$) the focusing strength consequently becomes weaker in relation to the ideal particle, and stronger for lower energy particles. A schematic of this is shown in Fig. 2.8.

Since the betatron tune depends on the focusing strength of the quadrupole magnets, a change in focusing strength implies that off-momentum particles will have a different tune. Given a distribution of particles, this leads to a chromatic tune spread:

$$\Delta Q = -\frac{\beta_0}{4\pi f_0}\delta \tag{2.19}$$

To avoid resonances, it is important to take the tune spread into account when determining what the fractional part of the tune should be. The chromaticity can be compensated using sextupole magnets as is done in e.g. the LHC and shown in Fig. 2.8. These magnets have a second order gradient.

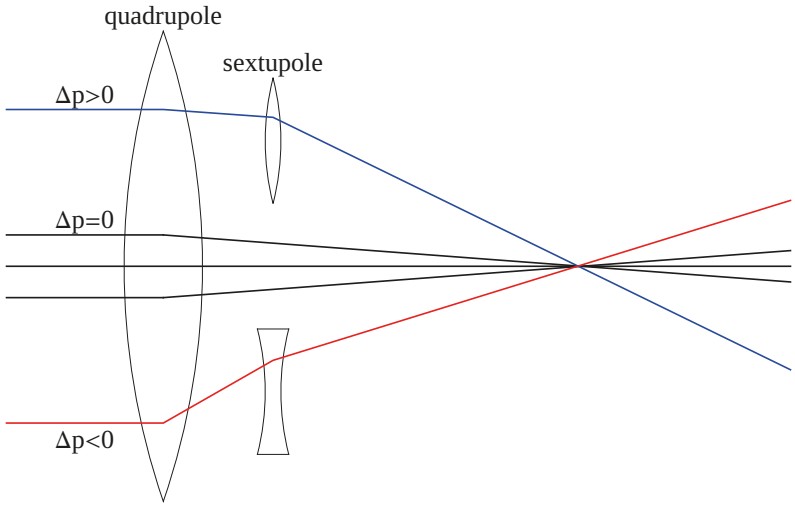

Figure 2.8. Effect of focusing errors in quadrupole magnets for off-momentum particles, as well as their correction using sextupole magnets.

2.6 Normalized coordinates

Consider a beam that is being accelerated, meaning that its longitudinal momentum increases. The vertical angle in phase space, defined through $y' = p_y/p_0$, will then decrease, since the denominator increases. The same holds for the horizontal angle. This means that the transverse beam size decreases during acceleration, and consequently also the emittance. It is thus common to use the *normalized* emittance, defined through

$$\varepsilon_n = \varepsilon_g \beta_r \gamma_r = \varepsilon_g \frac{v}{c}\left(\frac{E}{m_p} + 1\right) \approx \varepsilon_g \frac{E}{m_p} \tag{2.20}$$

where ε_g is the unnormalized, or *geometric* emittance, β_r the fraction of the speed to the speed of light, γ_r the Lorentz factor, E the energy and m_p the particle mass. This normalized emittance remains constant independent of the beam energy.

It is also useful to normalize the horizontal and vertical coordinates into the so called *action-angle* coordinates, through the following:

$$\begin{pmatrix} x_n \\ x_n' \end{pmatrix} = \frac{1}{\sqrt{\varepsilon_g}} \begin{pmatrix} \frac{1}{\sqrt{\beta(s)}} & 0 \\ \frac{\alpha(s)}{\sqrt{\beta(s)}} & \sqrt{\beta(s)} \end{pmatrix} \begin{pmatrix} x \\ x' \end{pmatrix} \tag{2.21}$$

with $\alpha(s)$ and $\beta(s)$ being the local Twiss parameters at location s. The benefit of these normalized coordinates is that particles travel on circles in phase space instead of ellipses. When normalizing the transverse coordinates to the local Twiss parameters, they are expressed in units of the RMS beam

size σ. If for example a particle has an amplitude, or so called *action*, of $1\,\sigma$ at one location in the accelerator, it will thus have an action of $1\,\sigma$ at all other locations in the accelerator. The coordinates can then be unnormalized by taking the inverse matrix and the local Twiss parameters. Many of the results in this thesis are expressed normalized to units of σ, making it easier to understand how critical an effect is, as well as to estimate e.g. resulting beam losses.

2.7 Longitudinal Dynamics

The RF cavities are one of the main components of any accelerator, since they are what accelerates the beam. An example of a simple type, known as a pill-box cavity, is shown in Fig. 2.9. As the RF is applied with a resonating frequency, electromagnetic fields are produced in the cavity. In particular, one is looking to have a longitudinally aligned electric field, as this is what can accelerate the beam particles.

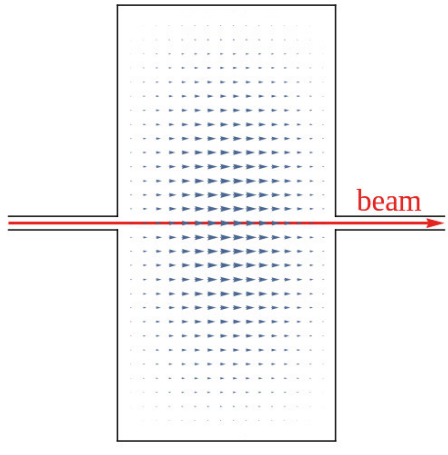

Figure 2.9. Pill-box type RF cavity, showing the electric field and the beam.

Solving the Maxwell equations with appropriate boundary conditions gives:

$$\begin{aligned} E_x &= E_y = 0 \\ E_z(r,\varphi,z,t) &= E_0 J_m(k_c r) e^{\pm im\varphi} e^{\pm ik_z z} e^{i2\pi ft} \end{aligned} \tag{2.22}$$

where E_0 is the peak amplitude, J_m the Bessel function of the first kind, r the transverse radius, z the longitudinal position, f the frequency of the RF and t the time. k_z and k_c are the wave vectors, and m is the mode of the cavity. In simple cases, the mode is 0, and the first zero of the Bessel function is put at the cavity circumference R, meaning that $k_c r = 2.40483 r/R$. We also have the condition that the electric field should vanish at $z = 0$ and $z = l$, meaning that $k_z l = n\pi$, where n is an integer.

Now, the question is what happens with the particles in the beam. For a single particle with a speed βc arriving with a phase φ to the center of the cavity, the energy gain that it receives is given by:

$$\Delta E = q\int_{-l/2}^{l/2} \hat{E}_z \cos[2\pi f t + \varphi] dz = q\hat{E}_z l \cos[\varphi] \frac{\sin[\omega_{rf} l/2\beta c]}{\omega_{rf} l/2\beta c} \tag{2.23}$$

where l is the cavity length, $\hat{E}_z$ the peak electric field in the longitudinal direction, and q the charge of the particle. The energy gain is thus clearly correlated to the phase, meaning the arrival time of the particle in relation to the RF frequency, and it can even be decelerated if the phase is incorrect.

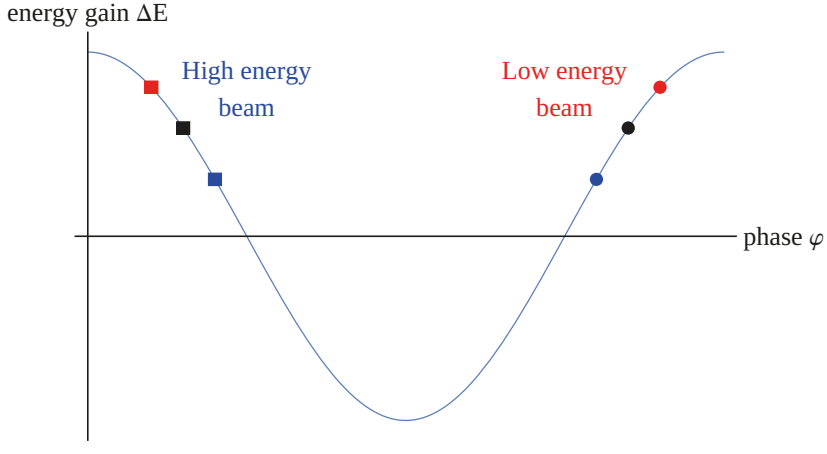

Figure 2.10. Energy ΔE given to a particle as it traverses the RF cavity depending on its phase in relation to the cavity field.

Looking at Fig. 2.10, maximum acceleration is given at the peak of the curve. The reference particle is the black dot. For non-relativistic beams, a particle with a higher energy than the reference particle will have a higher speed, and thus arrive earlier to the cavity, and vice versa. The higher energy particle, blue dot, thus arrives to the left of the reference particle, and sees a smaller energy gain. Similarly, a lower energy particle, red dot, arrives later than the reference particle and thus sees a larger energy gain.

Particles with small deviations in phase from the reference particle are thus focused towards it. This is true as long as the phase of the reference particle is on the rising slope of the sine wave. If it is instead located at the falling part of the sine wave, particles surrounding it would be defocused from it. This effect can be used to produce longitudinally separated groups of particles, with particle free gaps in between them. These groups are known as *bunches*. Several of these bunches can be formed at intervals corresponding to at a minimum the RF period.

For highly relativistic particles the phase of the RF in relation to the bunches needs to be different for focusing to occur, as depicted by the squares in Fig. 2.10. Particles with a higher energy have the same speed ($\approx c$), but their mass increases with the Lorentz factor, giving them a longer path length throughout the accelerator. Higher energy particles thus arrive later than the reference particle and should see a smaller energy gain in the RF cavity. For lower energy particles it is the opposite.

In electron machines, the beams are always above this *transition energy*, meaning that their synchronous phase is placed on the falling edge of the sine wave. In hadron machines, such as the CERN Proton Synchrotron, it is common that particles are injected below the transition energy and then accelerated through it, necessitating a change of the RF phase during acceleration.

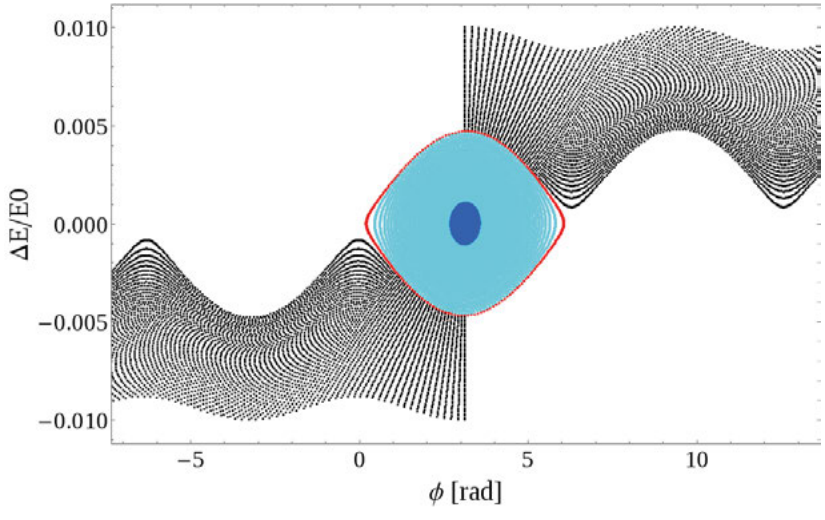

Figure 2.11. RF bucket in the CERN Super Proton Synchrotron, with a cavity voltage of 3 MV. Particles were distributed on a vertical line in the center and then allowed to propagate for many turns. Red shows the bucket border of stability, cyan stable particles within the bucket, blue the extent of the bucket that is filled by beam under nominal conditions. Black are unstable particles that drift away.

While the particles in a bunch are longitudinally focused, once they reach the correct phase of the reference particle, they overshoot, and instead oscillate around the ideal particle. This is shown in Fig. 2.11, where particles were distributed with deviations in their initial energy on the correct phase, and then tracked over many turns. The black particles are unstable and drift away. The cyan and blue particles are stable and perform *synchrotron oscillations* within the border designated by the red particle. The red particle defines the border of this so called *RF bucket*. As with betatron motion and the betatron tune, there is a corresponding *synchrotron tune*, which is the time taken for a particle to circle the RF bucket.

2.8 Collision point

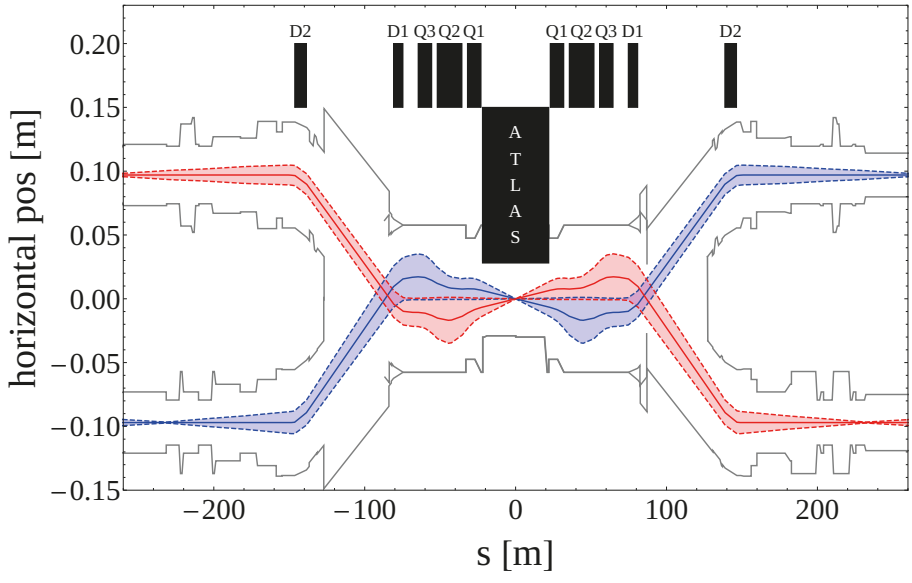

Figure 2.12. The ATLAS horizontal crossing. Blue and red solid lines show the beam orbit for beams 1 and 2, respectively. The dashed lines show their respective beam sizes ($6.7\,\sigma$ envelope) and the gray lines show the physical aperture.

Figure 2.12 shows the orbit around the collision point in ATLAS, for HL-LHC optics (v1.4 [26]), in solid blue line (beam 1) and solid red line (beam 2). The dashed lines show the extent of the beam size (a $6.7\,\sigma$ beam envelope) and the gray lines show the physical aperture. The crossing in ATLAS is horizontal, with an angle of $295\,\mu$rad. The separation (D1) and recombination (D2) dipoles are shown with their correct lengths in s. These magnets combine and separate the beams. The crossing is created by corrector magnets, separating the beam orbits by up to 17 mm in the crossing plane. In CMS, the other high luminosity experiment in the LHC, the crossing is equivalent to ATLAS, but in the vertical plane instead.

Around a collision point, there are generally long drift spaces without any magnets, such that the large detectors can be accommodated. The beta function in a drift space develops with the distance squared. The beta function around the collision point thus depends on the minimum beta function, the β^*, as follows:

$$\beta(s) = \beta^* + \frac{s^2}{\beta^*} \tag{2.24}$$

Furthermore, since charged particle beams require quadrupole magnets to be strongly focused, meaning that each magnet is focusing in one plane and defocusing in the other plane, it is necessary to significantly blow-up the beam size before it can be focused to a small size, in both planes simultaneously.

The final focusing is achieved by the triplet quadrupoles (Q1, Q2 and Q3). The beam size is largest within the Q3 dipoles, where the beta function will reach up to 22 km, compared to the collision point where the beta function will be 15 cm (HL-LHC optics). It should also be noted that the triplet quadrupoles contain the largest beta functions in the whole accelerator, which is generally true for any collider.

2.8.1 Luminosity

In order to achieve a high statistical significance of the interactions that one is looking for in the collisions, one needs to maximize the reaction rate R. This reaction rate depends on two parameters, the *cross section* σ (not to be confused with the beam size) and the *luminosity* L. The former is an interaction-specific parameter, giving the probability that the specific reaction between two colliding particles will occur under certain initial conditions, whereas the latter is a beam-specific parameter, giving the macroscopic probability that collisions occur.

In a collider, this leads to the following equation:

$$R = \sigma L = \sigma \frac{n_b f_{rev} 2 N_p}{4 \pi \sigma_x \sigma_y} \tag{2.25}$$

where n_b is the total number of colliding bunches per beam, f_{rev} the revolution frequency of the beam, N_p the bunch intensity, and $\sigma_{x,y}$ the transverse beam sizes. While the cross section, σ, is set by the laws of nature (for a given beam energy), the luminosity depends solely on the design of the collider, and the goal is normally to maximize it. The number of bunches is intrinsically bound to the revolution frequency; in a large accelerator, more bunches can fit, but the revolution frequency also decreases. Given a length of the accelerator, the goal is thus to put as many bunches in as is practically possible, which at first order depends on the length of the machine and the number of RF buckets, that is, the frequency of the accelerating RF.

The bunch intensity and the beam sizes are more flexible than the bunch number, and the goal of the High Luminosity LHC is to increase the bunch intensity, while decreasing the beam size in the collision points, in order to maximize the luminosity.

2.8.2 Beam-beam effects

Since both beams in a collider consist of charged particles, they exert a kick on each-other as they traverse the collision point. The kick due to a bunch with a gaussian proton distribution is shown, for HL-LHC beam parameters, in Fig. 2.13, and is given by:

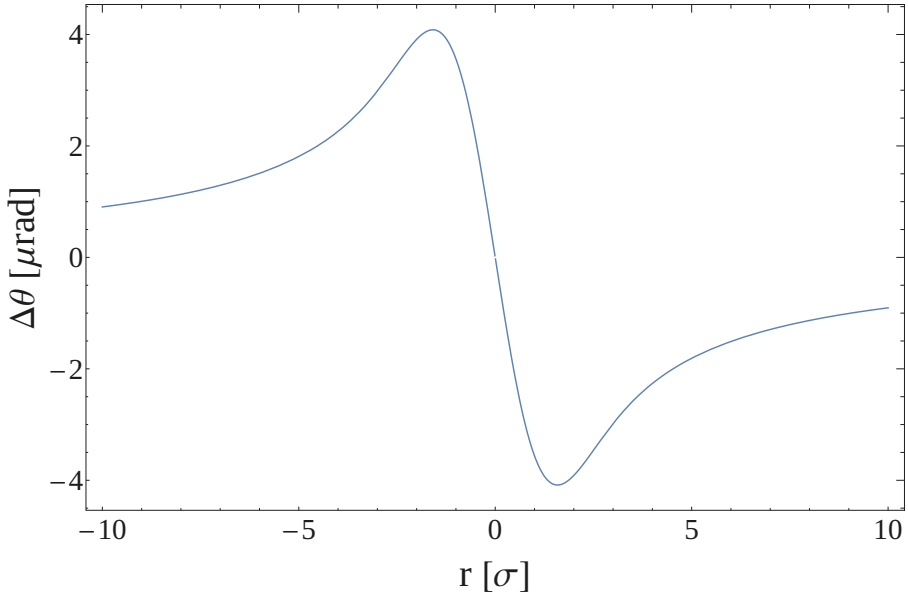

Figure 2.13. The beam-beam kick on a test charge at a varying displacement around a gaussian bunch.

$$\Delta\theta = -\frac{2nr_0}{\gamma_r}\frac{1}{r}\left(1-\exp[-\frac{r^2}{2\sigma_{x,y}^2}]\right) \tag{2.26}$$

where n is the bunch intensity, γ_r the Lorentz factor, r the beam separation and $\sigma_{x,y}$ the transverse beam size, here assumed to be the same in both planes (*round beams*). The classical particle radius r_0 is calculated from the elementary charge e, the vacuum permittivity ε_0 and the proton mass mc^2 through:

$$r_0 = e^2/4\pi\varepsilon_0 mc^2 \tag{2.27}$$

The kick is highly non-linear for large beam separations. Close to the center, the slope is however approximately linear, and the beam-beam effect for bunches that are close to each other acts as a quadrupole field, giving a focusing or defocusing effect.

For larger beam separations, the effect instead acts as a coherent transverse kick, which can perturb the orbit of both beams throughout the machine. Both of these effects are compensated for using magnets and by having the ATLAS and CMS crossings in alternating planes. The nonlinear parts of the kick also leads to a decreased beam quality, with e.g. an emittance growth over time.

3. CERN accelerator complex

The goal of this chapter is to introduce the reader to the CERN accelerator complex, with a focus on the LHC and its upgrade to HL-LHC, since that is where most of the studies presented in Chapter 5 belongs. Some experiments, presented in Paper IV, were done in the Super Proton Synchrotron (SPS). The LHC is introduced in detail, including an overview of how the machine protection system is built and functions.

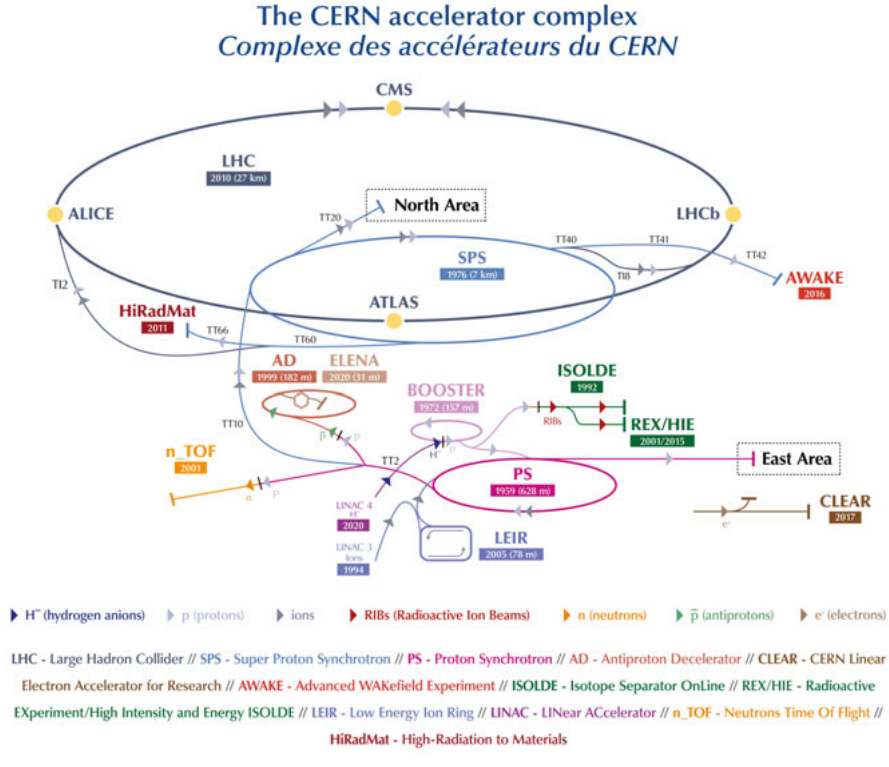

Figure 3.1. The CERN accelerator complex as of 2020 [27]. This includes the newest addition, LINAC4.

The full accelerator complex at CERN is shown in Fig. 3.1. Hydrogen anion beams are created in the Linear Accelerator (LINAC) 4 and are sent towards the proton synchrotron booster (PSB), where a thin foil strips off the electrons

to produce proton beams. The PSB consists of four rings stacked on top of each other. Once all four rings are filled with beam, they are sent towards the proton synchrotron (PS) and combined into a single beam. It takes two injections from the PSB to the PS to fill it. After the PS is filled, the beams are accelerated and extracted towards the super proton synchrotron (SPS), which requires a total of four injections from the PS to be filled. The beams are then accelerated to 450 GeV, the injection energy of the LHC [28]. Note that LINAC4 is a new addition, replacing LINAC2 as of 2021.

3.1 LHC

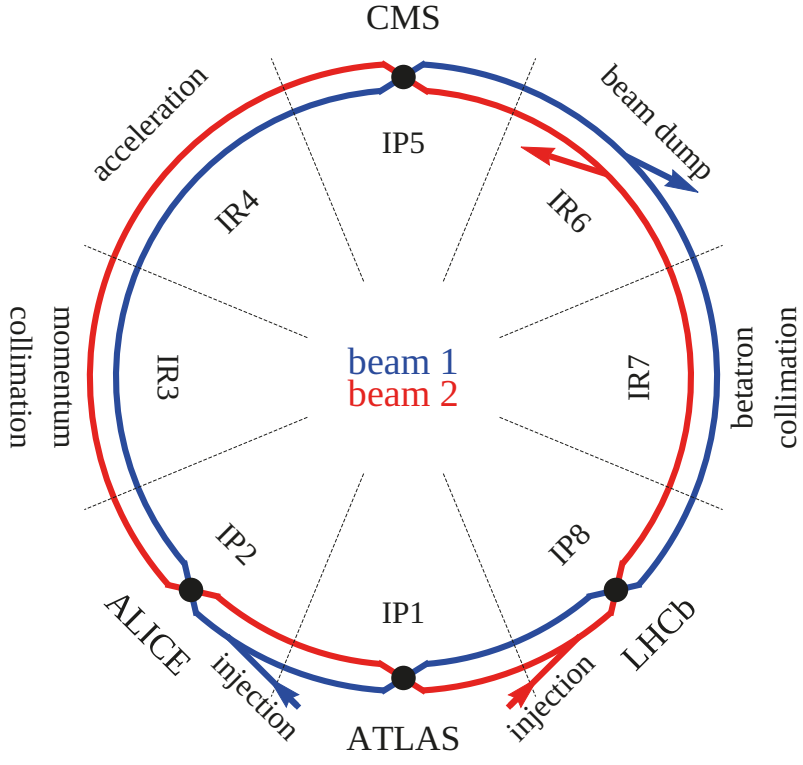

Figure 3.2. Top-view schematic of the LHC.

The large hadron collider (LHC) [13] is an almost 27 km long synchrotron capable of accelerating its two counter-circulating proton beams from an injection energy of 450 GeV to 7 TeV, where they are usually colliding for about half a day. This energy means that the beams are practically moving at the speed of light, and it takes about 88.924 μs for them to circulate once. This

is known as an *LHC turn*, hereinafter simply referred to as *turn*. A top-view schematic is shown in Fig. 3.2. It has an eight-fold symmetry, with eight arcs, consisting of standard FODO cells composed of 1x focusing quadrupole, 3x dipoles, 1x defocusing quadrupole, 3x dipoles. The dipole magnets number 1232 throughout the machine, are 14.3 m and have a maximum field of 8.33 T. The 858 quadrupole magnets are 3.3 m long and have a field gradient of 223 T/m. Aside from these, there are various specialized dipole and quadrupole magnets, as well as several thousand higher order magnets for correcting the field quality of the main dipoles and overall optics. The latter includes sextupoles for correcting chromaticity and octupoles for damping beam instabilities [29].

There are also eight insertion regions (IR) that are mostly straight. The IRs are where the beams can be manipulated or interact with each other. Four of the IRs have collision points, so called interaction points (IPs), designated IP1 (ATLAS), IP2 (ALICE), IP5 (CMS) and IP8 (LHCb). IPs 1 and 5 are the locations of the general purpose experiments, where the luminosity is maximized by having the smallest β^*, whereas the beam parameters in IPs 2 and 8 are not pushed as far. The IRs contain different types of magnets depending on the purpose of the IR, and they also contain mostly field-free drift spaces, in particular in the IPs where the drift spaces are up to 46 meters long.

The accelerating RF cavities are placed in IR4, and the beam extraction systems (*beam dumps*) are located in IR6.

Beam cleaning is done in the two collimation regions, IRs 3 and 7. IR3 has the momentum collimation, where particles with too large offsets in energy from the reference particle are removed from the beam. IR7 is focused on betatron collimation, where particles with too large transverse offsets are removed. Betatron collimation accounts for by far the largest proportion of collimated beam losses. Furthermore, since only transverse motion risks causing intense beam losses on short timescales, this thesis is focused on the IR7 collimators.

3.1.1 Filling Scheme

The nominal filling scheme of the LHC is described in [30]. The harmonic number, that is, the number of RF buckets, in the LHC is 35640. Each RF bucket is 2.5 ns long. Only every tenth bucket is available for bunches, meaning that there are 3564 possible bunch slots, and consequently a bunch spacing of 25 ns. Furthermore, there is always an *abort gap* of at least 3 μs, corresponding to about 120 bunch slots. The purpose of the abort gap is to allow the extraction kicker magnets of the beam dumping system to reach full voltage when the beams need to be extracted. Without this gap they would kick parts of the beam into the aperture. A gap of 0.95 μs is also necessary between separate batches (one batch is one full SPS beam) to allow the injection kicker

magnets to reach full voltage. The intermediate accelerators in the chain up to the LHC also require certain bunch-free gaps for similar reasons, and in the end there can be a maximum of 2808 colliding bunches per beam in the LHC according to the nominal design. By this date, this has however not been achieved and the maximum number of colliding bunches thus far is 2556. HL-LHC is to have 2748 bunches, out of which 2736 in each beam are colliding.

At the start of each LHC cycle, a so called *pilot bunch*, a single low-intensity bunch of $\sim 1 \times 10^{10}$ protons is injected into each of the beams. The purpose is to ensure that the optics in the machine are set correctly and that beams can circulate safely [31]. After that, a train of twelve nominal bunches (1.2×10^{11} protons per bunch in LHC during 2018) is injected into each beam. Their purpose is to check the correct setting of the transfer line and injection region before high intensity beams are injected, using the same optics and cycle in the SPS. They also provide certain diagnostics throughout the full cycle and were e.g. used for the beam-dust particle interaction studies presented in Paper II.

Lastly the full beams are injected. This is done with a minimum of ten injections from the SPS, per beam. At the fastest, there can be about one injection per 17.86 s, meaning about six minutes to fill the LHC. However, normally only every second SPS cycle is dedicated to the LHC and there can be more than ten injections per beam depending on the filling pattern. Once full, the energy is ramped. Operationally this is achieved by increasing the currents in the dipole magnets such that the orbit length changes (see Sec. 2.7). All in all, the energy ramp takes about 25 minutes.

In Fig. 3.3 a plot of one LHC fill is shown, showing what a cycle looks like. Plotted is the total beam intensity over time for the two beams, as well the beam energy. One can see a total of 20 injections per beam, with the first one being much smaller than the others since it is the 12 bunch train. After all injections are done, the magnet current ramps up to the value corresponding to a beam energy of 6.5 TeV. After this, the beams are *squeezed*, i.e., focused to collision parameters. The initial separation of the beams in the collision points is removed and the beams start colliding, indicated by the continuous drop in beam intensity. The beams are then finally dumped, indicated by the sudden drop in intensity, which is closely followed by a ramp-down of the magnet currents.

3.1.2 Machine Protection Systems

The machine protection systems are composed of active and passive components [32]. Passive protection deals with diffusing and absorbing beam losses, while active protection detects and acts on abnormal beam conditions to trigger the extraction of the two beams.

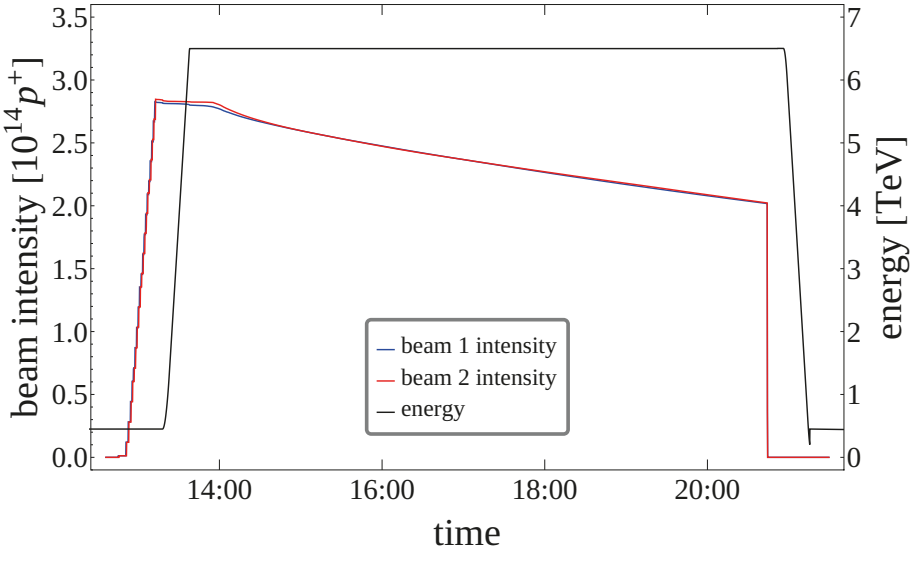

Figure 3.3. Plot of a typical LHC fill, with beam intensities (blue and red) and beam energy (black).

Passive Protection

The collimators in IRs 3 and 7 define the limiting aperture in the LHC. Particles with large offsets are captured, diffused and absorbed by the collimation system before they are lost elsewhere where they could cause e.g. magnet quenches. If the beam is perturbed, the transverse oscillations lead to beam losses at the IR7 collimators.

The LHC employs a three-stage collimation system [33–37], consisting of primary and secondary collimators, as well as tertiary collimators, depicted in Fig. 3.4. The primary collimators have the tightest aperture, about 2 mm, and are normally first to intercept particles with a large amplitude. The particles are then diffused and spread further, until they hit the secondary collimators where they are diffused further. They are finally absorbed in elements distributed throughout the accelerator, in particular the tertiary collimators, which protect the final focusing triplet magnets around the IPs. The tertiary collimators also protect the aperture of the triplet magnets against direct beam losses. Together, the collimators cover all the phase advances of the betatron motion, such that beam losses always occur in the collimation system first.

There are also absorbers installed downstream of the injection and extraction kicker magnets, to absorb beam losses due to misfiring of the respective magnets. The dump absorbers are particularly important as they absorb losses due to asynchronous beam dumps, that is, when the extraction kicker magnets are not correctly synchronized with the particle free abort gap.

The collimator apertures are set in units of RMS beam size σ, and are centered around the beam orbit. The aperture in millimeters can thus vary if the

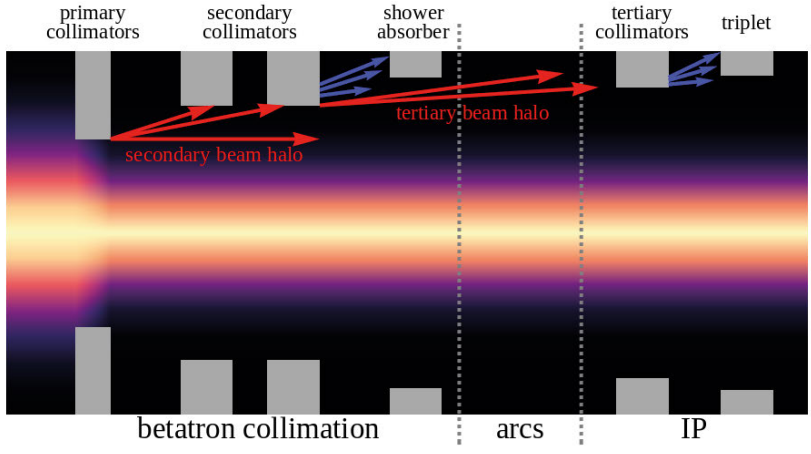

Figure 3.4. Schematic of parts of the LHC collimation system. The primary collimators clean the tails of the beam distribution, scattering protons into the secondary collimators. There they are scattered further and eventually end up in the tertiary collimators, where they are absorbed. Particle showers are also created, with some losses reaching the triplet magnets.

beta function changes, but the effect that they have on the beam depends on the beam size in relation to the gap. The gap settings for selected collimators is shown in Table 3.1.

Table 3.1. *Nominal settings in units of RMS beam size σ of selected collimator gaps in Run II and HLLHCv1.3 optics, assuming a normalized emittance of* $2.5\,\mu\text{m}\cdot\text{rad}$*, in collision optics [38]. The settings apply equally in horizontal, vertical and skew setups.*

Element	Run II	HL-LHC
IR7 primary collimators (TCP)	5.9	6.7
IR7 secondary collimators (TCS)	7.7	9.1
IR6 dump absorbers (TCDQ)	8.6	10.1
IP1/IP5 tertiary absorbers (TCT)	9.2	10.4
Triplet aperture (IP1)	10.4	11.2
Triplet aperture (IP5)	10.4	11.5

As explained in detail in Paper I Fig. 2, a **beam loss threshold** has been defined to the amount of protons that would impact the primary collimators for **beam orbit excursions of $1.5\,\sigma$**, with HL-LHC parameters. This corresponds to $\mathbf{1}\,\boldsymbol{MJ}$ of energy deposited into the collimation system. Orbit excursions resulting from failures should thus remain below this value.

Active Protection

The LHC has a vast number of distributed systems dedicated to the active protection of the machine [39]. Some of the main systems are introduced here. The information from the different systems is combined by the Beam Interlock System (BIS), which ensures that the LHC Beam Dumping System (LBDS) is activated, such that the beams are safely extracted from the LHC, in case a protection system detects an issue. This is known as a *beam dump*.

The Quench Protection System (QPS) in combination with the Powering Interlock Controllers (PIC) protect the superconducting circuits and magnets against damage and ensure the safe extraction of the stored energy in the circuits in case of a problem. The discharge of a critical circuit additionally triggers an extraction of the beams.

Fast magnet current change monitors (FMCM) ensure the fast detection of a powering failure in critical warm circuits, such as the IP1 and IP5 separation dipoles, and initiate the extraction of the beams. The other normal conducting magnets are protected by the Warm magnet Interlock Controller (WIC), detecting overheating in the magnets and issuing a beam dump in case of powering failures.

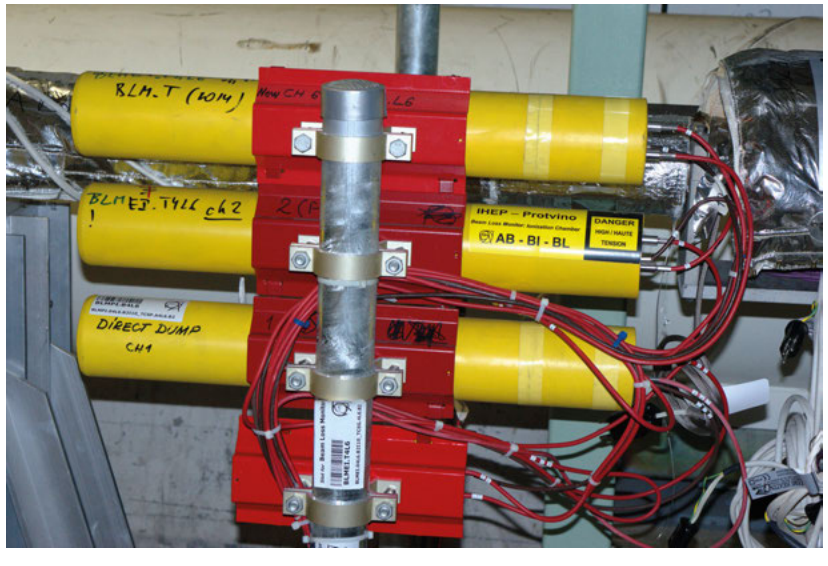

Figure 3.5. Three ionization chamber beam loss monitors (ICBLMs).

The beam loss monitoring (BLM) system [40] detects beam losses and request a beam abort, if a certain threshold is crossed. It consists of about 3700 ionization chamber BLMs (ICBLMs), distributed throughout the machine. Shown in Fig. 3.5, they are yellow gas filled cylinders that detect the ionization due to particle showers arising from beam losses. They have a sensitivity over several orders of magnitude and they are simultaneously integrated in time windows of varying length, the shortest being 40 μs, about half

an LHC turn of 89 μs. The BLM system has been designed to provide local protection of accelerator equipment against damage, as well as to provide a global protection of the machine through monitoring of losses via the IR7 collimators. In the latter case the source of the failure can be anywhere in the LHC [32]. While the BLM system constitutes a full safety net for failure detection, the general philosophy is to detect failures at their source and execute a beam dump before significant beam losses are created.

The beam current change monitor (BCCM) [41] is a new system to be installed, which complementary to the BLMs detects global beam losses, by measuring changes in the beam current.

There are also diamond Beam Loss Monitors (dBLMs). These consist of gold plated thin (100 μm and 500 μm) diamond films of one square centimeter. Due to fast signal rise and fall times (order of nanoseconds) they are capable of distinguishing the losses from individual bunches. These are used for various diagnostics purposes and are not interlocked [42, 43].

All these parameters that are being monitored, that can lead to a beam dump when abnormal values are detected, are said to be interlocked. Due to the extensive monitoring, it is also possible to reconstruct in detail what preceded a specific beam dump. All this data is saved in the post-mortem system [44].

There is also a Software Interlock System (SIS) which can execute more complex interlocking based on data from various systems, e.g. by measuring the beam orbit throughout the machine. The SIS feeds into the BIS in order to extract the beams.

Beam dump

The LHC beam dumping system (LBDS) handles the safe extraction of the beams. It is highly reliable and consists of two redundant systems running in parallel, since it provides the only means of safely removing the beam energy on a short timescale. Each beam is dumped onto a robust graphite block through the activation of 15 horizontally deflecting *kicker* magnets [45, 46]. This sends the beam into 15 stronger vertically deflecting *septum* magnets which are constantly powered, in order to separate the beam enough from the nominal orbit and into the beamline leading to the external beam dump. In this beamline, the beam is defocused by a *diluter* quadrupole, and kicker magnets with a time-varying horizontal and vertical field disperse the bunches of the beam onto different trajectories. The reason for this is that the beam dumps cannot handle a fully focused beam. All of these magnets and kickers are consequently interlocked, since a failure of the beam dumping system would be a highly critical scenario [47].

Magnet protection

In the LHC, most magnets are superconducting. When they *quench*, i.e. lose their superconductivity and become resistive, the large currents of over 10 kA start depositing energy in the resistive zones. Usually a resistive zone starts

small and develops naturally, eventually quenching the whole magnet. However, this *quench propagation speed* is normally not fast enough to compensate for the joule heating and a local hot spot develops [48]. To prevent damage to the superconducting wires and the wire insulation, active protection of the magnets is thus necessary.

The voltage over the superconducting circuits is continuously monitored. If an interlock is triggered, a signal is sent to the BIS to extract the beams, and the magnet protection is activated. The latter consists of several parts; bypass diodes protect the quenching magnet from the stored energy in the circuit, which contains several magnets, while energy extraction switches remove the current from the circuit to prevent damage to the bypass diode [49]. Quench heaters [49] are simultaneously activated to protect the magnet. These are resistive films attached to the outside of the magnet coils, running along the full length of the magnet. A pre-charged capacitor bank is discharged into them, heating the whole magnet. This quickly brings it from superconducting to normal conducting, such that the current is deposited throughout the whole mass of the magnet. A novel system for magnet protection called Coupling loss induced quench (CLIQ) will also be implemented for the IP1 and IP5 triplet magnets in HL-LHC. This is detailed in Sec. 5.1.

Reaction Time

There are four fiber optic cables going in opposite directions around the perimeter of the accelerator, two per beam. If one of them stops transmitting a signal, constituting the *beam permit*, detectors in the dump region, IR6, will detect this and initiate the beam dumping procedure. The optical fibres can be cut by equipment distributed throughout the eight straight sections, once some equipment in that octant triggers an interlock. There can be a delay of up to $100\,\mu$s from the moment the optical fiber is cut until the beam dump procedure is initiated.

Once initiated, the abort gap needs to be synchronized with the beam extraction kickers. This can take one turn, or $89\,\mu$s. It then takes up to another full turn until the beams are dumped. All in all, from the time that the BIS triggers a beam dump, there can thus be a delay of $278\,\mu$s, or about three turns.

Before the BIS can trigger a beam dump, the failure must be detected. How long this takes depends on the design of the system detecting the failure. The fastest are the proposed RF interlock for the crab cavities, at $15\,\mu$s. The fastest system in the current LHC is the fast magnet current change monitors at $20\,\mu$s and BLMs at $80\,\mu$s. In general, this works in the way that some threshold value is set for various detectors and parameters. If the threshold value is breached, and for most systems, is sustained over a certain amount of time, in order to not trigger on spurious noise spikes, the interlock is activated and the BIS is signaled to dump the beams. At least a few LHC turns is necessary for this evaluation. Taking the fixed delays into account, it is required from machine

protection that no failure causes critical beam losses on shorter timescales than ten LHC turns or about 1 ms.

The software interlocks of the SIS are considerably slower than the hardware interlocks that feed directly into the BIS. Consequently the SIS is used for less critical systems, that cannot produce fast beam losses.

3.2 HL-LHC

A summary of the HL-LHC beam parameters is presented in Table 3.2 and compared to the LHC era parameters. The goal is to increase the luminosity by a factor of eight as compared to the current LHC. This is mainly achieved through an increase of the nominal bunch intensity, from current 1.2×10^{11} protons to 2.2×10^{11} protons. The beta function in the collision points (β^*) is also decreased from 25 cm to 15 cm, providing smaller beams, since the beam size depends on the beta function in accordance with Eq. 2.17.

Following Eq. 2.24, the beta function in the drift space surrounding a collision point is closely linked to the β^*, the minimum beta function in the collision point. The decrease in β^* thus leads to an increase in the beta function around the IP, up to a maximum of about 22 km in the triplets, compared to the maximum value of about 9.6 km for the LHC Run III in 2018. This increases the beam-beam effects, which are detrimental for the beam quality. Thus, to reduce the beam-beam effects, the beams must be separated more than in the current LHC. The crossing angle will be increased from 162 to 295 μrad. This, together with the increased bunch size in the triplets, necessitates a replacement of the final focusing triplets for IP1 (ATLAS) and IP5 (CMS) by new magnets [52]. The new triplet magnets will have an increased aperture from the current 70 mm to 150 mm, with a decreased gradient from 200 T/m to 132.6 T/m [52].

The separation and recombination dipoles (D1 and D2) for IPs 1 and 5 will also be replaced [52]. They are currently resistive, but will become superconducting in order to accomodate space for other equipment. There are more magnets that will be replaced around these IPs, but they are not relevant in view of this thesis and therefore not discussed.

Another consequence of the increased crossing angle is that the bunch overlap in the collision point decreases, see schematic in Fig. 3.6(a). This reduces the luminosity, calculated from Eq. 2.25, through the so called geometric reduction factor F:

$$F = \frac{1}{\sqrt{1 + \left(\frac{\theta_c \sigma_z}{2\sigma_t}\right)^2}} \tag{3.1}$$

where θ_c is the total crossing angle, σ_z the longitudinal bunch size and σ_t the transverse bunch size. With a crossing angle of 130 μrad in the current

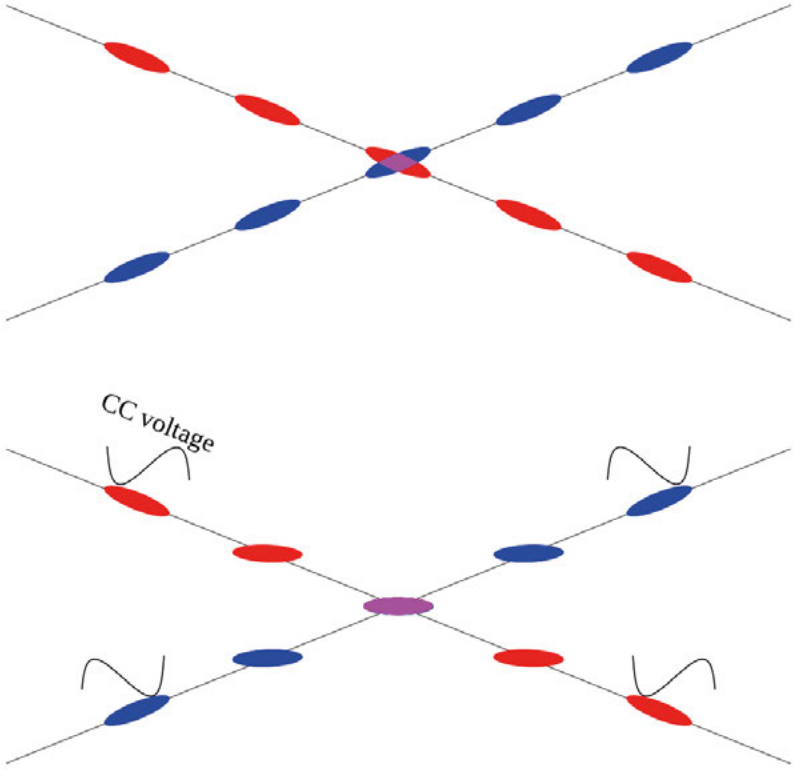

Figure 3.6. Schematic of the crossing point, showing the overlap of the bunches in magenta, without crab cavitites (a) and with crab cavities (b). The crab cavities tilt the bunches such that the overlap becomes better.

LHC, the reduction factor is about 0.7, meaning a 30% reduction of the luminosity as compared to head-on collisions. In the HL-LHC, this factor will instead become 0.3 and must be compensated. This is done through specialized RF cavities known as *crab cavities* [53]. As depicted in Fig. 3.6(b), this is done by applying a modulated transverse kick to the bunches. The bunch tails are thus rotated around the center of the bunch, such that they are tilted in the collision point, increasing the overlap. The resulting bunch profile in the IP is compared to a non-crabbed bunch in Fig. 3.7. The crab cavities are expected to compensate up to 190 μrad, while the crossing angle is $\pm 295\,\mu$rad [54].

The kick that the crab cavities impart on a bunch is given by:

$$\begin{aligned} \Delta x' &= -\frac{qV_0}{E}\sin[\varphi_{cc} + \omega_{cc}t] \\ \Delta p_z &= -\frac{qV_0}{E}\frac{\omega_{cc}}{c}\cos[\varphi_{cc} + \frac{\omega_{cc}z}{c}]x \end{aligned} \tag{3.2}$$

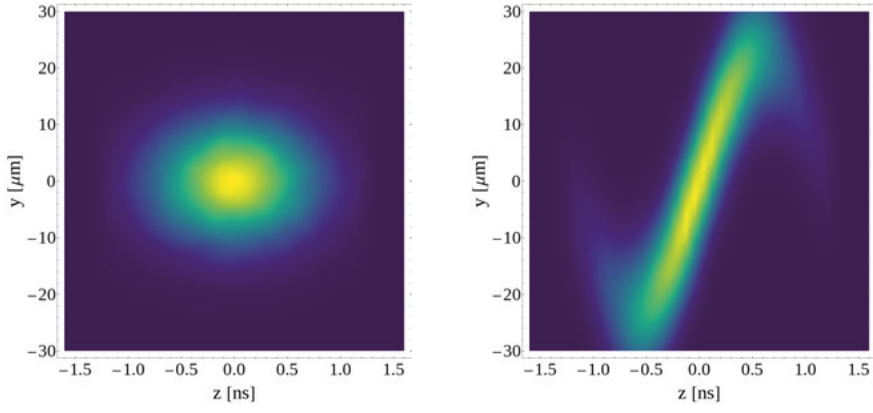

(a) **(b)**

Figure 3.7. Vertical vs longitudinal bunch profile in IP5 for a non-crabbed bunch (left) and crabbed bunch (right). The longitudinal tails were artifically enhanced to better illustrate the difference. A crab cavity voltage of $2 \times 3.4\,\mathrm{MV}$ was used.

where q is the charge, V_0 the voltage of the cavities, E the beam energy, φ_{cc} the phase of the cavity, ω_{cc} the angular frequency of the cavity and t the time. The kick is aligned either horizontally or vertically, and is equivalent in the different planes. Regardless of transverse plane, there is also an effect on the longitudinal plane, but this kick is small.

There will be two crab cavities per beam per side of IP1 (ATLAS) and IP5 (CMS). One of the IPs will have double quarter wave-type cavities [55], while the other will have RF dipole-type cavities [56]. The crab cavities on the side of the incoming beam crab the bunches, whereas the crab cavities on the opposite side of the IP uncrab the bunches. This makes the crabbing locally limited to the collision points.

Table 3.2. *Comparison of some of the optics parameters in LHC Run II [50], Run III [51], nominal LHC [13] and HL-LHC (HLLHCv1.4 [26]). The crossing orientations are Vertical (V) or Horizontal (H). SB refers to stable beam, meaning colliding beam optics. The emittance is the reference value for the particular optics. In reality it has been smaller, down to* 1.8 µm rad *in 2018.*

	Run II (2018)		Run III		LHC design	HL-LHC	
	Start SB	End SB	Start SB	End SB	Round	Round	Flat
β^* IP1 [cm]	30	25	105	30	55	15	7.5/30
β^* IP2 [cm]	1000	1000	1000	1000	1000	1000	1000
β^* IP5 [cm]	30	25	105	30	55	15	7.5/30
β^* IP8 [cm]	300	300	150	150	100	150	150
crossing IP1 [µrad]	130 V	130 V	109 V	162 V	143 V	295 H	245 V
crossing IP2 [µrad]	125 V	125 V	200 V	200 V	150 V	270 V	270 V
crossing IP5 [µrad]	130 H	130 H	109 H	162 H	143 H	295 V	245 H
crossing IP8 [µrad]	395 H	395 H	250 H	250 H	200 H	115 H	115 H
bunch intensity [10^{11} p$^+$]	1.2	1.2	1.8	1.2	1.15	2.2	2.2
ε_n [µm rad]	2.5	2.5	2.5	2.5	3.75	2.5	2.5
energy [TeV]	6.5	6.5	6.5/7	6.5/7	7	7	7
max β_x [m]	8061	9638	2361	7827	4403	21591	43267
max β_y [m]	8046	9637	2364	7835	4403	21542	43177

4. Failures

This chapter introduces failures on a general level, in preparation for the specific failure studies presented in Chapter 5.

Failures are any kind of event capable of causing uncontrolled beam losses. These can arise from incorrect equipment behavior or operational manipulations that are either unintended or that can have unintended consequences on the beam. Typical examples are powering failures and beam instabilities. If for example a dipole magnet loses power, the beam will start drifting out of orbit together with the current decrease, eventually hitting the physical aperture. Current decays in resistive magnets are on the order of seconds [57], which for the beam is a very long time, since **one LHC turn is 89 μs**. Nevertheless, it can be enough with just a small fraction of current decay to cause critical beam losses, for example in the IP5 separation dipole magnet, where the equivalent of a nominal bunch is lost in 19 turns after a power cut [57].

Failures are in this thesis classified by the time in which they develop and can produce unacceptably high beam losses, as follows:

> **Ultra-fast failures:** These are faster than 270 μs (three LHC turns) and thus faster than the reaction time of the machine protection systems, which requires at least three turns to safely extract the beams. Only passive protection can protect the machine if this kind of failure occurs
> **Fast failures:** These are faster than 10 ms
> **Slow failures:** These are slower than fast failures

The focus of this thesis lies on Fast and Ultra-fast failures. There are two important aspects related to failures, one is their consequence on the machine, its components, the resulting downtime and associated costs. The other is how probable a given failure is. Quantifying the probability that a failure occurs is possible through e.g. Monte-Carlo simulations [58, 59], but is outside the scope of this thesis. In this thesis the focus lies on analyzing and quantifying the consequences. Only a qualitative assessment on the probability of failure is done, in order to only include realistic failure scenarios.

Impact on the beam

The two main impacts on the beam that are critical in view of fast failures are transverse beam offsets and changes in the beta function, so called *beta beating*. Beam offsets can be created by any transverse kicks, arising from electrical fields or dipolar magnetic fields. Higher order magnetic components

can also give beam offsets if the beams are not centered in these magnets. This is e.g. the case in the final focusing triplet magnets, where the beams can be offset by over 10 mm. If the phase advance is such that the kicks give rise to transverse offsets at the aperture bottlenecks, mainly the primary collimators (TCPs), direct beam losses will follow.

Beta beating is a consequence of a change in the focusing gradients. For example if a quadrupole magnet has a change of current. As for transverse kicks, beta beating can also come from higher order fields if the beams are offset in the magnet. Due to the beating, the beam size throughout the accelerator is modulated, and if e.g. the beam size is suddenly increased in the TCPs, beam losses will occur. Another more complicated consequence of beta beating is that the hierarchy between the collimators and other aperture bottlenecks change. If e.g. the hierarchy between the extraction protection (dump absorber, TCDQ) and tertiary collimators (TCTs) is breached, asynchronous beam dumps would cause critical beam losses in the triplet magnets [60]. This could potentially be devastating.

4.1 Orbit offsets and kicks

The infinitesimal kick due to a magnetic field can be calculated from

$$d\alpha = \tan\left[\frac{Bds}{B\rho}\right]\sqrt{\frac{\beta(s)}{\varepsilon_g}} \approx \frac{Bds}{B\rho}\sqrt{\frac{\beta(s)}{\varepsilon_g}} \tag{4.1}$$

where $d\alpha$ is the normalized kick in units of RMS beam size σ, B the applied magnetic field, ds an infinitesimal length along the kicking element, $B\rho$ the magnetic rigidity of the beam, $\beta(s)$ the beta function at the kicker and ε_g the geometric emittance. The tangent function can be removed following the small angle approximation, since the considered kicks are generally on the order of microradians to milliradians. If the kick is instead due to an electric field, one need only replace B in the numerator with E/v, that is, the electric field over speed of the beam, which in the LHC is practically luminal.

Figure 4.1 shows a schematic of what happens with the orbit of the beam in relation to the reference orbit, after applying a kick. At the kicker location, the beam receives a sudden change in angle, giving sinusoidal oscillations around the reference orbit, driven by the phase advance of the betatron motion. The top plot shows a free oscillation of the horizontal offset. Since the LHC is a circular machine, the same beam comes back to the kicker but with a certain non-zero phase advance. If the kick is no longer present on the second turn, shown by the middle plot, the oscillation continues on with a different phase for each turn. By applying periodic boundary conditions, implying a new closed orbit, the bottom plot is attained.

The total number of oscillations in one turn is the betatron tune. In the plot, the tune is $Q = 6.41$, meaning that the oscillations do not add up perfectly. This

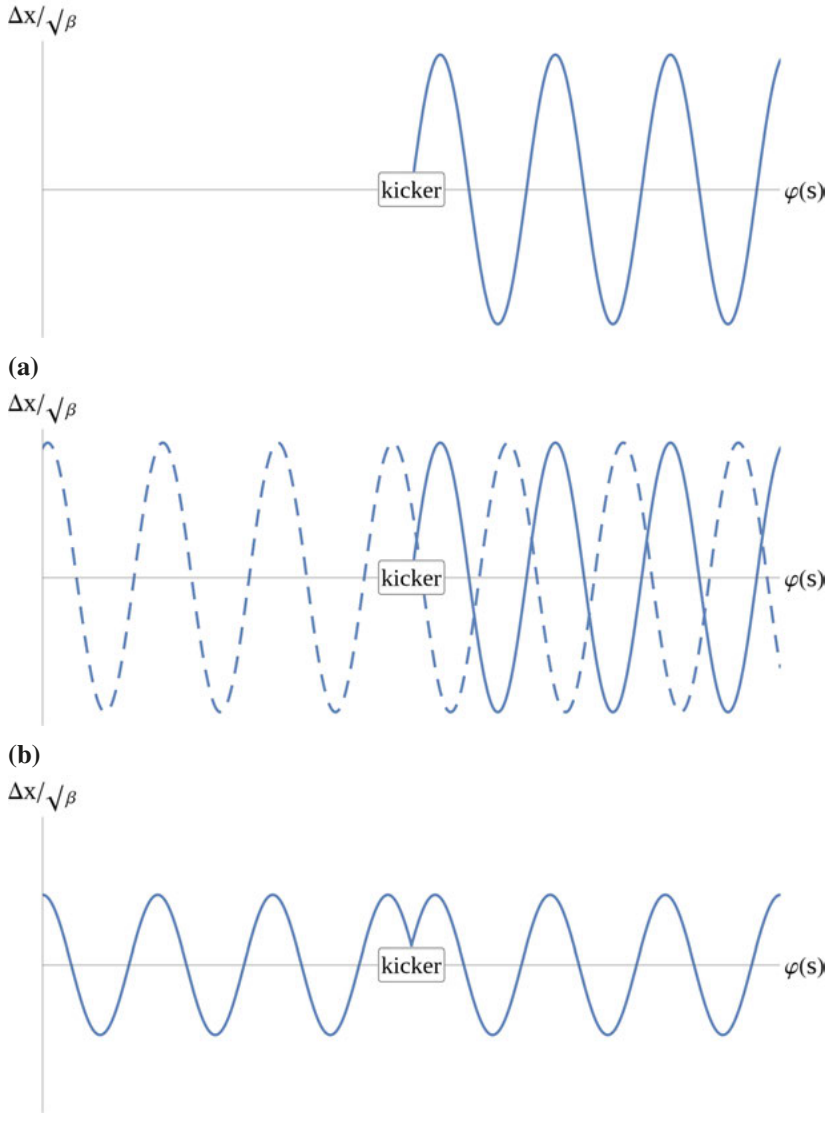

Figure 4.1. Effect of applying a kick to the beam at a certain location, with the horizontal displacement normalized to the beta function throughout a ring is plotted vs the phase advance. (a) evolution of the beam displacement directly after a single kick is applied (b) evolution of horizontal displacement for the first and second turns when the kick is only present on one turn (c) application of periodic boundary conditions, showing the equilibrium horizontal displacement for a static kick.

is by design; imagine that the fractional part of the tune were zero, then when the beam comes back to the kicker and receives a new kick, its angle would already be aligned with the kick. The beam thus resonates with the kicker,

gaining ever increasing amplitudes and quickly hits the aperture. Integer tunes must therefore be avoided, since otherwise any dipolar error in the machine would quickly push the beam into the aperture.

Similar resonances can occur with higher-order fields as well, such as e.g. quadrupole errors. Magnet errors are to a certain extent unavoidable and consequently the tunes must be adjusted such that all low-order rational numbers are avoided (1, 1/2, 1/3, 1/4, ...).

The transverse offset throughout the accelerator following a single-turn kick is given by:

$$\frac{x(s)}{\sqrt{\beta(s)}} = \Delta x' \sqrt{\beta(0)} \sin[\varphi(s) - \varphi(0)] \tag{4.2}$$

After applying periodic boundary conditions, one acquires the new *closed orbit*:

$$\frac{x(s)}{\sqrt{\beta(s)}} = \frac{\Delta x' \sqrt{\beta(0)}}{2\sin[\pi Q_x]} \cos[|\varphi(s) - \varphi(0)| - \pi Q_x] \tag{4.3}$$

where $x(s)$ is the resulting offset at position s, $\beta(s)$ the beta function, $\Delta x'$ the kick angle, $\beta(0)$ the beta function at the kicker, φ the phase advance and Q_x the horizontal betatron tune. For tunes $Q_x \to 0,\ 1,\ 2, \ldots$ this expression goes to infinity, due to the resonance.

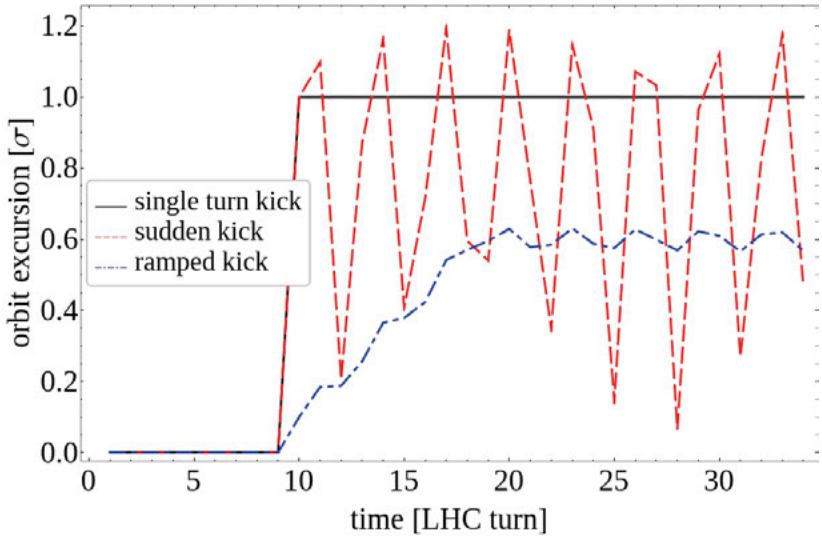

Figure 4.2. Comparison of the orbit excursion over time for three different types of kicks, with a normalized kick strength of 1 σ. For the solid line, the kick was applied on one single turn. For the dashed-dotted line, the kick was ramped over ten turns to full strength where it then remained, while for the dashed line, the kick was ramped to full strength in one turn where it remained.

Now, the question is how the onset of the kick, and whether it is static or transient, affects the beam. In Fig. 4.2 the *orbit excursion* over time, that is, the linear action of the beam normalized to units of beam size σ, is shown for three different types of kicks. The solid line corresponds to a normalized kick amplitude of $1\,\sigma$, that is present for only one turn and then disappears before the beam returns to the kicker. The beam will then follow a motion as depicted in Fig. 4.1 (b), that is, it will have a free oscillation around the nominal orbit with a constant maximum amplitude. This maximum amplitude corresponds to the action, and thus we can see that the action over time remains at $1\,\sigma$.

The dashed-dotted line (Fig. 4.2) also results from a normalized kick of $1\,\sigma$, but it is slowly ramped up to maximum strength where it then remains. This is the same as Fig. 4.1(c). That is, the beam lies on a new closed orbit (periodic boundary conditions), where the action remains constant at a value of $\frac{1\,\sigma}{2\sin[\pi Q_x]}$. This follows from Eq. 4.3 by adding a factor of $(\varepsilon_g)^{-1/2}$ on both sides, to normalize the displacement and the kick.

For the third case, the dashed line (Fig. 4.2), the kick is immediately switched to full power and then remains constant. In this case, since the beam returns to the kicker with a new angle every turn due to the fractional tune, the kick will sometimes act to enhance the angle whereas on some turns the incoming angle will be cancelled by the kicker, lowering the action of the oscillation. The beam will consequently oscillate around the *new* closed orbit, shown by the dashed-dotted line, with an amplitude corresponding to the difference between the new and old closed orbits.

This is better illustrated in Fig. 4.3, where the same three kicks are shown in phase space. The coordinates of one particle (or rather, the bunch center) are observed once per turn at the same location in the machine. For the single turn kick (black), the particle traces out a constant circle with a radius corresponding to the value in Fig. 4.2. As for the ramped kick (blue), it corresponds to a shift of the closed orbit, meaning that it should remain stable. Since it was ramped up over only ten turns, there is still some remnant oscillations, which is the reason for the small circle it traces out around the position of the new closed orbit.

As for the sudden kick (red), it oscillates around the new closed orbit and thus traces out a circle around the blue kick, with a radius corresponding to the difference between the new and the old closed orbits.

4.2 Beta beating

The beta function throughout the machine is determined by the focusing lattice. In case a focusing error occurs, the beta function changes such that an oscillation around the nominal value, or a *beating*, occurs. This can be calculated using the following equation:

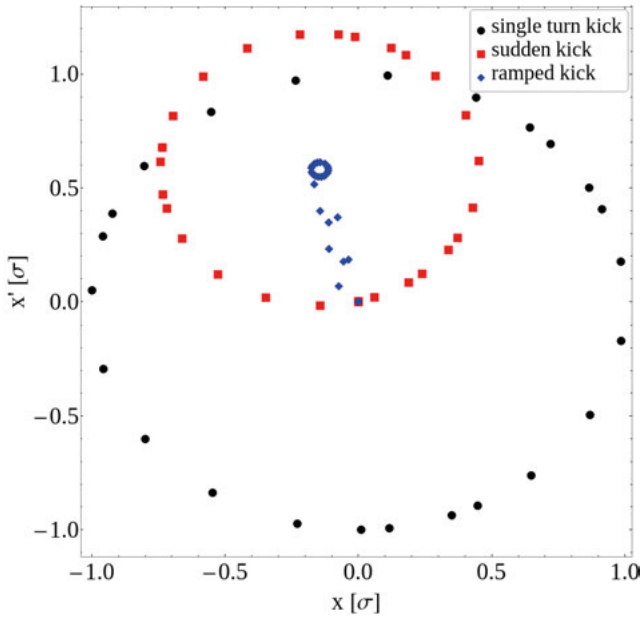

Figure 4.3. Phase space plot for the three kicks in Fig. 4.2. The kick of $1\,\sigma$ was active on a single turn for black dots, ramped over ten turns to full strength and remained on for blue dots, and ramped to full strength in one turn for red dots.

$$\frac{\Delta\beta(s)}{\beta(s)} = \frac{\Delta q \beta(0)}{2\sin[2\pi Q]} \cos[2|\varphi(s) - \varphi(0)| - 2\pi Q] \tag{4.4}$$

Note the factor of two inside the sinus function. This implies that there is a resonance for fractional tunes of $Q = 0,\ 0.5$. For half-integer tune, the beam will return with an opposite sign in its displacement x and angle x'. Resonance is thus driven by quadrupolar errors, since quadrupoles have symmetric magnetic fields around the center point.

The nominal quadrupoles have a gradient of $223\,\mathrm{T/m}$ [61]. If one of them, here chosen with a phase advance to the collimators that maximizes the effect, loses power such that the gradient drops by $72.3\,\mathrm{T/m}$, Fig. 4.4 results. The vertical beam size ($6.7\,\sigma$ envelope) in a small section of the LHC, close to the collimators in IR7, is shown. The solid black line shows the nominal value, whereas the dashed line shows the new beam size.

One can see that the beam size in this case is drastically increased inside the secondary collimators (position 13330 m), while it is decreased in the primary collimators (position 13125 m). This makes it such that the secondary collimators become primary and vice versa, which would have a detrimental effect on the efficiency of the cleaning of particles with too large transverse offsets.

Furthermore, if the beam size is instead increased in the primary collimators, there would be significant beam losses. Adjusting the collimator gaps

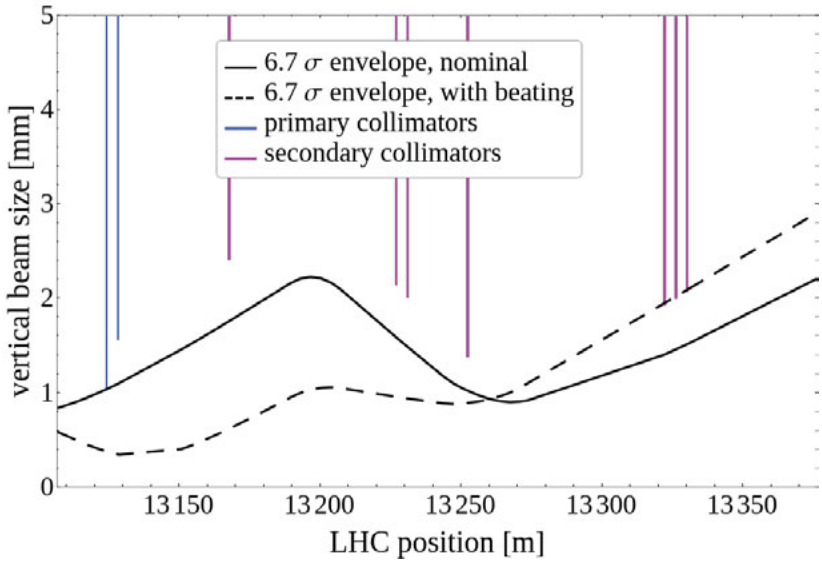

Figure 4.4. Comparison of beam size with and without beta beating around some collimators in the betatron collimation region, IR7. The $6.7\,\sigma$ beam envelope is set by the primary collimators, but with strong beta beating the effective settings of the different collimators can change such that the hierarchy between them is broken.

to compensate is a mechanical process, and thus slow. It is not done during operation and could not help against failures.

4.3 Scaling laws

As seen in Eq. 4.3, the effect that a kick has on the beam scales with the square root of the beta function, at the location of the error. Similarly, for focusing errors, the effect depends on the beta function at the source of the error as shown by Eq. 4.4.

The beta function thus acts as a lever, enhancing the sensitivity of the beam to perturbations. This is illustrated in Fig. 4.5, where a transverse kick of $5\,\mu$rad is applied on a bunch of particles inside of a focusing quadrupole (large beta function) to the left and a defocusing quadrupole (small beta function) to the right. Even though the change in angle is the same in both cases, one can see that the kick is much bigger in relation to the nominal angular spread in the bunch for the case where the beta function is large. Consequently, particles kicked where the beta function is large will trace out larger ellipses in phase space and have larger oscillation amplitudes. Due to this the final focusing triplet magnets are among the most critical magnets in the LHC, or any collider for that matter, since the beta functions are about a factor of 40 larger than the maximum values in the arcs (HL-LHC).

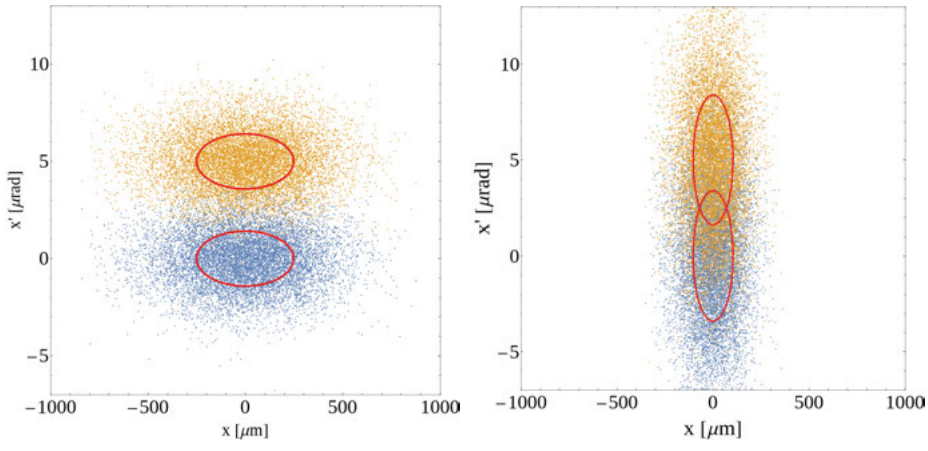

(a) **(b)**

Figure 4.5. Transverse kick of $5\,\mu$rad on a bunch of particles in a focusing (a) and a defocusing (b) quadrupole. Blue particles are before the kick and orange after the kick. Red ellipse corresponds to one σ.

As for the energy dependence, as seen in Eq. 4.1, the kick is inversely proportional to the magnetic rigidity and to the square root of the geometric emittance. These depend on the energy, and the net effect is that the kick is inversely proportional to the square root of the energy. That is, increased energy makes the beam less sensitive to perturbations.

5. Specific failure scenarios

In this chapter, the different fast failure scenarios that have been studied within the scope of this thesis are introduced and the main results of the respective studies are summarized. As explained in Chapter 4, fast failures are those that can produce critical beam losses within 10 ms. With the fastest interlocks, including margins for failure detection, the beams are **dumped within 10 LHC turns** (0.89 ms). This sets an upper limit for the acceptable severity of the different failure cases. More details of the failures described in this chapter are provided in the referred to papers. An overview of the failures is presented below:

Quench heaters are a part of the magnet protection and consist of resistive heaters attached to the magnetic coils. Their kicks on the beam in HL-LHC are analyzed in Paper I.

Coupling-loss induced quench is a novel system for magnet protection to be used in HL-LHC. They cause a strong oscillation of the electric current in the magnets, leading to very fast beam perturbations. These are studied in Paper I.

Triplet quenches, that is, quenches in the final focusing triplet magnets, can cause fast orbit perturbations and are studied in Paper I.

Transverse dampers are used to keep the beam stable and damp transverse oscillations, but they can also resonantly excite transverse beam oscillations. This is studied in Paper I.

Unidentified falling objects are sudden beam loss spike events caused by micrometer-sized dust particles interacting with the beam. These are analyzed in detail in Paper II and Paper IV.

Beam-beam kicks perturb the orbit of the beam that remains after only one of the two beams is dumped. This is studied for LHC Run III and HL-LHC in Paper I.

Beam-beam compensating wires are current-bearing wires designed to mitigate some of the effects of the beam-beam kick. These are summarized in Paper I.

Crab cavities are a new type of equipment for HL-LHC necessary for reaching the luminosity goal. They produce strong transverse kicks on the beam which can cause a fast orbit perturbation if they malfunction. These are studied in Paper III and Paper V.

5.1 Magnet Protection

As mentioned in Section 3.1.2, the superconducting magnets in the LHC need to be protected against damage when a quench develops. In HL-LHC, the following components are relevant for their impact on the beam:

Quench heaters (QH), resistive heaters attached to the outside of the magnet coils, heat up the magnets in order to speed up the quench propagation. The current consequently deposits the stored magnet energy over a larger volume, lowering the maximum hot-spot temperature.

Coupling loss induced quench (CLIQ), works by discharging an oscillating current directly into the magnet coil. This ac current induces eddy currents in the copper matrix, leading to a heating of the full magnet volume and is thus more efficient than the QHs, at high currents.

Both the QHs and CLIQ induce magnetic fields within the beam region. The effect this has on the circulating beam is analyzed in detail in Paper I.

Different methods were used for analyzing the QHs and CLIQ. For the QHs, analytical calculations were used, whereas MAD-X was employed for the CLIQ simulations.

5.1.1 Quench Heaters

The QHs ramp to their full current within half an LHC turn, and can thus be considered instantaneous kicks that remain static for multiple turns (the *sudden kick* in Fig. 4.2). The effect on the beam is consequently an oscillation around a new closed orbit, where the closed orbit follows Eq. 4.3. The maximum orbit excursion is a factor of two larger than the change in closed orbit.

The magnetic field in the magnetostatic solution can be calculated using the Biot-Savart law, by assuming the magnet mass and structure to consist of vacuum. This is valid because the iron yoke of the magnets is approximately saturated at nominal magnet currents. Furthermore, since the QH strips are located more than 100 mm radially away from the beam, they can be modeled as thin, infinitely long, current-carrying wires. The equation is:

$$\bar{B} = \begin{cases} -\frac{i\mu_0 I}{2\pi\sqrt{x_s^2+y_s^2}\exp[i\,\mathrm{atan2}[y_s,x_s]]}\left(1-\sqrt{\frac{x^2+y^2}{x_s^2+y_s^2}}\exp[i(\mathrm{atan2}[y,x]-\mathrm{atan2}[y_s,x_s])]\right)^{-1} \\ \frac{i\mu_0 I}{2\pi\sqrt{x^2+y^2}\exp[i\,\mathrm{atan2}[y,x]]}\left(1-\sqrt{\frac{x_s^2+y_s^2}{x^2+y^2}}\exp[i(\mathrm{atan2}[y_s,x_s]-\mathrm{atan2}[y,x])]\right)^{-1} \end{cases} \tag{5.1}$$

where $\bar{B} = B_x\hat{x} + B_y\hat{y}$, $\mu_0 = 4\pi\times10^{-7}\,\mathrm{H/m}$ is the magnetic permeability in vacuum, (x,y) is the observation point, (x_s,y_s) the location of the source and I the current in the source. The top equation is for $x^2+y^2 < x_s^2+y_s^2$, and the bottom equation for the complementary condition. $\mathrm{atan2}[y,x]$ is the 2-argument arctangent function.

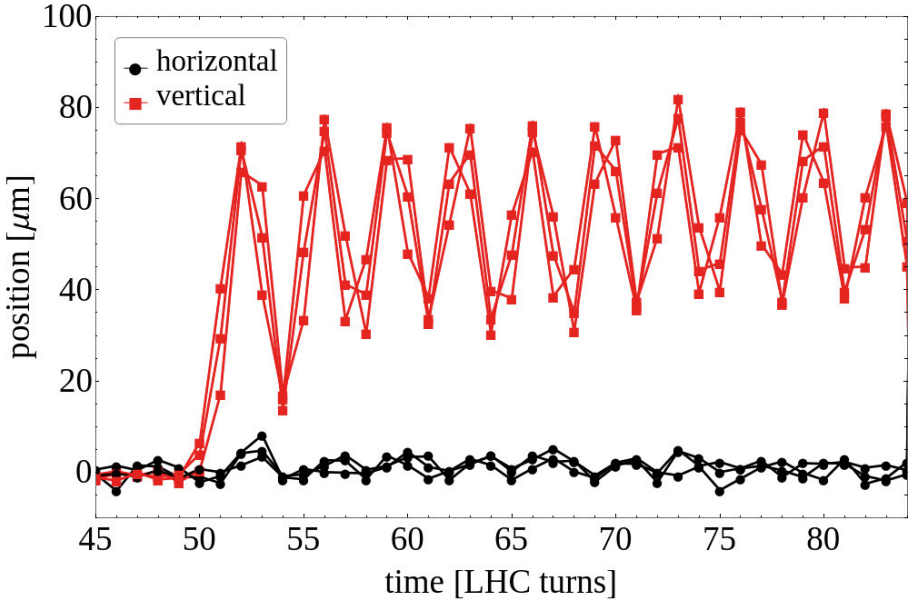

Figure 5.1. Measured horizontal and vertical bunch positions over time for three bunches following a QH discharge in a main dipole magnet (MB.C28L5).

These assumptions were experimentally validated by firing the QHs in a main dipole in the LHC with circulating beam at two different beam energies (3.46 TeV and 6.5 TeV). The lower energy case is shown in Fig. 5.1. The average oscillation amplitude is about 60 μm. The beta function at the beam position monitor (BPM) and the magnet that quenched was $\beta_y = 166.3$ m and $\beta_y = 137.12$ m respectively. The phase advance from the magnet to the BPM was 3.3434 rad. Putting this into Eq 4.3, one can calculate the kick:

$$\begin{aligned} \Delta y' &= \frac{y_{BPM} 2\sin[2\pi Q_y]}{\sqrt{\beta_{BPM}\beta_{QH}}\cos[\Delta\varphi - \pi Q_y]} = \\ &= \frac{60\times10^{-6}\cdot 2\sin[2\cdot 0.295\pi]}{\sqrt{166.3\cdot 137.12}\cos[3.3434 - 0.295\pi]} = 1.02\,\mu\text{rad} \end{aligned} \tag{5.2}$$

Using Eq. 4.1 with an effective magnetic dipole length of 14.8 m and a magnetic rigidity of $B\rho = 3.46\,\text{TeV}/c$, we find that this corresponds to 800 μT. The QHs in this case consist of two circuits with a total of four strips. They carry 80 A, and are placed at coordinates $(x, y) = (\pm 45\,\text{mm}, \pm 40\,\text{mm})$ around the beam. The magnetostatic flux density is thus 795 μT, as shown in Fig. 5.2. This is consistent with the simple estimate above. However, in all cryogenic parts of the LHC, the beam pipe is filled with a *beam screen* fully encompassing the beam [62]. One of the main purposes of this copper plated stainless steel screen is to shield the superconducting magnets from synchrotron radiation. This screen also shields the beam region from fast external changes in

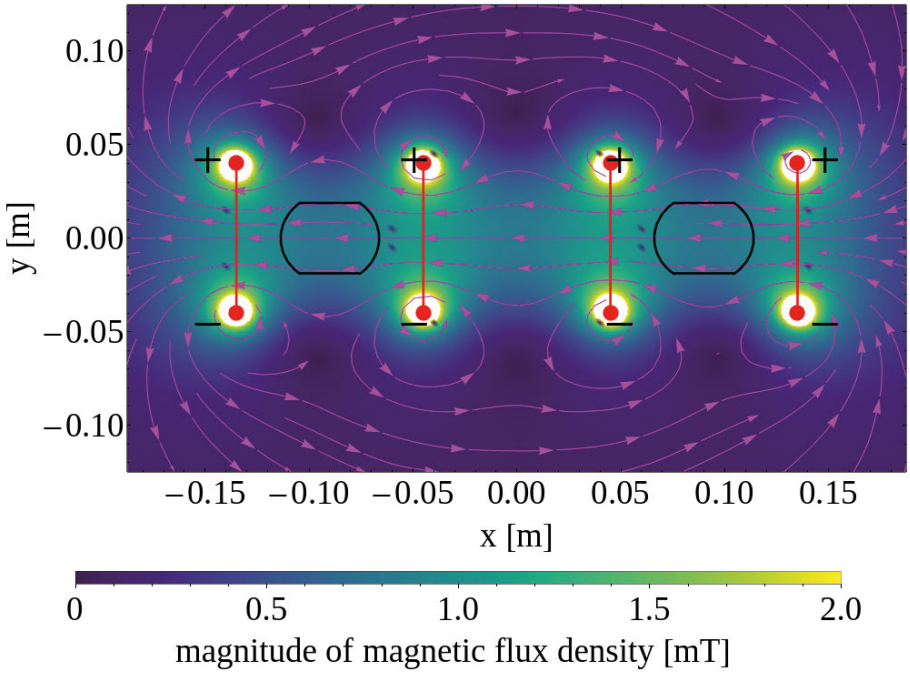

Figure 5.2. Magnetic field induced in a main dipole (double aperture) when all quench heaters fire (the nominal scenario). The black lines show the beam screen, while the red lines show which quench heater strips are connected to each other. The QH polarities are shown by + and -.

magnetic flux density, which attenuates the kick of the QHs on the first few turns. A more accurate method is consequently to use Eq. 4.2 on a turn-by-turn basis. This requires iteratively mapping the measured beam position and angle from the BPMs to the QH, and then the QH back to the BPM. The beam angle can be determined from two BPM measurements, using the following equation (results are presented in the report from the experiment: [63]):

$$x_0' = \frac{x_1 - \sqrt{\frac{\beta_1}{\beta_0}}\Big(\cos[\Delta\varphi] + \alpha_0 \sin[\Delta\varphi]\Big)x_0}{\sqrt{\beta_0\beta_1}\sin[\Delta\varphi]} \tag{5.3}$$

The calculated magnetic fields produced when all QH circuits in the most critical HL-LHC magnets fire are shown in Paper I Fig. 5. For the triplet quadrupoles, and the main dipole shown in Fig. 5.2, the field is dipolar, whereas for the separation (D1) and recombination (D2) dipoles, the field is quadrupolar. This qualitative difference arises from the polarities of the different QH strips – in half of the QH strips the current is flowing parallel to the beam, whereas in half the current flows back antiparallel to the beam. These connection schemes are important to consider, and where possible one should use the quadrupolar connection schemes as this limits the kick on the beam. For the

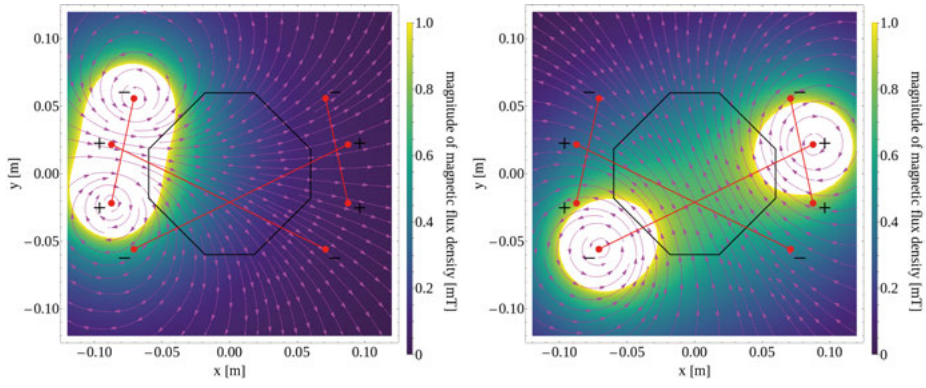

(a) **(b)**

Figure 5.3. Spurious discharge of single quench heater circuits in the D1 separation dipole. Black lines show the beam screen, while red lines show which quench heaters are connected to each other. In (a), a QH circuit located on the side fires, which provides a relatively small kick on the beam. In (b), a QH circuit connected across the magnets fires, which enhances its effect on the beam.

triplets this was not possible due to competing requirements from the magnet and circuit design.

While it is part of the design requirements that QHs and CLIQ cannot fire normally with beam in the machine, spurious discharges of single units cannot be excluded, and have been observed in the past, albeit rarely. For spurious discharges of a single QH circuit, only two strips will activate. How the strips are connected to each other is shown by the red lines in the figures. The discharges in two different circuits in D1 are compared in Fig. 5.3; in (a) a circuit confined to one side and in (b) a circuit connected across the magnet cross section. The latter connection enhances the effect on the beam since the magnetic field becomes stronger in the beam region. The ideal scenario when considering the beam impact is the one in D2 (Paper I Fig. 5). All the QH circuits are confined to one quadrant each of the magnet. While this produces a strong field at the edge of the magnet, in the beam region the effect is minimized. One of the downsides of this layout is that if one QH circuit fails, one whole quadrant of the magnet is not efficiently protected. In the D2 this is not considered a concern [64]. In the D1 layout [65], all parts of the magnets are protected at least partially, unless there is a simultaneous failure of two QH circuits.

The kicks for the most critical HL-LHC magnets are summarized in Paper I Table II. The worst cases are the horizontal kicks in the D1 dipole and the Q2 quadrupoles, reaching up to $1.38\,\sigma$ and $1.23\,\sigma$ respectively. This is within the machine protection limit set at $1.5\,\sigma$, although the oscillatory nature of the resulting orbit excursion could breach it (c.f. Sec. 4.1). Spurious

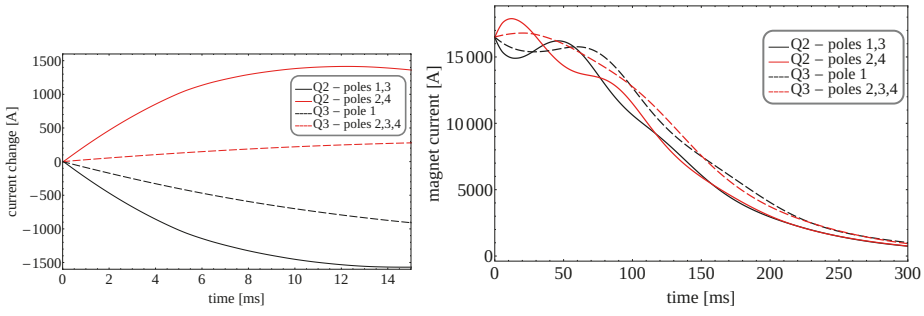

(a) **(b)**

Figure 5.4. CLIQ currents in the triplet magnets Q2 and Q3, during a spurious discharge of a single unit. Q1 is the same as Q3. (a) is a zoom showing the relative current change whereas (b) shows the decay of the nominal magnet current as well.

discharges must be detected by a separate system and interlocked, such that the beams are dumped as fast as possible.

5.1.2 Coupling Loss Induced Quench

The magnetic fields induced by a discharge of CLIQ are more complicated than the ones of the QHs, and finite-element methods are required [66–69]. The induced CLIQ currents in the three triplet magnets are shown in Fig. 5.4. Due to the change in magnet current, coupling-currents are induced in the copper matrix surrounding the superconducting wires, which heats up the whole magnet mass. This also induces a magnetic field that increases over time. As with QHs, spurious discharges cannot be excluded and the resulting magnetic field change in such a case is shown in Fig. 5.5, at a time $t = 5\,\text{ms}$ after the start of the discharge. In Q1 and Q3, the main components of the field are normal and skew dipolar. In Q2, the main component is instead skew octupolar.

The reason for this difference lies in how the CLIQ units are connected. The connection scheme for the CLIQ units is shown in Fig 5.6. This is the baseline before these studies, whereas the new baseline as of 2020 is shown in Paper I Fig. 9. The new baseline is a direct outcome of the work presented in this thesis. The three triplet quadrupole magnets, Q1, Q2 and Q3 are marked in the circuit. Their four poles are designated p1, p2, p3 and p4, and are depicted in Fig. 5.7. Each of the triplet magnets consist of two equivalent halves, that are rotated 180 degrees in relation to each other (in the horizontal plane). The halves are designated a or b, with a being the half closest to the collision point. For Q2 the halves are in separate cryostats, but not for Q1 and Q3.

The CLIQ units are marked as C in the circuit diagram. For Q2, if one CLIQ unit fires, only one half (7.15 m) is affected. In the schematic the nominal magnet current goes to the right, and it is consequently increased by the

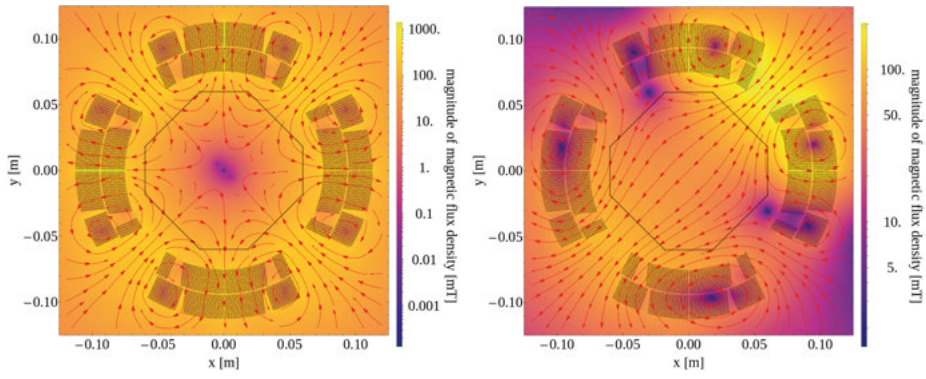

(a) **(b)**

Figure 5.5. The magnetic field induced by a CLIQ discharge in the IP1 and IP5 triplet magnets, 5 ms after firing. The black lines show the beam screen and the black dots the cable positions. (a) Q2 - skew octupolar field (b) Q1/Q3 - normal and skew dipolar fields (beam screen corresponds to Q3).

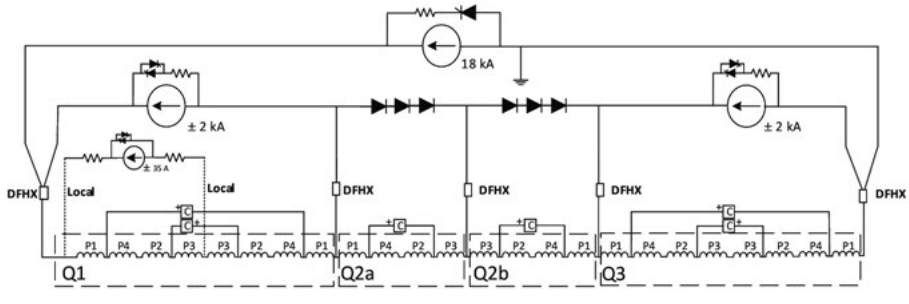

Figure 5.6. Circuit diagram of the HL-LHC triplet magnets, Q1, Q2 and Q3. The magnet poles are designated by p1 through p4, and the CLIQ units by C. For Q2, the magnet halves are separate.

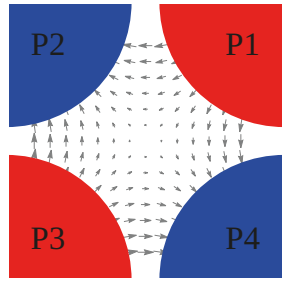

Figure 5.7. Schematic showing the pole numbering in a quadrupole magnet. The LHC center is to the right, and beam 1 goes into the paper, while beam 2 goes out of the paper. The magnet is thus horizontally focusing for beam 1 and horizontally defocusing for beam 2.

CLIQ discharge in poles p4 and p2, but reduced in poles p1 and p3. This is a *symmetric* discharge, and explains the skew octupolar magnetic field.

For Q1 and Q3, if one CLIQ unit fires, both the magnet halves (4.2 m each) are affected. In both magnet halves, for three of the poles the CLIQ current goes in one direction, and for only one pole the current goes in the other direction. This leads to an *asymmetric* discharge, and explains the dipolar magnetic fields.

A multipolar decomposition of the magnetic fields under this baseline is summarized in Paper I Table III (time $t = 3$ ms after start of discharge). The worst components for each magnet is marked in bold. For a beam with a static transverse orbit of 17 mm, the magnetic flux density integrated over the length of the magnet would then 0.11 Tm for Q2 and 0.26 Tm for Q1 and Q3.

This shows that the dipolar magnetic field components in the Q1 and Q3 make them significantly worse than the skew octupolar field component of the Q2. Furthermore, since the beam orbit is not static within the magnets, the average orbit is smaller, and consequently the integrated magnetic field of Q2 is smaller than 0.11 Tm.

After attaining the magnetic fields during the CLIQ current ramp, they were decomposed into their multipoles on a turn-by-turn basis and used in MAD-X tracking simulations. For the tracking, thin lenses were used for computational speed. The downside of using thin lens tracking in these studies is that it requires a re-matching of the magnet strengths throughout the accelerator, in order to have correct optics parameters (Twiss parameters, tunes, ...).

The output of the tracking contains the six phase space coordinates as explained in Section 2.1. These are normalized using Eq. 2.21 and the orbit excursion is calculated. The orbit excursion is the figure of merit for the final results, since orbit displacement limits are defined to the beam centroid reaching an excursion of $1.5\,\sigma$ (c.f. Sec. 3.1.2).

The results of the tracking for CLIQ in the triplet magnets are presented in Figs. 5.8, only showing the worst triplet for each type (Q1, Q2 and Q3), for the old and the new baselines in solid and dashed lines respectively. In the new baseline (see Paper I Fig. 9 for details), the CLIQ connection in Q1 and Q3 has been redesigned to be equivalent to the scheme for Q2, thus removing the dipolar fields and instead producing a skew octupolar field. Indeed the effect is significantly slower with the new baseline. In the old baseline, the $1.5\,\sigma$ limit is reached already in one turn, and the beam center reaches the physical aperture within five turns. There are no means of protecting the LHC against a failure such as this, neither using active nor passive equipment, and significant damage to machine components would be expected. With the new baseline, Q2 constitutes the worst case, but the limit is only reached in 17 turns, providing sufficient time to detect the failure and extract the beams. This requires however that a dedicated detection system for spurious CLIQ discharges is implemented.

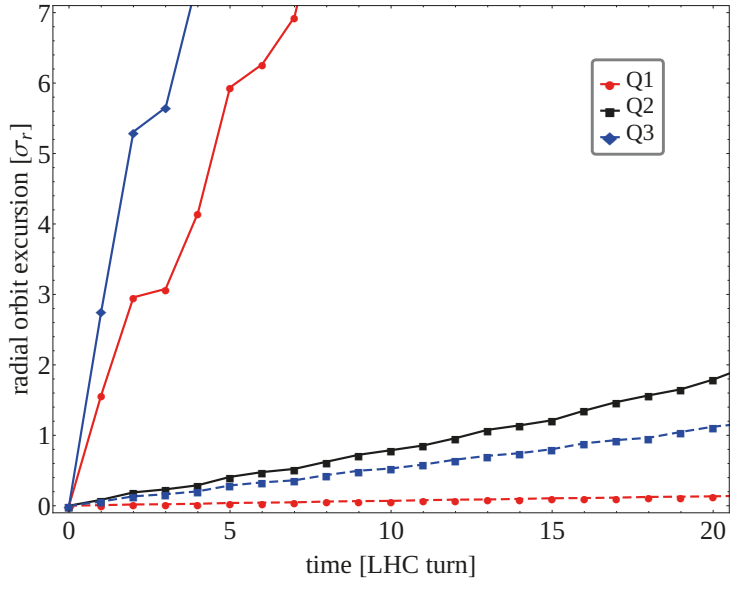

Figure 5.8. Results of a spurious CLIQ discharge in the worst of each of the Q1, Q2 and Q3 triplet magnets. Solid lines are with the previous baseline connection, while dashed lines show the proposed mitigation adopted into the new baseline.

Other than the orbit excursion, the CLIQ units have a strong effect on other beam optics as well, inducing beta beating and tune changes. As explained in Section 4.2, beta beating can change the effective collimator gap settings, by modulating the beam size throughout the machine. The primary collimator gaps and the dump absorber gaps are discussed in detail in Paper I.

As for the hierarchy between the primary and secondary betatron collimators, this is breached in some of the cases, as seen in e.g. the worst case, a magnet designated MQXFB.B2R5 (Q2 right of IP5) in Fig 5.9. On turns 9 and 10 after the CLIQ discharge, the hierarchy is breached for all the secondary collimators with the horizontal primary collimator. This means that primary beam losses would start appearing on the secondary collimators. Nevertheless, since the secondary collimators are also robust, this would mainly be a concern for the efficiency of the beam cleaning, which is not important on these time scales [70]; within 10 turns of the start of the failure the beams will be dumped by the interlock systems.

In Paper I, the effect of different beam orbits within the triplets as the CLIQ discharge occurs is also discussed. Due to the nested problem, with the CLIQ effect on the beam depending on time, on the beam orbit, the change in beam orbit, and the induced beta beating, there is no simple method of scaling the resulting orbit excursion with different initial orbits. For the paper, an iterative approach was taken instead, simulating the effect for some different initial

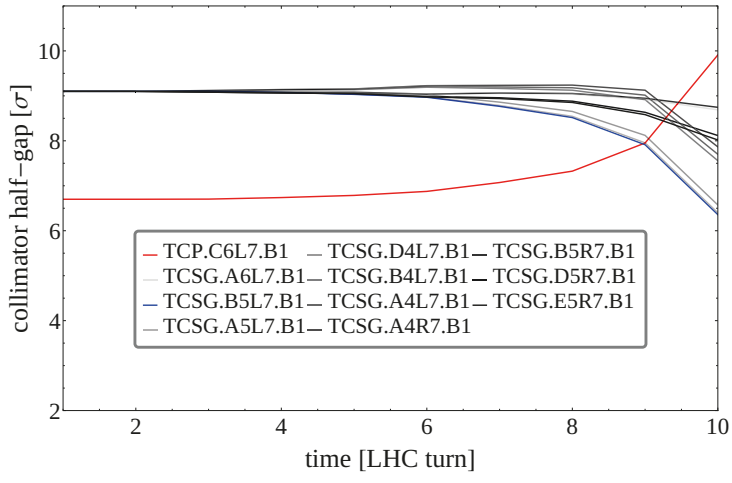

Figure 5.9. Change of the effective primary (TCP) and secondary (TCSG) collimator settings following a spurious CLIQ discharge in the worst case magnet (Q2 right of IP5).

beam orbit offsets. These are presented in Paper I Fig. 15, and show that the orbit must be kept to the design value within a 2 mm margin.

5.2 Triplet Quenches

With the majority of LHC magnets being superconducting, the risk that a magnet quenches and becomes resistive is ever-present. Once they quench, the current slowly decays on the order of a second and the magnet consequently loses its function on the beam [71]. If this occurs in a main dipole magnet, the beam will not get deflected as much as it should, giving it a horizontal orbit offset throughout the machine. If it happens in a quadrupole magnet, the focusing properties of the lattice will become incorrect. Another effect that can occur in higher-order magnets, if the nominal beam orbits are displaced in these magnets, is that a transverse kick on the beam is removed. Removal of a kick is in practice equivalent to the addition of a kick, with opposite sign.

Normally, the current decay in the magnets is slow enough that the beams are extracted by the interlock systems long before any effects become present on the beam. However, in summer of 2018, one of the Q1 triplet magnets next to IP1 (ATLAS) quenched. This quench occurred in the top half of the magnet and was symmetric around the vertical axis. Due to the symmetry, it took an unusually long time for the quench detection system to detect it. Furthermore, in this particular case the helium bath had an unusually high temperature of 2.16 K instead of the nominal 1.9 K, which caused the quench to propagate quickly. Since the beam orbits are offset from the magnetic center in the triplet magnets, a drift of the orbit for beam 1 resulted, up to a root mean squared

value of 60 μm. Beam losses were consequently induced in the collimators, triggering a beam dump.

Beam 2 was not appreciably affected at all in this event, despite sharing the same beam pipe as beam 1 in this particular magnet and also having an offset from the magnetic center. This is believed to have been caused by how the current redistributed around the resistive zone that develops due to the quench, as shown by simulations in [72].

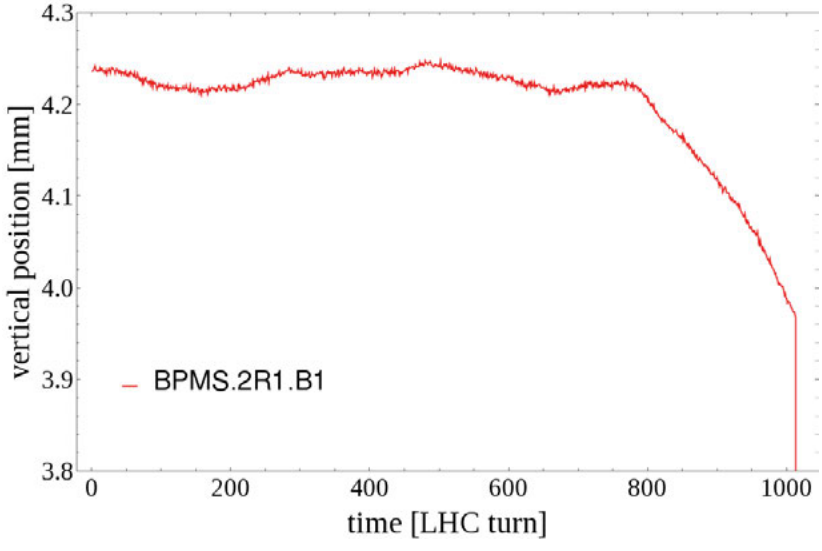

Figure 5.10. Measured orbit over time by the BPM closest to the Q1 right of IP1 that quenched. The quench started at 242 turns before the beam dump.

Figure 5.10 shows the orbit during the observed quench as measured by the BPM closest to the magnet that quenched. A shift of about 180 μm can be seen for the last 240 turns. This is a relatively slow kick and the shift follows the change in the closed orbit (c.f. Fig 4.2). The measurements of all 594 standard BPMs around the LHC were normalized by their individual beta functions and then a fit of Eq. 4.3 was done, leaving the kick $\Delta y'$ and the phase φ_0 as free parameters. The result of the fit is compared to the BPM measurements around IP1 in Fig. 5.11. A cusp can be seen at the location of the triplet magnet that quenched, which confirms the source of the kick.

The kick over time acquired from the fit is shown in Fig. 5.12. When the beams were dumped due to beam losses in the collimation region, the kick was only 0.2 μrad, or 0.7 mT, which can be compared to the nominal magnetic flux density at the beam location of over 1 T. However, due to the large vertical beta function of 3.8 km, the normalized kick reached 1 σ. While still not a critical failure in 2018 LHC, in the HL-LHC era, the beta functions will be increased to 22 km and the beam orbit to 17 mm. The 1.5 σ limit could thus be reached in only 50 turns, as shown in Paper I.

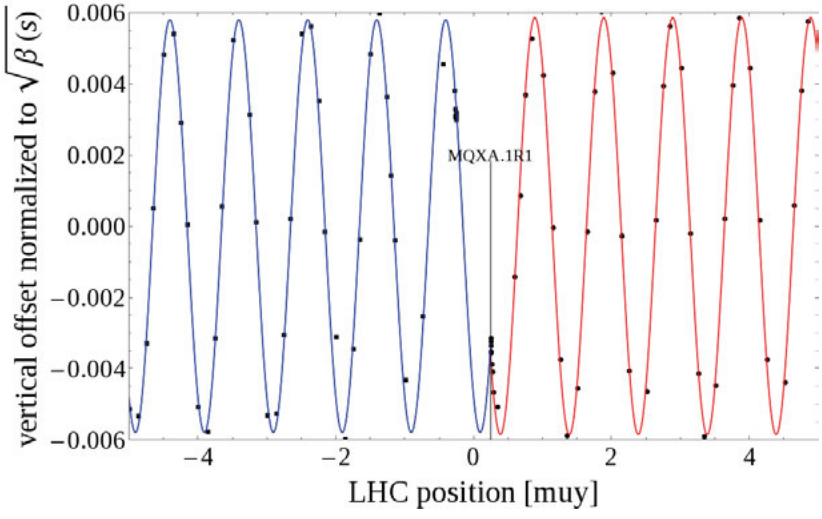

Figure 5.11. Normalized BPM measurements around IP1 compared to the fit of Eq. 4.3. *Muy* is the vertical phase advance in units of 2π. The location of MQXA.1R1, the Q1 right of IP1 that quenched, is indicated in the plot.

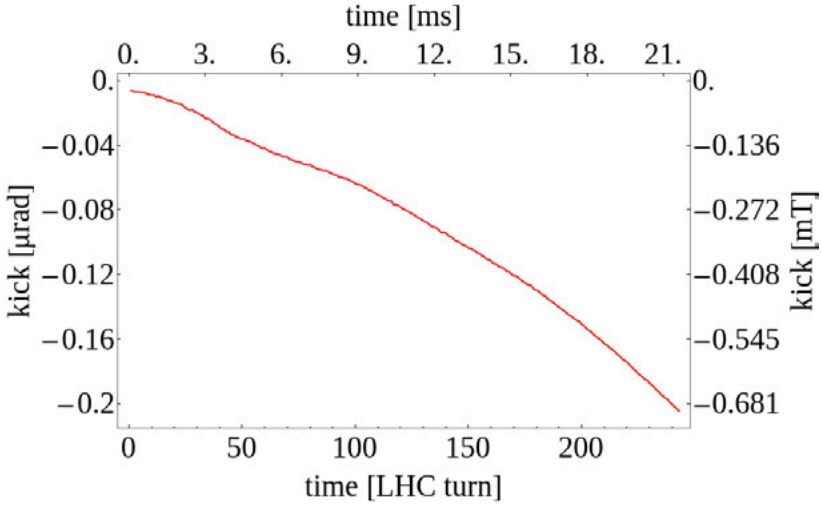

Figure 5.12. Kick over time following the quench in the Q1 right of IP1.

The detection margins, using the beam loss monitors, is adequate to protect the machine against this failure in the HL-LHC. However, this should be reiterated if there are significant changes to optics that might aggravate the failure. Whether or not the detection margins are sufficient using the hollow electron lens should be analyzed [73, 74]. If necessary, an interlock on the helium bath temperature could prevent this type of failure.

5.3 Transverse Dampers

When bunches are injected into the LHC, they generally acquire some transverse oscillations about the closed orbit in the LHC due to imperfect injections. These oscillations need be damped or they cause an effective emittance increase after filamentation. For this purpose, the LHC transverse dampers (ADT) was implemented [75]. Per plane and per beam, the ADT consists of four pairs of 1.5 m long electric plates centered around the beam with an aperture of 52 mm. They can provide small transverse kicks (up to 0.2 μrad at 6.5 TeV) to the bunches. Each individual bunch has its transverse displacements measured at two locations in IR4. This allows determining its displacement and angle following Eq. 5.3. The future angle that the bunch will have at the location of the kickers is then calculated and transmitted in time for the kickers to apply a voltage to the bunch, correcting its angle. Injection oscillations are thus damped, with a decay constant of about 50 LHC turns.

After their conception, it was realized that they have a diverse usage, and they are used throughout the whole LHC cycle to damp transverse instabilities and oscillations, as well as to clean out particles trapped in the abort and injection gaps [76].

Since the ADT can apply a voltage to individual bunches in order to damp them it can also excite bunches by reversing the sign of the applied voltage. This can be done flexibly depending on the goal. For example applying white noise voltage to a bunch will cause its emittance to grow. Applying a static voltage to selected bunches will instead give them a shifted closed orbit as if there was an extra dipole magnet for only these bunches. Coherently exciting a bunch gives it ever-increasing transverse oscillation amplitudes, such that it can be lost into the aperture. Due to its capability of exciting oscillations in the beam, it is important to ensure that it does not cause excitations by a fault, that it does not risk causing damage when excitations are manually executed, and that the interlock systems are adequate for protecting the machine in the worst case.

The ADT is configured to always provide damping to the bunches and any excitations are superposed on the damping voltage. The resulting orbit excursion over time thus takes the form:

$$\sigma(t) = \frac{k}{d}(1 - exp[-d \cdot t]) \tag{5.4}$$

where k/d is the kick strength in units of σ/kV and d the damping time in turns. The orbit excursion over time takes this form for a given constant excitation voltage. As the bunch oscillations increase, the damping voltage applied to it increases, such that an equilibrium eventually occurs between the excitation and the damping. From experiments (c.f. Paper I Fig. 21), k/d and damping constant τ were fitted to $1.274 \pm 0.004\,\sigma/\text{kV}$ and 82.8 ± 0.7 turns at

a beam energy of 6.5 TeV. At 450 GeV they were fitted to $2.379 \pm 0.008\,\sigma/\mathrm{kV}$ and 44.5 ± 0.4 turns respectively.

The maximum voltage of the ADT depends on its frequency, and consequently its resolution. For single bunch resolution, it is 1 kV, whereas for a multiple bunch mode (1 MHz corresponding to 20 bunches or more) the voltage is up to 7.5 kV. The Twiss parameters of the ADT kicker and BPMs are presented in Table 5.1.

Table 5.1. *Names of the ADT kickers and BPMs and their positions and beta functions, in LHC Run II, $\beta^* = 25\,\mathrm{cm}$ collision optics. The beta functions for the kickers are in practice the same for the different Run II and Run III optics. The position s is measured clockwise from the center of IP1.*

Element	Comment	s [m]	β_x [m]	β_y [m]
ADTKH.A5L4.B1	beam 1 hor. kicker	9972	268	227
ADTKV.A5R4.B1	beam 1 ver. kicker	10023	217	265
ADTKH.A5R4.B2	beam 2 hor. kicker	10022	260	281
ADTKV.A5L4.B2	beam 2 ver. kicker	9971	209	332
BPMCS.7L4.B1	beam 1 hor. Q7 BPM	9728		
BPMCS.9L4.B1	beam 1 hor. Q9 BPM	9648		
BPMCS.7R4.B1	beam 1 ver. Q7 BPM	10260		
BPMCS.9R4.B1	beam 1 ver. Q9 BPM	10337		
BPMCS.7R4.B2	beam 2 hor. Q7 BPM	10260		
BPMCS.9R4.B2	beam 2 hor. Q9 BPM	10337		
BPMCS.7L4.B2	beam 2 ver. Q7 BPM	9728		
BPMCS.9L4.B2	beam 2 ver. Q9 BPM	9648		

Given the maximum beta function in the kicking plane of 332 m at their location, the normalized theoretical kick as calculated from Eq. 4.1 becomes:

$$\begin{aligned} \frac{\bar{E}/c \cdot l \cdot e}{E/c}\sqrt{\frac{\beta}{\varepsilon_g}} = \frac{Ule}{Ed}\sqrt{\frac{\beta}{\varepsilon_g}} &= \frac{7.5\times10^3\cdot 6}{0.052\cdot 6.5\times10^{12}}\frac{\mathrm{eVm}}{\mathrm{eVm}}\sqrt{\frac{\beta}{\varepsilon_g}} \\ &\approx 0.13\,\mu\mathrm{rad}\sqrt{\frac{332\,\mathrm{m}}{3.609\times10^{-10}\,\mathrm{mrad}}} = 0.13\,\sigma \end{aligned} \tag{5.5}$$

where $\bar{E} = U/d$ is the approximate electric field, with voltage U and gap d, l the length of the ADT kicker plates, and E the energy of the beam. If this kick is applied statically over multiple turns, the closed orbit change for the affected bunch becomes, following Eq. 4.3, a factor of $(2\sin[\pi Q_y])^{-1} \approx 0.59$ smaller than the normalized kick, meaning $0.08\,\sigma$. Given that the beta functions in the arcs is up to about 330 m, this means that the displaced orbit is up to $\Delta y \approx 30\,\mu$m. For injection energy, the displaced orbit is up to $\Delta y \approx 380\,\mu$m in the arcs.

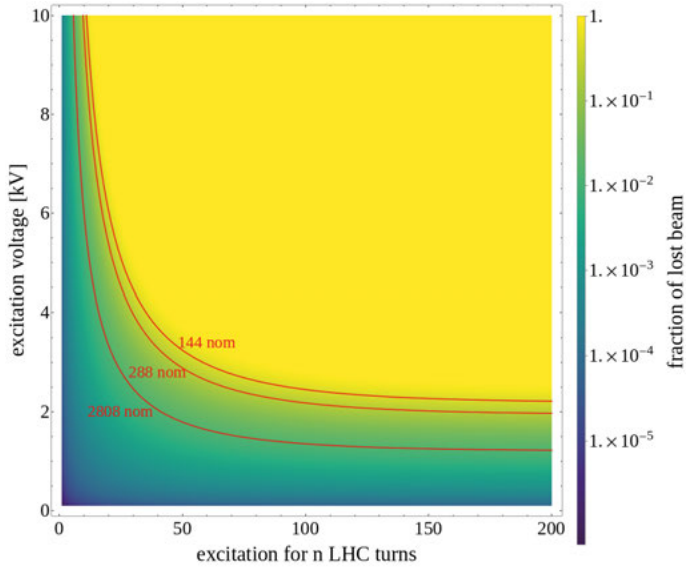

Figure 5.13. Fraction of lost beam for coherent ADT excitations at a beam energy of $\mathbf{0.45}\boldsymbol{TeV}$ in LHC Run III optics. The contour lines refer to the beam loss limit assuming a certain number of bunches with $1.8 \times 10^{11}\,\mathrm{p}^{+}$ each.

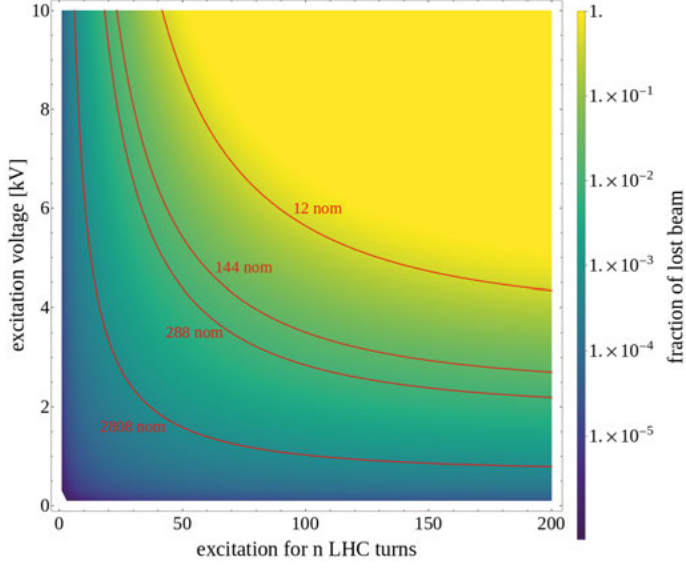

Figure 5.14. Fraction of lost beam for coherent ADT excitations at a beam energy of $\mathbf{6.5}\boldsymbol{TeV}$ in LHC Run III optics. The contour lines refer to the beam loss limit assuming a certain number of bunches with $1.8 \times 10^{11}\,\mathrm{p}^{+}$ each.

As for multi-turn, coherent, excitations, the fraction of lost beam depending on excitation voltage and number of turns is shown in Figs. 5.13 and 5.14.

These plots are for injection and top energy (6.5 TeV) during Run III, with the damping parameters as fitted to Eq. 5.4. The color density shows the fraction of lost beam and the contour lines correspond to the damage limits depending on how many nominal bunches are excited in parallel. That is, bunches with an intensity of $1.8 \times 10^{11}\,\mathrm{p}^+$.

These plots can be used as a reference for interlock settings on the ADT. A similar plot is shown in Paper I Fig. 22 for HL-LHC parameters. With the higher bunch intensity of $2.2 \times 10^{11}\,\mathrm{p}^+$ the orbit excursion threshold ($1.5\,\sigma$) is reached in twelve turns. Consequently the current protection strategy using the BLM system, as well as the new beam-current change monitor to be implemented, is sufficient even in the worst case. This is regardless of whether the excitation is due to a fault or due to manual operations.

5.4 Beam-dust interactions

Ever since high intensity beam operation started in the LHC, sporadic beam loss spikes have been observed throughout the whole accelerator, for both beams [77]. These loss spikes have caused a significant amount of beam dumps and several magnet quenches [78]. An example of a measurement of these beam losses is shown in Fig. 5.15. The beam loss spike has a total length of about a millisecond, which is typical. It has a longer rise time than fall time, which is in line with expectations from the hypothesis of their interactions. This is however not always the case in the measurements as discussed in Paper II. With increasing beam energies, the impact of these events on machine availability is expected to aggravate [77]. The prevailing hypothesis for these events is the interaction of micrometer-sized dust particles with the beam, leading to their name Unidentified Falling Objects (UFOs). Dust has been a long-time problem in electron accelerators, where the negative beam potential attracts positively charged dust, which is then trapped inside the beam as it keeps acquiring a larger positive charge [79–81].

The LHC is the first accelerator with positively charged beams to suffer from their consequences. It is believed that the dust particles fall into the beam through gravity, and possibly also electrostatic attraction due to an initial negative charge. As the dust starts interacting with the beam protons, electrons are ejected from it, leading to a positive charge build-up. This causes an electric repulsion of the dust, slowing it down and eventually ejecting it from the beam. During the interaction, there are also inelastic collisions, causing localized particle showers observed as beam losses, and also elastically scattered beam protons that end up causing beam losses in the collimation system.

Several studies were conducted by previous authors [78, 82] to understand these events better, with the hope of mitigating them. These studies showed that dust interacting with the beam be the most likely explanation for the events [82, 83]. A tool for simulating the dynamics and the resulting beam

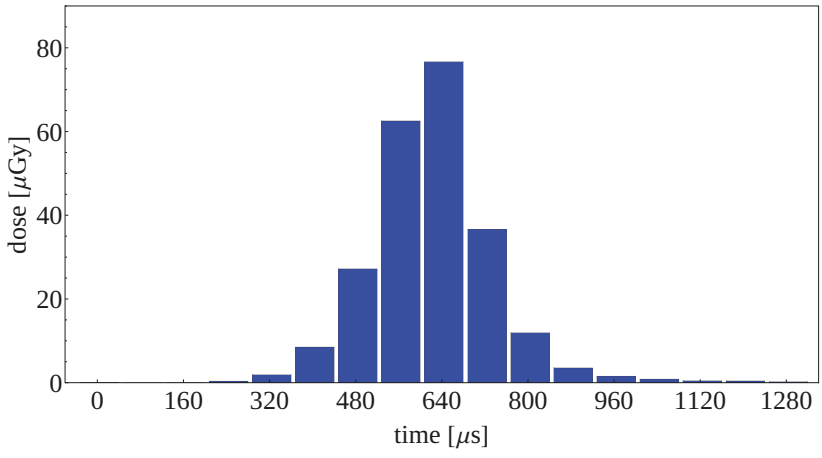

Figure 5.15. Example of an ionization chamber beam loss monitor measurement of a UFO event.

losses due to their interaction with the beam was also devised [84]. More details about these previous studies are summarized in Paper II.

One of the questions concerning this dust is whether it can have an initial negative charge or not. The presence of a negative charge plays an important role for the dynamics, and consequently the resulting beam losses, and could be key to explaining what triggers the dust to start moving towards the beam. A method for studying the dynamics of the dust particles as they interact with the beam was developed and first tested in an experiment presented in Paper IV. This method relies on having selected bunches in the beam with a larger transverse size: one group of bunches with an increased vertical size and one group with an increased horizontal size. Comparing the relative beam losses arising from these two groups of bunches with the normal, reference, bunches, allows calculating the dust particle position in relation to the transverse center of the beam.

The result was promising, giving an estimated dust particle position consistent with simulations. Nevertheless, the event was fast, and only the turn with the peak losses could be utilized for the method. Furthermore, only one event could be triggered, since this particular UFO caused a beam instability after the initial interaction, resulting in a beam dump.

Ratio of bunches method

The method for estimating the UFO position based on bunches of different sizes is explained in this subsection. In Fig 5.16(a), the proton density of two Gaussian bunches is shown, projected onto one dimension. A dust particle is located at 2σ from the beam center, producing beam losses from the two bunches that are proportional to their respective proton densities. The ratio of the two bunch profiles is plotted in Fig. 5.16(b).

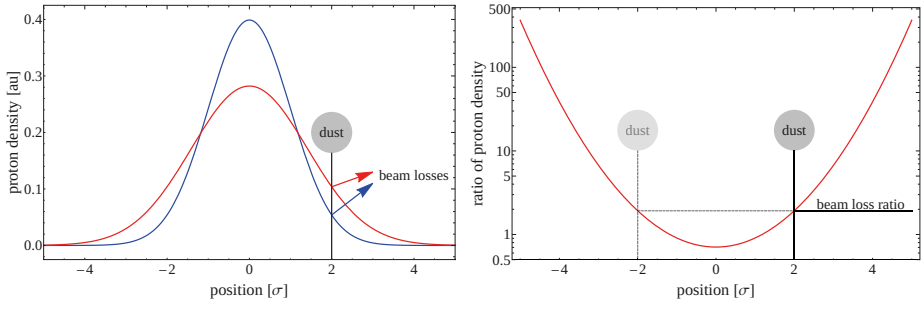

(a) **(b)**

Figure 5.16. (a) Gaussian proton density profiles, one with an emittance a factor of two larger than the other, (b) Ratio of the proton density profiles. A dust particle is located at an offset of $2\,\sigma$ from the beam center.

By looking at this ratio, one can deduce the dust particle location as shown by the lines. There is however a symmetry around zero, such that a measured beam loss ratio produces two potential dust particle locations in this one dimensional case. The two dimensional case (horizontal and vertical planes) requires at least three different bunches, producing four potential dust particle positions. This is explained in Paper II.

The measured beam losses per bunch are, under the assumption of Gaussian beams, given by

$$\text{signal} \propto \frac{N_b}{\sigma_x \sigma_y \sqrt{2\pi}} e^{-\frac{1}{2}\left(\frac{x^2}{\sigma_x^2}+\frac{y^2}{\sigma_y^2}\right)} \tag{5.6}$$

The proportionality factor is independent on which bunch the dust is interacting with. N_b is the bunch intensity, x and y the horizontal and vertical coordinates of the dust particle center in relation to the bunch center, and σ_x and σ_y the transverse bunch sizes.

Defining m_i as the measured losses normalized by bunch intensity for bunch type i, the ratio of the measurements from two bunches i and j are given by:

$$\begin{aligned} \frac{m_i}{m_j} &= \frac{\sigma_{xj}\sigma_{yj}\exp[-\frac{1}{2}(\frac{x^2}{\sigma_{xi}^2}+\frac{y^2}{\sigma_{yi}^2})]}{\sigma_{xi}\sigma_{yi}\exp[-\frac{1}{2}(\frac{x^2}{\sigma_{xj}^2}+\frac{y^2}{\sigma_{yj}^2})]} = \\ &= \frac{\sigma_{xj}\sigma_{yj}}{\sigma_{xi}\sigma_{yi}} \exp\left[\frac{1}{2}\left(x^2(s_{xj}^2-s_{xi}^2)+y^2(s_{yj}^2-s_{yi}^2)\right)\right] \end{aligned} \tag{5.7}$$

where the reciprocal of the bunch size was defined as $s_{x,y} \equiv 1/\sigma_{x,y}$. Rearranging this gives an equation describing a hyperbola or an ellipse:

$$m_{ij} \equiv 2\ln\left[\frac{m_i}{m_j}\frac{\sigma_{xi}\sigma_{yi}}{\sigma_{xj}\sigma_{yj}}\right] = x^2(s_{xj}^2-s_{xi}^2)+y^2(s_{yj}^2-s_{yi}^2) \tag{5.8}$$

where m_{ij} was defined for brevity. This equation can be solved uniquely with a four-fold symmetry by adding the ratio between a third bunch and one of the first two bunches. This leads to the matrix equation:

$$AX = M \tag{5.9}$$

$$\begin{pmatrix} (s_{x2}^2 - s_{x1}^2) & (s_{y2}^2 - s_{y1}^2) \\ (s_{x2}^2 - s_{x3}^2) & (s_{y2}^2 - s_{y3}^2) \end{pmatrix} \begin{pmatrix} x^2 \\ y^2 \end{pmatrix} = \begin{pmatrix} m_{12} \\ m_{32} \end{pmatrix} \tag{5.10}$$

By defining

$$A^{-1} \equiv \begin{pmatrix} a & b \\ c & d \end{pmatrix} \tag{5.11}$$

the solution can be expressed as

$$X = \begin{pmatrix} x^2 \\ y^2 \end{pmatrix} = \begin{pmatrix} a & b \\ c & d \end{pmatrix} \begin{pmatrix} m_{12} \\ m_{32} \end{pmatrix} = \begin{pmatrix} am_{12} + bm_{32} \\ cm_{12} + dm_{32} \end{pmatrix} \tag{5.12}$$

$$\leftrightarrow \begin{cases} x = \pm\sqrt{am_{12} + bm_{32}} \\ y = \pm\sqrt{cm_{12} + dm_{32}} \end{cases} \tag{5.13}$$

Error estimate

Error propagation gives the covariance matrix for the estimated x and y coordinates from the covariance matrix of m_{ij}, that is $C_X = JC_MJ^T$, where J is the Jacobian for the transformation from the measured m_{ij} to the x and y estimates. C are the covariance matrices for the different parameters.

By restricting the solutions to the first quadrant, and setting the equation for x as f_1 and the equation for y as f_2, the Jacobian then becomes:

$$J = \begin{pmatrix} \frac{\partial f_1}{\partial m_{12}} & \frac{\partial f_1}{\partial m_{32}} \\ \frac{\partial f_2}{\partial m_{12}} & \frac{\partial f_2}{\partial m_{32}} \end{pmatrix} = \frac{1}{2} \begin{pmatrix} \frac{a}{\sqrt{am_{12}+bm_{32}}} & \frac{b}{\sqrt{am_{12}+bm_{32}}} \\ \frac{c}{\sqrt{cm_{12}+dm_{32}}} & \frac{d}{\sqrt{cm_{12}+dm_{32}}} \end{pmatrix} \tag{5.14}$$

The sample standard deviation $\hat{\sigma}$ of the measurements can be estimated from bunches with similar bunch parameters, meaning that they should provide the same amount of beam losses given a set dust particle position. This should be the same for the blown-up bunches. The covariance matrix for the measured parameters, considering the three types of bunches (reference, vertically and horizontally blown-up) is then given by:

$$\begin{pmatrix} \sigma_1^2 & 0 & 0 \\ 0 & \sigma_2^2 & 0 \\ 0 & 0 & \sigma_3^2 \end{pmatrix} = \hat{\sigma}^2 \begin{pmatrix} \frac{1}{N_1} & 0 & 0 \\ 0 & \frac{1}{N_2} & 0 \\ 0 & 0 & \frac{1}{N_3} \end{pmatrix} \tag{5.15}$$

where N_i are the number of bunches of each type. The Jacobian for transforming the measured values m_1, m_2 and m_3 to m_{ij} is given by:

$$J = 2\begin{pmatrix} \frac{1}{m_1} & -\frac{1}{m_2} & 0 \\ 0 & 0 & 0 \\ 0 & -\frac{1}{m_2} & \frac{1}{m_3} \end{pmatrix} \tag{5.16}$$

The covariance matrix for m_{ij} then transforms to the following:

$$C_M = 4\begin{pmatrix} \frac{\sigma_1^2}{m_1^2} + \frac{\sigma_2^2}{m_2^2} & 0 & \frac{\sigma_2^2}{m_2^2} \\ 0 & 0 & 0 \\ \frac{\sigma_2^2}{m_2^2} & 0 & \frac{\sigma_2^2}{m_2^2} + \frac{\sigma_3^2}{m_3^2} \end{pmatrix} = \tag{5.17}$$

$$C_M = 4\hat{\sigma}^2\begin{pmatrix} \frac{1}{N_1 m_1^2} + \frac{1}{N_2 m_2^2} & 0 & \frac{1}{N_2 m_2^2} \\ 0 & 0 & 0 \\ \frac{1}{N_2 m_2^2} & 0 & \frac{1}{N_2 m_2^2} + \frac{1}{N_3 m_3^2} \end{pmatrix} \tag{5.18}$$

The zero values in this matrix correspond to the parameter m_{22} and can thus be removed from the matrix, giving the required 2×2 matrix for calculating the final covariance matrix C_X. This is used to construct confidence ellipses for the estimated dust particle positions when applying the method on the measurements.

Displaced Bunches

An alternative method to the blown-up bunches, is to displace the orbit of selected bunches by giving them a recurring dipolar kick every turn, as explained in Eq. 5.5. At top energy, this leads to a maximum orbit offset of $30\,\mu$m in the arcs. Taking the ratio of two Gaussian bunch profiles of the same width, where one is displaced by this amount horizontally, we get:

$$\begin{aligned} \frac{m_i}{m_j} &= \frac{\sigma_{xj}\sigma_{yj}\exp[-\frac{1}{2}(\frac{x_i^2}{\sigma_{xi}^2} + \frac{y_i^2}{\sigma_{yi}^2})]}{\sigma_{xi}\sigma_{yi}\exp[-\frac{1}{2}(\frac{x_j^2}{\sigma_{xj}^2} + \frac{y_j^2}{\sigma_{yj}^2})]} = \exp\left[\frac{1}{2}\left(x_j^2 s_{xj}^2 - x_i s_{xi}^2 + y_j^2 s_{yj}^2 - y_i s_{yi}^2\right)\right] = \\ &= \exp\left[\frac{s_x^2}{2}\left((\Delta x + x_i)^2 - x_i^2\right)\right] = \exp\left[\frac{s_x^2}{2}\left(\Delta x^2 + 2\Delta x x_i\right)\right] = e^{\frac{s_x^2 \Delta x^2}{2}} e^{s_x^2 \Delta x x_i} \end{aligned} \tag{5.19}$$

where Δx is the horizontal difference between the center of the two bunches, and $x_{i,j}$ and $y_{i,j}$ are the dust particle positions in relation to the center of the two bunches. The other parameters are the same as defined above for the ratio of bunches method. This gives a simple relation between measured ratio and horizontal dust particle position, with x_i being the only unknown. A plot of this is shown in Fig. 5.17. It can be seen that even with a small bunch-by-bunch offset of $30\,\mu$m, there is a significant difference between the expected

measured values, with increased losses from the displaced bunch of 11%, 23% and 37% for a dust particle at 1, 2 and 3 σ respectively. This method also removes the symmetry of the method using blown-up bunches, which would provide important information for the dust particle dynamics.

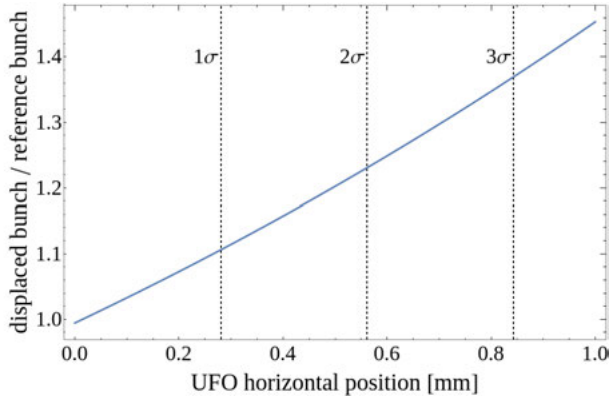

Figure 5.17. Ratio of the bunch distribution for a bunch displaced 30 μm with that of a reference bunch with zero displacement. Lines corresponding to 1, 2 and 3 horizontal σ of the reference bunch are shown.

Results

Given the successful experiment in Paper IV, a follow-up was devised and is detailed in Paper II. Until recently, only UFOs that caused beam dumps could trigger the fast diamond beam loss monitors (dBLM) required for measuring the bunch-by-bunch losses (c.f. Sec. 3.1.2). With an upgraded acquisition system in 2018, it became possible to trigger on UFOs that did not cause beam dumps. In the experiment, one bunch had its vertical size increased and one bunch its horizontal size, in both of the two LHC beams. Diamond BLMs installed in the betatron collimation region (IR7) were then used to measure the elastically scattered beam losses produced by UFOs at any location in the LHC.

During the experiment with blown-up bunches, a total of 12 UFOs were recorded. There were another 16 events recorded during the validation period prior to having blown-up bunches, and another 6 events recorded during a heavy ion run that was conducted after this experiment, where blown-up bunches were not available. Out of the events recorded with proton beams, 17 were during ramp, and 16 were also detected by a separate UFO detection system which looks at the ionization chamber beam loss monitor (ICBLM) signals only. During the period with blown-up bunches, the ICBLM based system detected a total of 33 events, mostly at top energy. A detailed list of the events with blown-up bunches is shown in Table 5.2.

For the events with blown-up bunches, the signal was unfortunately too low for doing a meaningful analysis in most events. For every bunch-dust particle

Table 5.2. *List of dBLM recorded UFOs with blown-up bunches. The maximum bunch signal is the peak height in bits output by the analog to digital converter.*

Event timestamp [CET]	Beam	Beam energy [TeV]	Max bunch signal [au]
2018-09-30 224752	b2	6.5	2100
2018-10-03 121604	b1	6.5	490
2018-10-03 152726	b2	2.9	210
2018-10-07 012459	b2	3.4	400
2018-10-09 174201	b1	1.1	170
2018-10-16 095144	b1	4.5	460
2018-10-16 141328	b1	2.1	210
2018-10-17 235320	b2	1.6	140
2018-10-17 235320	b2	1.6	220
2018-10-19 143039	b1	3.4	250
2018-10-20 094316	b1	2.3	1400
2018-10-26 231623	b1	6.5	340

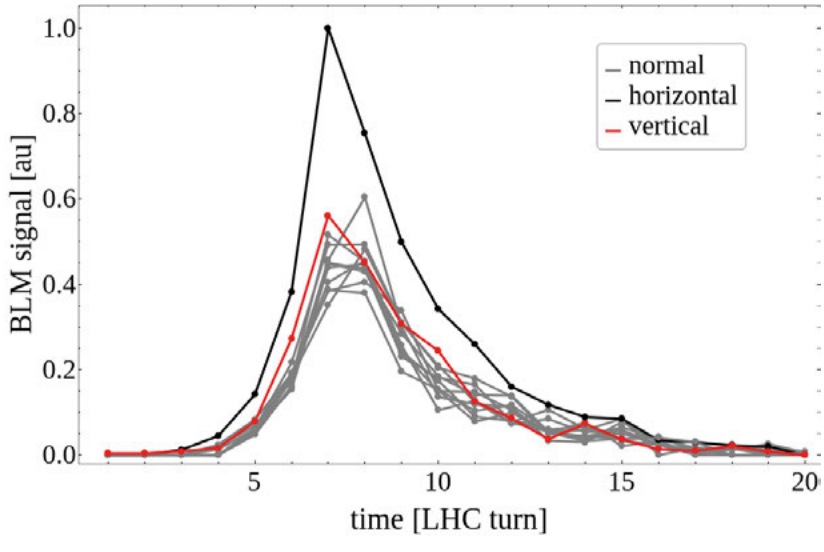

Figure 5.18. Bunch-by-bunch losses per turn for the 12 bunch train. Horizontally blown-up bunch is shown in black, vertically blown-up bunch in red and reference bunches in gray.

crossing, a small number of protons are elastically scattered with sufficient amplitudes to hit the primary collimators, producing the showers measured by the dBLMs. However, the magnitude of the showers depends on the beam energy. This is also dependent on the betatron phase advance, such that a disadvantageous phase advance can cause the scattered protons to miss the collimators. Measurement challenges aside, it could also be that some events

simply did not produce a lot of beam losses, e.g. due to a shallow penetration depth into the beam and dust with a small mass.

In the end, two events had a maximum signal an order of magnitude larger than the others. The first of these, top in the list in Table 5.2, is explained in detail in Paper II and is shown in Fig. 5.18. It was possible to reconstruct the dust particle position over the four turns leading up to, and including, the peak losses. The result of this is shown in Fig 5.19. Monte-Carlo simulations, using a UFO dynamics simulation tool [84], were then conducted to find the best matching initial dust particle conditions. These simulations used the inelastically scattered beam losses measured locally by the ICBLMs as reference, in order to find the conditions that best could reproduce the observed beam losses. The trajectory of the best fit is also shown in Fig. 5.19. There is a good agreement on the three turns with the highest losses, although the angle of approach is more vertical in the simulated event. Nevertheless, this is the first direct validation of the dynamics simulation tool. Furthermore these measurements and simulations give a strong indication that dust particles can have an initial negative charge.

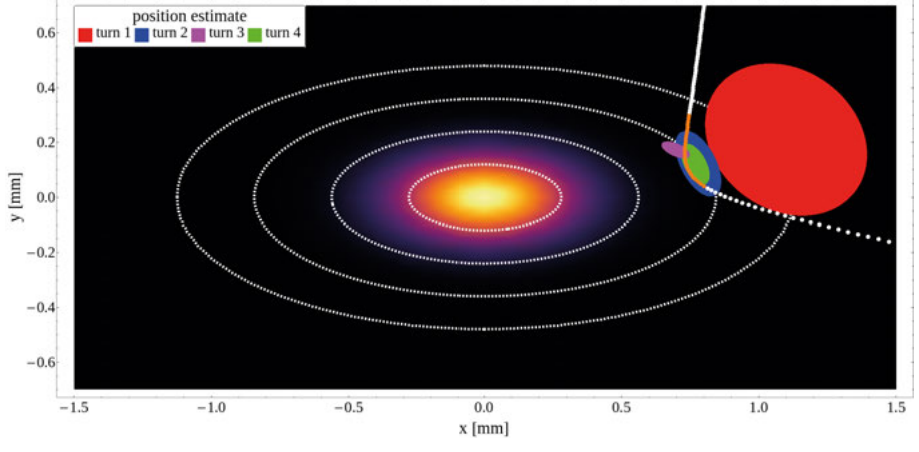

Figure 5.19. Result of the dust particle position estimate for the four turns leading up to the peak in Fig. 5.18. White dots show the simulated trajectory, with orange dots corresponding to the four turns leading up to the simulated peak losses.

The other event with a good signal, second to last on the list in Table 5.2, is shown in Fig. 5.20. This event was unfortunately too short to conduct a dynamics study, only having a useful signal on one turn. Nevertheless, it is interesting since it is the only event where the reference bunches showed a significantly larger signal than the blown-up bunches. This indicates that the dust particle entered deeply into the beam, to a radial position of about $1\,\sigma$. From the dynamics simulation tool, it is known that the more deeply the dust particle enters the beam, the more quickly it is ejected. This is due to the significantly higher proton density giving a correspondingly faster ionization

rate of the dust particle. This kind of event is not possible for dust simply falling into the beam, as it would be moving too slowly. This is consistent with the measurement, since it only shows signal on one turn, meaning that the dust particle quickly entered and quickly exited the beam.

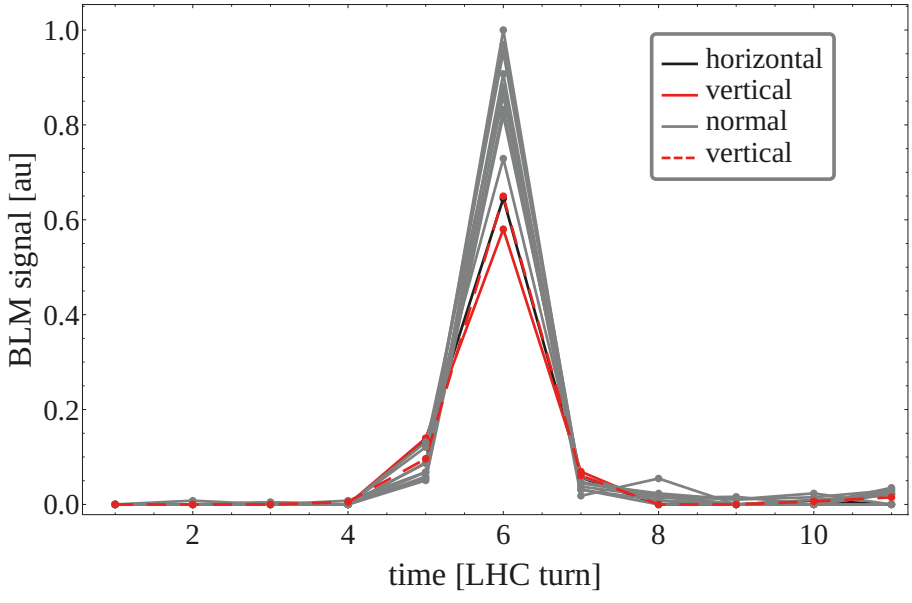

Figure 5.20. Time profile of an event with increased signal in the reference bunches (gray). Vertically blown-up bunches are shown in red whereas black shows the horizontally blown-up bunch. The dashed red line is a bunch that unintentionally had a larger vertical emittance, in-between nominal and that of the blown-up bunch.

In summary, the understanding of UFO dynamics has been significantly improved, through validation of the simulation tool with direct measurements, and the conclusion that dust particles can be negatively charged. A novel method for studying the dynamics of dust particles, indirectly through beam losses, was also devised. Only the method using blown-up bunches was applied in experiments, but the method using displaced bunches is strongly recommended for testing in the future.

5.5 Beam-beam kick

Since the beams share a common beam pipe around the collision points, IPs 1, 2, 5 and 8, they exert a force on each other as explained in Section 2.8.2.

The part with a common beam pipe goes between the left and right D1 separation dipoles, for a total length of 150.5 m for IP1 and IP5, and 118.7 m for IP2 and IP8. With a bunch spacing of 25 ns, each bunch sees a bunch from the opposing beam every 12.5 ns, receiving a kick. This means that there are

up to 41 beam-beam kicks in IP1 and IP5, and up to 33 kicks in IP2 and IP8. Due to the filling pattern of the beams, consisting of bunch trains separated by gaps of various lengths, the bunches of one beam will see a different number of bunches of the other beam, at different locations around the IP. The maximum effect is seen on bunches in the middle of the trains, since they see a maximum number of opposing bunches both on their approach and their departure from the IP. For bunches in the beginning of a train, they will not see any opposing bunches on their approach, consequently having roughly half the total number of beam-beam kicks. The same applies for bunches at the end of a train, but they only see opposing bunches on their approach to the IP.

During normal operation, the beam-beam kick is corrected by corrector magnets. However, if one beam is suddenly removed, due to a beam dump, the remaining beam will suddenly stop seeing the beam-beam kick from the beam that was dumped. In effect the beam-beam kick is then overcorrected by the magnets, leading to an orbit excursion. The abort gaps of beam 1 and beam 2 are synchronized in IP1 (ATLAS) and IP5 (CMS), meaning that it is not possible to extract both beams at exactly the same time in IR6. Furthermore, due to the design of the LHC interlock and beam dumping system, there can be a delay of up to three turns between dumping the beams. As mentioned in Section 3.1.2, both beams have beam permits propagated by optical loops around the accelerator, that when cut trigger the beam extraction. Some systems only cut the permit for one of the beams and then rely on a *beam linking* in IR6 to also dump the other beam, however this introduces a delay. A loss of the beam-beam kick is thus seen for every beam dump on at least one turn, and for some dumps it is visible for up to three turns.

A schematic of the beam dumping process is shown in Fig. 5.21, for beam 1 (left) and beam 2 (right). As beam 1 starts being dumped, the last quarter of beam 2 will be the first to experience a loss of the beam-beam kick, in IP8. Next, the first quarter of beam 2 will experience a loss from IP1, as well as IP8. Then, the middle half of the beam will experience a loss of the beam-beam kick from IP2 and onward. The last quarter of beam 2 will not experience a loss of the beam-beam kick in IP5 until the second time it passes the IP.

When dumping beam 2 first, the order of losing the beam-beam kicks for beam 1 is different. The first quarter of beam 1 will first experience a loss of the kick in IP5, it will then see the kick in IP8 and lose it again in IP1 and onward. The middle half also experiences a loss first in IP5, where after it will not see the kick anymore. The last quarter of beam 1 experiences a loss of the kick from IP2 and onward.

The three different parts of the beams are designated by the magenta squares in the schematic. Now, it is also important where one is observing the beam. For example, since the last quarter of beam 1 sees a loss of the kick from IP2 and onward, when it reaches the betatron collimation region in IR7, it will only have seen a loss of the kick in IP2 and IP5. Then it continues on towards IP8 and IP1, where it also experiences the loss. Consequently, only the second

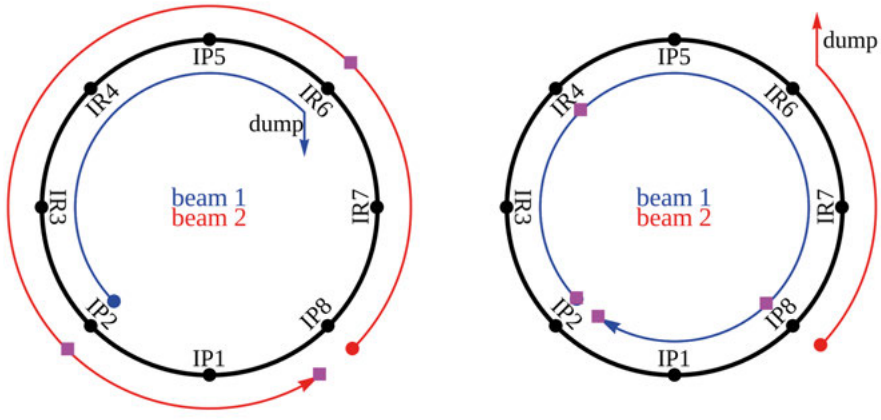

(a) **(b)**

Figure 5.21. Schematic top view of the dump of the two beams; for simplicity the beam crossings are not shown. (a) shows the order in which beam 2 sees a loss of the beam-beam kick in the different IPs as beam 1 is being dumped, while (b) shows the other case with beam 2 being dumped. The magenta squares show how the beams are partitioned when it comes to the order that they experience a loss of the beam-beam kick.

time that it passes IR7 will it have seen the loss from all IPs, whereas if one is instead observing it between IP1 and IP2, a loss of the kick in all four IPs would be seen already on the first turn. This is summarized for the two beams in Table 5.3. There are two observation points of interest, IR4, which is where the BPMs used for this analysis are located, and IR7, where the main beam losses occur.

The magnitude of this orbit excursion is simulated using the *beambeam module* in MAD-X. Using correctly matched thin optics for beams 1 and 2, markers are placed at the location of every beam-beam kick in the beam that is to be removed. Twiss calculations provide the beam parameters at each of these markers. The transverse positions and beta functions are extracted. Next, *beambeam* kicks are installed at the same locations for the beam that remains, using the Twiss parameters of the beam that is removed. Lastly tracking is done on a reference particle.

For the tracking, two methods are possible. One is to adiabatically ramp up the beam-beam kick strength, while also correcting the optics such that the beam remains on the correct closed orbit with the correct Twiss parameters, and then suddenly setting the beam-beam kick to zero. This is however complicated since the optics cannot be matched while tracking. A simpler, and equivalent, method is to start the tracking with the beam-beam kick set to zero, and then suddenly putting it to its full value with a negative sign. The latter was used for the simulations presented here.

Table 5.3. *The sequence of the loss of the beam-beam kick in the IPs is indicated for the three turns, for the three different parts of beam 1 (b1) and beam 2 (b2). For an explanation of the beam parts, please see Fig. 5.21.*

B1	Observed in IR7			Observed in IR4		
part	Turn 1	Turn 2	Turn 3	Turn 1	Turn 2	Turn 3
1	IP5	IP1 IP2	IP8		IP5 IP1 IP2	IP8
2	IP5	IP8 IP1 IP2			IP5 IP8 IP1 IP2	
3	IP2 IP5	IP8 IP1		IP2	IP5 IP8 IP1	
B2						
1		IP1 IP8	IP5 IP2		IP1 IP8 IP5	IP2
2		IP2 IP1 IP8	IP5		IP2 IP1 IP8 IP5	
3	IP8	IP2 IP1	IP5	IP8	IP2 IP1 IP5	

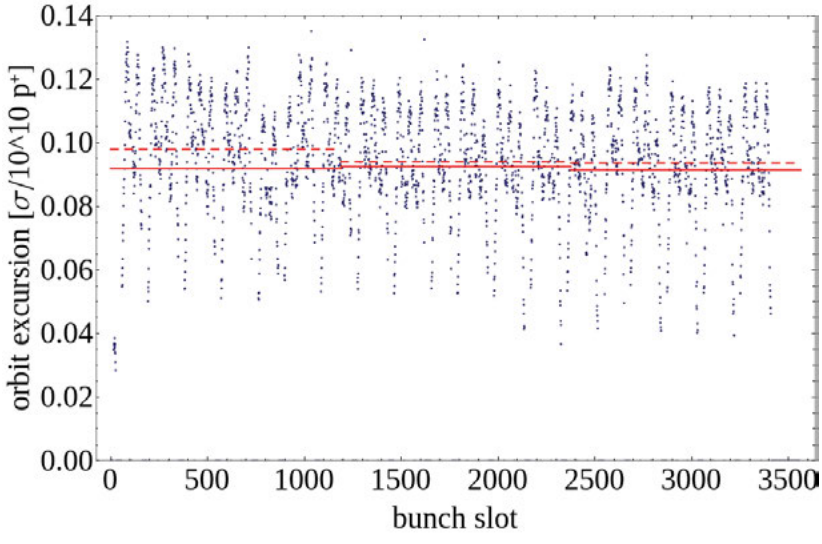

Figure 5.22. Comparison between the measurements and the simulations of the beam-beam kick in beam 1. The blue dots show the orbit excursion normalized to bunch intensity for the individual bunches in the filling pattern. The dashed red lines show the average over the three beam parts. The solid red lines show the estimates from the simulations of the three beam parts. .

This method was validated against measurements, as shown in Fig. 5.22 for beam 1 and Paper I Fig. 18 for beam 2. These consist of 5 measurements on beam 1, and 14 measurements on beam 2. They show the orbit excursion per bunch, normalized to the bunch intensity. The red lines correspond to the simulated beam-beam kicks, using average bunch intensities and emittances of the full beam. The simulations assume that the bunch encounters opposing bunches at all potential locations. This explains why some of the bunches in

the measurements fall below these lines, going down to a value about half of these. All in all, the agreement is good when considering average beam losses over the full beam (dashed red lines).

The relevant beam parameters considered for future LHC operations are presented in Paper I Table IV. The bunch intensity will be increased, to 1.8×10^{11} p^+ in Run III and 2.2×10^{11} p^+ in HL-LHC. Since the kick is proportional to the bunch intensity, this plays a significant role. In HL-LHC, the β^* will also decrease, which increases the beta function around the collision point. Increased beta functions implies both a stronger beam-beam kick due to the increased bunch size (see Eq. 2.26) and an increased normalized kick (see Eq. 4.1). On the other hand, the crossing angles will also be increased in HL-LHC, which puts the beams further apart and limits the beam-beam kick. For more details on beam optics in the different LHC eras, the reader is referred to Table 3.2.

The leveling also plays a role, since the less squeezed optics at the start of collisions (*stable beams*, SB) limit the beam-beam kick. This is considered for Run III, with start and end of SB, as well as a realistic mix of them both. For HL-LHC, the machine is designed to be able to run with the fully squeezed optics with the maximum bunch intensity, and the machine must consequently be able to run safely under these conditions.

Table 5.4. *Results of the beam-beam kick simulations per IP for Run III and HL-LHC, shown as the* ***radial orbit excursion in units of beam*** σ. *The values are the orbit excursion that the remaining beam would see on the first turn if it looses the beam-beam kick of one individual IP.*

Optics	IP1 (hor.)	IP2 (ver.)	IP5 (ver.)	IP8 (hor.)
Run III				
Start of SB	0.79	0.18	0.43	0.23
End of SB	0.65	0.08	0.52	0.15
HL-LHC				
Round	0.86	0.09	0.86	0.58
Flat	0.72	0.09	0.72	0.57

The expected beam-beam kick per IP is shown in Table 5.4 for the considered cases. Both beams see the same normalized kick in each IP. The kick is strongest in IPs 1 and 5, which is due to them having more squeezed optics than IPs 2 and 8. HL-LHC is worse than Run III as expected from the increased bunch intensity. The larger crossing angle however counteracts this increase to a certain extent. In HL-LHC, the optics in IPs 1 and 5 are equivalent, but in opposite planes (IP1 has horizontal crossing while IP5 has vertical crossing).

The results of the complete simulations, for both beams and different beam optics in Run III and HL-LHC, are summarized in Paper I Table VI. For nom-

inal optics in Run III, the defined beam loss limit of 1 MJ deposited into the collimation system, is just reached on the third turn for beam 2, when first dumping beam 1. This is acceptable as long as there are no other large orbit excursions already in place on the beam, that adds up with the beam-beam kick. In HL-LHC however, the limit is breached on the second turn for beam 1, when dumping beam 2 first. It is consequently required that the machine protection system does not allow more than a single turn of delay between dumping the two beams. This can be achieved by linking the beam permits of both beams in the hardware of the BIS for high intensity operation.

5.6 Beam-beam compensating wires

The long-range beam-beam compensating wires (BBCW) are sets of straight current-carrying wires installed parallel to the beams. Their purpose is to imitate the long-range beam-beam kicks up to second order and compensate for the adverse effects this has on the beam quality, in particular emittance growth [85]. In the LHC Run III, they are 1 m long, installed inside tertiary collimators around IPs 1 and 5, at a minimum distance to the beam of 9.9 mm [86, 87]. A pair of wires is installed at each location and different magnetic fields can be produced depending on the relative polarity of the wires.

In the HL-LHC, where they are considered for installation, they will be 3 m long, installed as separate elements in the shadow of the tertiary collimators, next to the IP1 and IP5 Q4 quadrupoles (distance to beam $> 10.5\,\sigma$) [88–90]. Only one wire per location is envisioned, meaning that a dipolar field will be the main component at the beam location.

A short-circuit bypassing the wire would be the fastest source of a failure involving them. This is however not expected to be of concern since it can be avoided by an appropriate design. What remains are failures involving the power converter. If it trips, the current approximately decays exponentially as shown in Fig. 5.23. The magnetic field in the beam region decays proportionally to the current and the effect it has on the beam is consequently removed, effectively leading to a kick on the beam.

In the LHC Run III, the pairs of wires are powered with opposite polarities, producing magnetic field components of even order (quadrupolar, octupolar, ...). As the power decays, beta beating is induced. If the beam is not centered in the collimator jaws, a kick is also imparted on the beam. In HL-LHC, a kick is the main effect but there is also some beating due to higher-order magnetic field components.

There is less mass in between the BBCW and the beam, than between the quench heaters (from 5.1.1) and the beam, and the change in current is about three orders of magnitude slower. The magnetic fields are thus calculated in the same way as for the quench heaters, by the Biot-Savart law Eq 5.1.

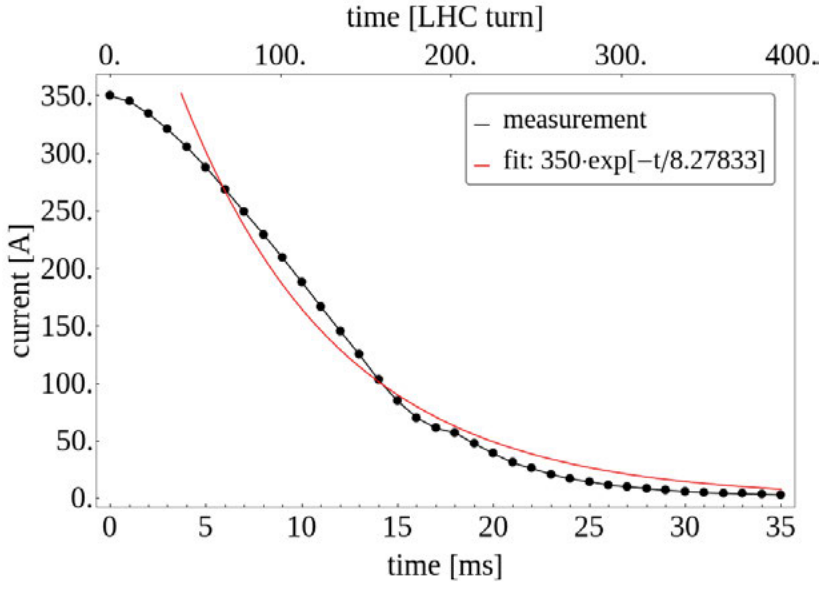

Figure 5.23. Measured current decay in the power converter to be used for the Run III BBCW.

The kick is then calculated by Eq. 4.1, while the beta beating is calculated from the quadrupolar gradient using Eq. 4.4. The tune change is calculated from:

$$\Delta Q_{x,y} = \frac{\beta_{x,y}}{4\pi f} \tag{5.20}$$

where f is the focal length of the produced quadrupolar field.

The beta beating around the machine for beam 1 in Run III is shown in Fig 5.24. It reaches almost 8% in horizontal beating, and is similar for the other wire pairs, as well as for beam 2. In HL-LHC, the beating will be reduced to a maximum of 2% vertically, since there will only be one wire per location. In HL-LHC, there is however a kick on the beam, up to almost $1\,\sigma$ as shown in Paper I Fig. 20. In Run III, kicks are only possible if the beam for some reason is not centered in the collimator, but even then it is limited to a maximum of $0.4\,\sigma$ given realistic assumptions for the initial orbit offset.

While the BBCW do not constitute a critical source of failures in the LHC, it is important to not run the machine with the beta beating or the orbit excursion that they can induce and they should be interlocked against powering failures. The expected interlock for this kind of less critical system, part of the WIC (c.f. Section 3.1.2) reacts in 1.2 ms, which is sufficiently fast for dumping the beams.

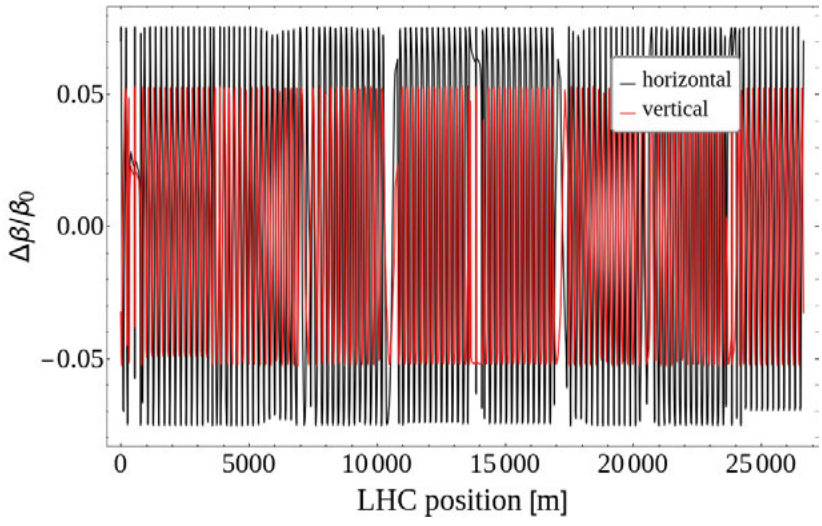

Figure 5.24. Beta beating induced by wires with fully depleted currents in the tertiary collimator TCTPH.4L1.B1, Run III.

5.7 Crab Cavities

The crab cavities were introduced in Section 3.2. Their purpose is to apply a longitudinally modulated transverse kick to the bunches around the collision points in the ATLAS and CMS experiments (see Eq. 3.2). This improves the overlap in the collision point, that is otherwise reduced by the crossing angle, and improves the luminosity.

There are a few different types of failures that can occur in the crab cavities, e.g. as observed in the KEKb electron-positron machine cavities [91], namely:

Power failure/voltage drop: if the voltage of one or several cavities fails, the crabbing might not be compensated properly by the cavities on the other side of the IP. This leads to crabbed beams circulating the machine, including at the aperture bottlenecks in the collimation region. This could lead to beam losses and aggravate other failure scenarios.

Phase jumps: if the phase of one or several cavities changes to a new equilibrium value, the crabbing would similarly not be uncrabbed properly, leading to crabbed beam in the collimation region. Since the zero-crossing of the phase would no longer be at the bunch center, there would also be some kick to the center part of the bunch, which is the most intense part. This would be more critical than the voltage drop.

Phase slips: if the phase changes continuously over several turns, not only would the crabbing not be compensated, but there could also be a build-up of betatron oscillations. In particular, if the phase slip per turn resonates with the betatron tune, the bunch would be coherently excited leading to it quickly hitting the aperture.

Cavity quench: since the cavities are superconducting, they can quench. This leads to both a voltage drop and a phase slip, and the consequences would be a combination of the individual failure types.

In 2018, the first ever crab cavity tests with hadron beams were performed. These utilized a set of two prototype double quarter wave [92] cavities installed in the SPS.

A simulated example of a phase slip in the SPS, where the phase change per turn resonates with the betatron tune, is shown in Fig. 5.25. The reference particle, black, quickly increases in oscillation amplitude, whereas the colored lines, corresponding to particles offset by $\pm 2\,\sigma$ in the longitudinal plane have different tunes and consequently do not keep resonant with the excitation for more than a few turns. In the HL-LHC, due to the fast interlocking of the cavities, the interest lies mainly on the first ten turns. There the majority of the particles in the bunch behave similarly to each-other.

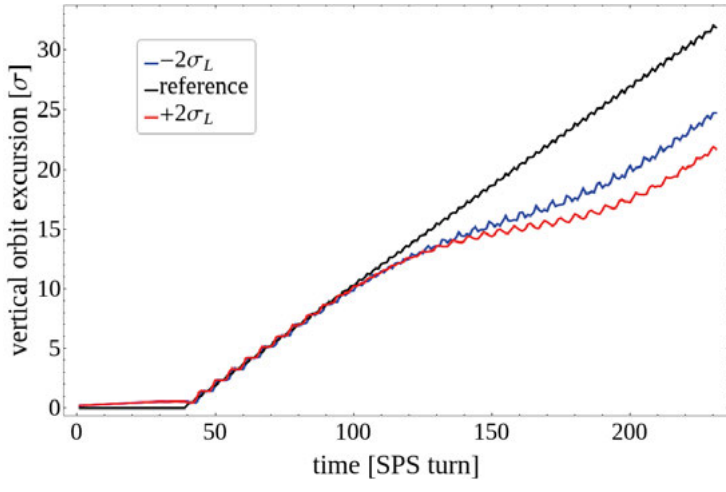

Figure 5.25. Simulated coherent excitation of the beam due to a phase slip resonating with the tune in the SPS. One SPS turn is about $23\,\mu$s.The black line corresponds to the reference particle, whereas the colored lines correspond to particles that are offset $\pm 2\,\sigma$ in the longitudinal plane.

The cavities are limited in how much they can change their phase per turn, depending on the input power and the voltage, according to the following equation [93]:

$$\max\left[\frac{d\varphi(t)}{dt}\right] = \frac{\omega}{2Q_L}\sqrt{\frac{4(R/Q_\perp)Q_L P_{max}}{V_0^2} - 1} \tag{5.21}$$

where $Q_L = 3\times 10^5$, $R/Q_\perp = 500\,\Omega$, $P_{max} = 100\,\text{kW}$, V_0 is the applied voltage and $f = 400\,\text{MHz}$. Due to this, some voltages are inherently safer than

others, as shown for simulations in the SPS in Fig. 5.26. The black line corresponds to the reference particle, whereas the colored lines correspond to particles that are offset by $\pm 2\,\sigma$ in the longitudinal plane, and as in Fig. 5.25 these particles have different tunes. What is shown is the maximum orbit excursion that the particles acquire within 100 SPS turns (one SPS turn is $0.23\,\mu$s) following the start of the failure, given a maximum phase slip per turn for different cavity voltages following Eq. 5.21. Lower voltages are critical, since the phase change per turn can be large enough to resonate with the betatron tune, whereas for large cavity voltages, a large orbit excursion can be reached without resonance.

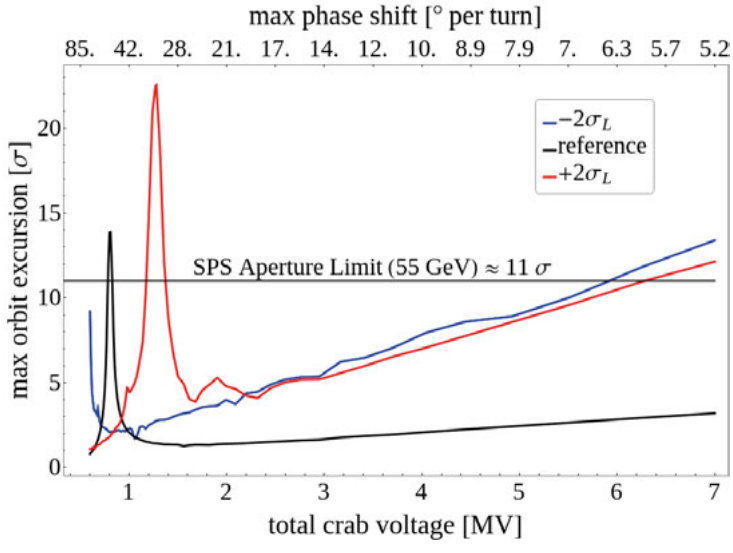

Figure 5.26. Simulated effect on the beam in the SPS following a maximum phase slip per turn at different cavity voltages. The black line corresponds to the reference particle, whereas the colored lines correspond to particles that are offset $\pm 2\,\sigma$ in the longitudinal plane.

One of the purposes of the prototype tests in the SPS was to analyze the predicted failure modes, their effect on the beam, and how to design the interlock systems for the cavities. The machine protection related conclusions from the prototype tests are summarized in Paper III.

No cavity failures occurred with beam in the machine. However, in the SPS there is a relatively large beam revolution frequency change as the beams are ramped from injection energy, 26 GeV, to the top energy of 270 GeV in these experiments. This corresponds to an RF frequency change of 120 kHz. The crab cavities are designed for the LHC, where the frequency swing is less than 1 kHz, and were consequently not capable of staying synchronized with the beam during ramp. This leads to an effective phase slip of the voltage exerted on the bunches in the beam, which quickly excited the beam into the

physical aperture at different points in the ramp where resonance occurred. An example of the measured vs simulated orbit excursions under these conditions is shown in Fig. 5.27, showing a good agreement. This provides confidence in simulations for HL-LHC. The bottom plot shows the drop in beam intensity and the recorded beam losses during the same time.

Aside from validating the simulations for HL-LHC, one of the outcomes of these tests is that fast hardware interlocks of the cavities are necessary in the future prototype tests with the RF dipole cavities, if they are to be used with high intensity beams. These interlocks should ensure that phase differences between the cavity RF and the main beam RF remains below 15 deg and that the cavity voltage remains below 50 kV during beam energy ramp.

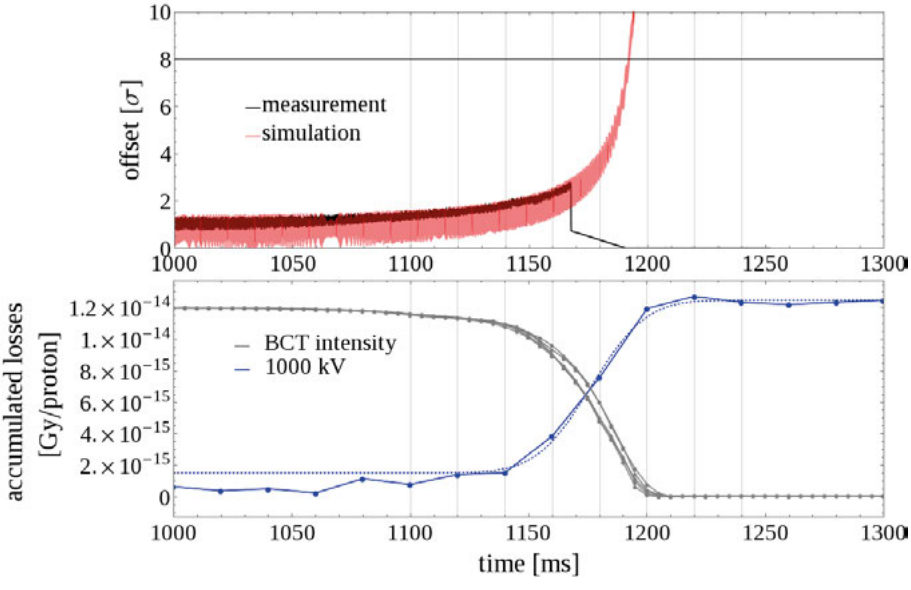

Figure 5.27. Simulated versus measured orbit excursion during a beam loss event at beam energy ramp, caused by the effective phase slip between beam revolution frequency and cavity frequency. The bottom plot shows the accumulated beam loss measurements in blue and in gray the beam intensity measurements.

The crab cavity names in the optics are summarized in Table 5.5. In the sequence they are installed as *tkicker* elements, which are normal kickers. These are useful for e.g. matching the crab cavity voltages on both sides of the IP such that the crabbing is properly compensated. Since the beta functions are different, the voltages of the cavities should be different for optimal compensation. In MAD-X there is also a *crabcavity* element, which is useful for simulating the longitudinally varying kick over the bunch. Phase, frequency and voltage can be changed for these elements during tracking. This is how the simulations in the SPS and those for HL-LHC presented in Paper V were done (see Section 5.8).

Table 5.5. *Names of the beam 1 crab cavities and their positions and beta functions (HLLHCV1.4 optics). The positions and values for beam 2 crab cavities are similar, and the final "B1" in the name is changed to "B2".*

Element	Comment	s [m]	β_x [m]	β_y [m]
ACFCA.BL1.B1	beam 1 IP1 crab cavity	26499.2	3642	3785
ACFCA.AL1.B1	beam 1 IP1 crab cavity	26500.2	3682	3904
ACFCA.AR1.B1	beam 1 IP1 crab cavity	154.8	4300	3880
ACFCA.BR1.B1	beam 1 IP1 crab cavity	155.9	4176	3838
ACFCA.BL5.B1	beam 1 IP5 crab cavity	6504.9	3643	3789
ACFCA.AL5.B1	beam 1 IP5 crab cavity	6505.9	3684	3907
ACFCA.AR5.B1	beam 1 IP5 crab cavity	6819.4	4300	3878
ACFCA.BR5.B1	beam 1 IP5 crab cavity	6820.4	4176	3836

5.8 Combined failures

Until now, different failure scenarios have been addressed on a case-by-case basis. However, one of the questions is whether these failures can occur in parallel to each other. For this to happen with any non-negligible probability, there must be a common source of or a causal link between the failures. The circuits for quench heaters and CLIQ units are all individual, and the capacitor banks for HL-LHC magnet protection devices placed in radiation shielded areas. The probability that two of these fire spuriously in parallel can thus be excluded. When a magnet quenches, it can influence the beam, and the quench protection system is also triggered. For the LHC main dipole magnets, it has happened that the quench heaters have been triggered by the quench detection system while there is still beam in the machine [94]. However, as seen in the triplet quench, for any significant kicks induced on the beam, where a combination of the quench induced orbit excursion and that of the quench protection system would be critical, the effect on the beam is faster than the reaction of the quench detection system which has a 10 ms evaluation time [95]. This means that the beams are dumped by the beam loss monitoring system before the quench protection activates.

Any kind of orbit excursions causing beam losses can lead to quenches in the magnets, which could then potentially add up with the orbit excursion already present. However, even for the worst quenches in the triplet magnets, there are a few tens of turns before the quench-induced orbit excursions start becoming significant. Furthermore, there are beam loss monitors all around the ring, with individual dump thresholds set to protect the magnets. If there are beam losses intense enough to cause magnet quenches, the beam loss monitors would likely be activated to dump the beams, before the quench itself could affect the beam.

There is however one combined failure that happens for every dump, and that is with a loss of the beam-beam kick. For every failure causing beam

losses, the beams are dumped, and since the beams cannot be dumped simultaneously, there is always at least one turn where the beam-beam kick adds up with the failure that initiated the dump. This was the scope of the study in Paper V, where a combination of crab cavity failures with the beam-beam kick was analyzed.

In this paper, two types of crab cavity failures were considered, voltage drops and phase slips. Power failures lead to exponential voltage decays with a time constant of $\tau = Q_L/(\pi f) \approx 400\,\mu$s [93], whereas the maximum rate of phase shift can be determined from Eq. 5.21 to be 28.6 deg per turn (88.9 μs). The prototype cavity interlock (see Paper IV) was capable of detecting the anomalous cavity parameters in 10 μs, although this is expected to be up to 15 μs in the HL-LHC [96]. It was thus assumed that one beam is dumped within one turn of the start of the failure, and that the remaining beam sees a combined failure for another two turns.

The resulting displacement in the primary collimators for crab cavity failures and the loss of the beam-beam kick were then simulated separately in MAD-X. For the crab cavity failures, 13 particles evenly distributed longitudinally along the bunch were tracked, while only the reference particle was considered for the beam-beam kick tracking. Since the displacements are small, on the order of 1 σ, they can be added linearly. A double Gaussian distribution (superposition of two Gaussian distributions, one for the core and one wider distribution representing the halo, c.f. Paper V) was then considered in the transverse plane, which was integrated from the collimator cut for the 13 individual particles that were tracked. Their individual contributions to the total beam losses were weighted by a longitudinal Gaussian with an RMS width of 9 cm.

It was found that, for these short time scales, the loss of the beam-beam kick is the main source of beam losses for voltage failures. On the second turn, the orbit excursion threshold (1.5 σ) was breached for all the beam 1 cases, but neither of the beam 2 cases. For phase slips, the losses were significantly aggravated, with a crab cavity failure in IP5 of beam 1 leading to a loss of 0.17% of the full beam. The orbit excursion threshold is defined by that which gives a beam loss of 1 MJ, or 0.14% of the full HL-LHC beam. For these simulations, as a conservative assumption, the crab cavity failure was added at the end of each turn and considered equally for all parts of the beam. The small breach of the threshold is consequently deemed to be manageable as long as it is ensured that there is maximum of one turn delay between dumping the two beams. This reiterates the conclusion from the beam-beam kick studies. One should also be aware that the phase advance between the crab cavities and the primary collimators plays a significant role for the short-term losses. Neither of the cases breached the threshold for beam 2, which is due to small phase advances. If the optics are changed, such that the phase advances approach 90 deg, these simulations need be reiterated. A fast interlock in the low-level RF controlling the cavities is required and it should simultaneously trigger a

dump of both beams. This is already in line with the conclusion from the beam-beam kick studies.

5.9 Discussion

Common for all failures that perturb the beam orbit, aside from the beam-beam compensating wires and the beam-beam kick, is that their impact on the beam is proportional to $\sqrt{\beta/\varepsilon_g}$. The beam-beam compensating wires are automatically set at a further distance from the beam if the beta function is increased, such that their effect remains constant. The beam-beam kick does not depend on the beta function at first order. The energy also plays a role, in that the kicks are inversely proportional to it, for all cases. For failures causing an orbit excursion, a maximum limit is defined to $1.5\,\sigma$. This is conservative, in the sense that all particles outside the collimator cuts are not immediately lost. The betatron motion spreads the losses over more than three turns. Furthermore, depending on the phase advance between the source of the failure and the collimators, a certain portion of the orbit excursion can be in the form of an angular offset rather than a displacement at the collimators, leading to less beam losses. Whether the kick is on a single turn, and how fast it is applied, also affects this dynamic behavior. This was taken into account for all simulated failure cases. The phase advance to the collimators was taken into account for beta beating results as well as the combined crab cavity and beam-beam kick loss estimates, but was not considered in general since the phase advance is not fixed. Consequently it is more robust to base the protection on the maximum orbit excursion.

These methods have allowed determining the criticality for the different failures, such that proper interlocking or other types of mitigation strategies can be ensured. Depending on the goals of the failure study, one could consider using more precise particle tracking methods that enable collimator scattering, such as SixTrack [97]. This could provide precise loss maps throughout the accelerator, but is not necessary for determining the criticality. E.g. for the old baseline CLIQ, it is clear that an orbit excursion of over $3\,\sigma$ in one turn is not acceptable. For slower cases such as the triplet quenches, it is also apparent that the margins are sufficiently large for the BLMs to provide the necessary interlocks. Where it could be useful with more precise simulations are the borderline cases that have been identified using the methods in this thesis. Whenever possible, such cases ought to be mitigated, but it is not always possible to provide further mitigations, such as for the quench heaters in D1 and Q2. In these magnets, a phase advance constraint to the primary collimators could be applied to slow the onset of beam losses further if deemed necessary.

The failures are summarized here, with a focus on the HL-LHC era:

Quench heaters can, for spurious discharges of single QH circuits, give a kick of up to $1.38\,\sigma$ within one turn in the separation dipole magnet (D1). The resulting orbit excursion could breach the threshold. Due to the oscillatory nature of this kick, the beam losses are spread out over a few turns. The required dedicated detection system for spurious discharges can consequently dump the beams before damage ensues. They cause beta beating of less than 1%. Their kicks scale with QH current, QH position, connection scheme and the beam orbit.

Coupling-loss induced quench fired spuriously causes an orbit excursion of up to $0.8\,\sigma$ in ten turns, and the limit is reached in 17 turns. They also cause considerable beta beating of up 50% within 10 turns. They require interlocking by a dedicated detection of spurious discharges, which is expected to react within $500\,\mu$s [98]. Their effect on the beam scales with the CLIQ current and the beam orbit.

Triplet quenches can kick the beam and cause beta beating due to the decrease in magnet current. The kicks develop relatively slowly and can reach $0.5\,\sigma$ in 60 turns, or the orbit excursion threshold in 80 turns. They are interlocked by the quench detection system, but this is likely too slow to react, and instead beam loss monitors would trigger the dump. Their impact on the beam scales with the beam orbit and the magnet current drop.

Transverse dampers (ADT) can cause kicks of $0.13\,\sigma$. In the HL-LHC coherent excitations can reach the orbit excursion threshold in 12 turns. Their settings are protected through software and they are interlocked by the beam loss monitors, which can react in one turn at the fastest, with two more turns necessary for the dump. Their kick scales with applied voltage and is attenuated by the single bunch mode and damping strength.

Unidentified falling objects cause sudden beam loss spikes generally reaching their peak losses in between one and ten turns. Magnet quenches can occur within a few turns and they can not be interlocked without drastic effects on machine availability due to increasing number of beam dumps. Their impact on the machine scales non-linearly with energy, such that increased energy means larger probability of beam dump and magnet quench.

Beam-beam kick leads to a radial kick of up to $1.6\,\sigma$ on the beam that remains when the other one is dumped first. The averaged orbit excursion over the beam breaches the $1.5\,\sigma$ threshold on the second turn and adds up on top of any other orbit excursion e.g. due to failures already present in the beam. The delay between dumping the two beams must consequently be limited to a maximum of one turn. The kick increases with bunch intensity while it decreases with an increased crossing angle.

Beam-beam compensating wires produce mainly a dipolar field at the beam location, which when removed e.g. due to a powering failure kicks the beam. Albeit slower than the other failures presented here, they still constitute a fast failure, with an orbit excursion of up to $0.1\,\sigma$ after ten turns or $1\,\sigma$ after approximately 40 ms. They produce small beta beating of up to 2%. Their powering circuit requires interlocking, which can react in 1.2 ms. Their impact on the beam is proportional to their current and length.

Crab cavities provide kicks of up to $1.8\,\sigma$ and with phase slips their kicks on the beam core can add up over several turns to cause critical losses. Critical losses can be expected in 5 turns. They are required to be interlocked by the low-level RF, expected to have a reaction time of $15\,\mu$s. Their kick on the beam is proportional to cavity voltage, but an increased voltage limits the maximum possible phase change per turn, which can limit the beam orbit excursion.

6. Conclusions

Since their conception in the beginning of the 20th century, particle accelerators have played a key role in the scientific development both inside and outside of physics. Furthermore, both the accelerators themselves and the technologies developed while building them have found usage in the general society. For fundamental physics research, there has been a continuous tendency towards constructing larger machines with higher energy beams. This implies that the amount of energy stored in the beams becomes increasingly more difficult to handle. The Large Hadron Collider (LHC) stands at the forefront, with an unprecedented stored beam energy of 362 MJ, in each of the two beams, which will be increased to 678 MJ with its upgrade to the High Luminosity LHC (HL-LHC). This energy corresponds to that which is released by 162 kg of TNT explosive, squeezed into a needle-thin beam less than a millimeter in width. If erroneously deflected, it can drill a hole of several meters in solid copper, and only a small fraction of this energy is capable of damaging sensitive components, such as the experiment detectors, the superconducting magnets and other accelerator equipment. With the LHC, the field of Machine Protection has emerged as a vital part of accelerator design, where failures that risk damaging the machine are studied and mitigated with active and passive machine protection systems. Passive protection consists of an extensive collimation and beam loss absorption system. Active protection detects abnormal conditions, e.g. beam losses, and act to safely remove the energy stored in the magnet circuits, and the beams by extracting them onto a robust beam dump.

Within the scope of this thesis, a broad range of fast failures were studied, with a focus on the High Luminosity era of the LHC. A number of critical failures were found, and mitigation or interlock strategies were proposed where deemed necessary. Prior to this thesis, the impact of superconducting magnet failures or their protection devices on the beam had not been considered on this level. However, it has been found that they can cause critical beam losses on ultra fast timescales, requiring dedicated interlocking and mitigation strategies. In particular failures involving crab cavities and parts of the magnet protection are among the most severe in the HL-LHC. The latter consists of quench heaters (QH) and coupling-loss induced quench (CLIQ). It is required for HL-LHC that they by design cannot fire with beam in the machine. Spurious discharges of single units can however not be excluded. For CLIQ, the beam would see an orbit excursion of over $3\,\sigma$ in just a single LHC turn, and the beam core would reach the physical aperture in just four turns. There would be no means of protecting the machine against this kind of sudden beam

loss. Instead, a change of the circuit scheme was proposed, significantly mitigating this failure scenario. This change has been adopted into the HL-LHC baseline.

For QHs, focus lied on changing the connection schemes where possible to less critical ones, meaning schemes where the dipolar fields in the beam region are minimized, which was done for the D1. In the final focusing triplet quadrupoles this was however not possible. For spurious discharges in the Q2 and D1 magnets in particular, the kick breaches the defined orbit excursion threshold, implying that beam losses above the allowed threshold could be expected. Since the losses are spread over a few turns due to the betatron motion, this is manageable as long as the failure is detected and the beams extracted with minimum delay. Consequently, both QHs and CLIQ are required to be interlocked by dedicated detection of spurious discharges, mitigating the failure.

The crab cavities are another potential source of fast failures and critical beam losses can occur in as little as five turns for phase slips. These will be interlocked with a reaction time of up to $15\,\mu$s. The beams are then dumped within three turns, giving sufficient margin. The RF dipole prototype cavity tests in the SPS during Run III also need to implement fast hardware interlocks, ensuring phase differences between the cavity RF and the main beam RF below 15 deg. During energy ramp, a cavity voltage below 50 kV should also be ensured. These tests will allow verifying that the reaction time of the crab cavity interlock is sufficiently fast for the HL-LHC.

The beam-beam kick will increase significantly in future LHC operations. If one beam remains after the other beam is dumped the perturbation of the remaining beam due to a loss of the beam-beam kick can breach the orbit excursion threshold already on the second turn. It is consequently required that both beams are dumped with a maximum of a single LHC turn of delay between each other. The combination of a loss of the beam-beam kick with another failure is however ever-present. Phase slip failures in the crab cavities are among the fastest failures, where the orbit excursion could go significantly beyond the $1.5\,\sigma$ limit. The crab cavity failures themselves will be mitigated through dedicated, fast, interlocking. The combination with the beam-beam kick reinforces the conclusion that it is necessary to limit the delay between dumping both the beams to a single turn.

For the other failure scenarios, interlock strategies based on equipment settings and on the beam loss monitoring systems are deemed sufficient for safe operation.

In summary, the methods used in this thesis have allowed the study of a wide range of different failure scenarios, for vastly different types of beam optics and configurations. The most critical failures have been addressed and mitigations proposed, whereas the current interlock strategies have been determined to be adequate for other cases.

Sammanfattning på svenska

Avhandlingens titel på svenska: *Kritikalitet hos snabba felscenarion i High Luminosity Large Hadron Collider*. Forskningen omfattar både experimentellt och teoretiskt arbete inom acceleratorfysik.

Introduktion

I början av 1900-talet utförde Geiger och Marsden ett experiment, där de lät alfapartiklar från radioaktiva preparat träffa en tunn guldfolie. När alfapartiklarna träffar folien sprids de i olika vinklar, och utifrån distributionen av dessa vinklar kunde Rutherford komma fram till att atomer består av en liten massiv kärna med elektroner runt omkring som utformar atomens volym. För att förklara hur ett sådant system kunde vara stabilt utvecklades kvantmekaniken, ur vilken bland annat våg-partikeldualiteten formaliserades. Dvs, att ett objekt har såväl partikel- som vågegenskaper. Hur små objekt som kan studeras med tex alfapartiklarna i experimentet ovan, beror på partikelns våglängd, som i sin tur beror på partikelns rörelsemängd, eller kinetiska energi. Ju snabbare en partikel rör sig, desto mindre är dess våglängd och desto mindre objekt kan den studera.

Problemet med radioaktiva källor är att partiklarna från dem inte är kontrollerade och att de har en låg energi. För att på ett mer kontrollerbart sätt kunna studera materiens uppbyggnad utvecklades därmed partikelacceleratorn. Partikelacceleratorer är maskiner vars funktion är att accelerera laddade partiklar (främst protoner och elektroner) till väldigt höga energier.

Partiklarna används sedan bland annat till att studera material, samt att låta två motriktade strålar av partiklar att kollidera med varandra. Vid dessa kollisioner skapas det en kaskad av nya partiklar som sprider ut sig kring kollisionspunkten. Runt dessa kollisionspunkter bygger man partikeldetektorer, som i detalj kan mäta de partiklar som produceras, vilken energi de har, vilka banor de rör sig i, vilken elektrisk laddning de har, osv. Utifrån detta kan man sedan validera eller avfärda de teoretiska modeller som ämnar förklara hur universum fungerar, i synnerhet den så kallade Standardmodellen inom partikelfysiken. Standardmodellen utvecklades under andra halvan av 1900-talet och förklarar vilka olika elementarpartiklar som existerar, hur de interagerar med varandra, samt hur tre av de fyra kända krafterna inom naturen fungerar, elektromagnetismen, den starka kärnkraften och den svaga kärnkraften. Gravitationen är den fjärde kraft som inte omfattas av denna modell.

Modellen har korrekt lyckats förutspå förekomsten av flera partiklar, som sedermera har upptäckts. Senast var den så kallade Higgsbosonen, som upptäcktes vid Large Hadron Collider (LHC) 2012. Bosoner är en typ av partiklar

som förklarar hur de andra elementarpartiklarna interagerar med, eller växelverkar med, varandra. Till exempel fungerar elektromagnetismen genom att virtuella fotoner växelverkar mellan två laddade partiklar, som sedan tex kan attrahera varandra. Higgsbosonen gör att elementarpartiklarna, förutom den masslösa fotonen, innehar massa. Upptäckten var således monumental för att förklara hur vår omvärld fungerar.

Det finns fortfarande ett flertal stora, fundamentala, problem i naturen som inte kan förklaras av Standardmodellen. Ett av dessa är materia-antimateria-asymmetrin, dvs observationen att det i det observerbara universum nästan bara finns materia. De flesta processer som skapar partiklar är symmetriska på så sätt att de skapar både en partikel och en antipartikel och det kräves modeller bortom Standardmodellen för att förklara denna diskrepans.

Partikelacceleratorer

En partikelaccelerator består av några grundläggande komponenter, magneter och radiofrekvens- (RF)-kaviteter. Magneterna kan klassificeras beroende på hur många poler de har; dipolmagneter har två poler med ett gap emellan. I dem produceras ett homogent, oftast vertikalt riktat, magnetfält. Detta fält böjer laddade partiklars banor i det horisontella planet, och kan därmed få strålen att åka runt i en ring. Kvadrupolmagneter har fyra poler och ett magnetfält vars styrka beror på var i magneten man befinner sig; i mitten av magneten är fältet noll, medan det ökar linjärt med avståndet från centrum. Fältet är riktat så att partiklar antingen böjes av in mot eller ut från centrum. Eftersom styrkan på fältet avtar ju närmare centrum partikeln hamnar och byter riktning på andra sidan centrum, så leder det till en transversell fokusering eller defokusering av strålen. En kvadrupolmagnet fokuserar alltid i ena planet och defokuserar i andra. Om man kombinerar flera kvadrupolmagneter, roterade 90 grader i förhållande till varandra, kan man dock hålla strålen transversellt fokuserad i båda planen.

RF-kaviteterna är en form av kaviteter som strålen färdas igenom. Till dessa kopplar man växelspänning med en frekvens inom radio-området, därav namnet. Detta leder till en spänningsskillnad mellan början av kaviteten, där strålen åker in, och slutet av kaviteten, där strålen åker ut. När en partikel befinner sig i kaviteten så ser den därmed ett elektriskt fält, vilket kan accelerera partikeln om den är korrekt synkroniserad med frekvensen på växelspänningen.

Den underliggande fysiken kallas för *acceleratorfysik* och beskriver hur strålen och dess egenskaper påverkas av de olika ingående komponenterna. Under normala förhållanden så kommer strålen att ligga på en viss bestämd omloppsbana, som är periodisk och därmed sluter sig själv. Detta är den *stängda omloppsbanan*. Tittar man på enskilda partiklar i strålen så ser man dock att dessa oscillerar runt denna bana. Det är här kvadrupolmagneterna kommer in; partiklarna i strålen tenderar att divergera bort från strålens centrum, men dessa magneter böjer tillbaka partiklarna in mot centrum. Prob-

lemet är dock att det ger dem en transversell hastighet så att de åker förbi centrum, och sedan ut mot andra sidan, varifrån de sedan fokuseras tillbaka in igen. De beter sig alltså ungefär som en fjäder, som oscillerar upp och ned utan att stanna vid centrum. Detta kallas för *betatron-oscillationer*, och ger strålen en viss utbredning, en viss storlek. Storleken kan moduleras utefter acceleratorn med hjälp av olika kvadrupolmagneter.

Dipolmagneter fungerar lite annorlunda. Eftersom de har ett homogent magnetfält, så ser alla partiklar i strålen samma fält och påverkas därmed på samma sätt. Om man tänker sig att man har en dipolmagnet igång under bara ett varv, så kommer hela strålen att böjas av lite från den stängda omloppsbanan. Likt de enskilda partiklarna så kommer då hela strålen i sig att genomgå betatron-oscillationer runt deras ursprungliga omloppsbana. Detta liknar det som kan hända vid ett fel; först beräknar man det elektriska och/eller magnetiska fält som felet ger upphov till. Sedan kan man beräkna hur strålens bana, eller andra parametrar som dess storlek, påverkas *i förhållande till* den stängda omloppsbanan. Utifrån detta kan man beräkna att strålen tex börjar oscillera med en viss amplitud, vilket man kan jämföra med kollimatoröppningarna för att beräkna hur stor andel av strålen som kommer att träffa dem, och därmed absorberas av kollimatorsystemet.

Large Hadron Collider

Large Hadron Collider (LHC) vid CERN i Genève är med en omkrets på nästan 27 km världens största accelerator. Den har även de mest energetiska partiklarna, protoner som accelereras upp till sju teraelektronvolt (TeV). Detta motsvarar energin som en enkelt laddad partikel får om den accelereras över en spänningsskillnad på sju teravolt. För protoner motsvarar detta en hastighet på $99,9999991\%$ av ljusets hastighet. LHC har två vakuumrör, med två motgående strålar. Vid fyra ställen korsar dessa rör varandra så att strålarna kan kollidera med varandra. Dessa ställen, nämnda ATLAS, ALICE, CMS och LHCb, är omgivna av partikeldetektorer stora som hus, vars syfte är att upptäcka det som produceras i kollisionerna.

För att studera fysik bortom Standardmodellen kommer LHC att genomgå en uppgradering fram till 2027, till den så kallade High Luminosity LHC (HL-LHC). Luminositet är ett mått på hur många kollisioner som sker mellan protonerna över tid. Tanken är alltså att maximera antalet kollisioner i LHC, så att man får mer data och bättre möjlighet att hitta ovanliga typer av reaktioner, samt mäta egenskaper hos olika partiklar mer precist. Detta kan leda till observationer som inte kan förklaras av Standardmodellen.

Maskinskydd

En stor utmaning i LHC, och i synnerhet HL-LHC, är att partiklarna i strålarna är väldigt många, i storleksordningen 10^{14} protoner, som alla har en hög rörelseenergi. Den totala energimängden som lagras i vardera stråle uppgår därmed till 362 MJ i LHC, eller 678 MJ i HL-LHC. Det senare motsvarar en-

ergin som släppes ut vid en detonation av ungefär 162 kg TNT, en energi som är komprimerad till en millimeter-tunn stråle av protoner. Om strålen i nuvarande LHC skickas mot ett solitt kopparblock, så kan den borra ett 35 m djupt hål. En förlust av blott en bråkdel av strålen kan skada de komponenter som acceleratorn är uppbyggd av, tex de superledande magneter som utgör större delen av konstruktionen. Sådana skador leder både till höga kostnader och långa reparationstider. LHC är unikt i detta att den lagrade energin är så hög, och har därmed varit starkt pådrivande i så kallad "Machine protection", eller maskinskydd.

Maskinskydd omfattar hur man försäkrar att den energi som är lagrad i acceleratorn, både i strålarna och i de elektriska systemen som magneterna, tas om hand om på ett säkert sätt, utan risk för skada på komponenter. Den här avhandlingen har fokuserat på att studera det strålrelaterade skyddet och konsekvenserna av snabba och okontrollerade strålförluster, med fokus på HL-LHC. Det finns en stor uppsättning av så kallade kollimatorer, vars syfte är att avlägsna partiklar med för stor spridning runt strålens centrum. De har därmed små öppningar, de minsta ca 2 mm, och utgör de minsta gapen i hela acceleratorn som strålen färdas igenom. Därmed är kollimatorerna även de objekt som får ta emot merparten av strålförluster när någonting går fel, som tex att strålen inte längre följer sin tänkta omloppsbana. Kollimatorsystemet utgör därmed ett av de mest robusta systemen. Trots det är marginalerna väldigt små, i synnerhet i HL-LHC, där så lite som en förlust av 0.14% av strålen på ett kort tidsintervall kan leda till mekanisk skada i kollimatorsystemet.

Frågan är då vad som kan påverka strålen så att det skapas strålförluster. LHC är en komplicerad maskin, som består av en ofantlig mängd separata komponenter. Tex finns det 1232 dipolmagneter, dvs magneter med ett konstant vertikalt riktat magnetfält, vars syfte är att böja strålens bana i det horisontella planet så att den kan cirkulera acceleratorn. Dessa magneter är superledande och hålles nedkylda till ca 1,9 K, vilket motsvarar ca $-271\,^{\circ}\mathrm{C}$. Om de tappar sin superledande förmåga, något som kallas för en *quench*, så blir de resistiva och börjar förlora den ström som upprätthåller magnetfältet. Strålen kommer då inte längre att böjas tillräckligt varpå den till slut slår i en av kollimatorerna. Händelser som dessa kallas för *failures*, eller fel. Det vill säga, när någon komponent tappar sin avsedda funktion, alternativt något annat oförutsett sker, så att okontrollerade strålförluster uppstår.

Felen kan klassificeras beroende på hur snabbt de kan leda till kritiska strålförluster, långsamma fel är i storlekdsordningen sekunder, snabba fel är snabbare än 10 ms, medan ultrasnabba fel är snabbare än 270 μs. Det senare motsvarar den tid det tar för strålen att cirkulera tre varv i acceleratorn och är även den maximala tid det tar från att ett fel signalerar maskinskyddssystemen att strålarna behöver extraheras, till att båda strålar är extraherade från acceleratorn. Denna process kallas för att strålarna dumpas, varpå de leds ut ur acceleratorn och skjuts mot ett stort robust grafitblock. Dessa två stråldumpar

är de enda delar av LHC som kan hantera strålens fulla energi utan att taga skada.

Olika metoder för att studera felscenarion har tillämpats i detta arbete. För vissa fel räcker det med analytiska beräkningar, där felet ses som en linjär perturbation runt den ordinära stråloptiken. För andra fel har numeriska simuleringar varit nödvändiga, där antingen iterativa analytiska formler används eller där ett simuleringsprogram, MAD-X, används för att även inkludera ickelinjära effekter. För beräkning av strålförluster ses kollimatorerna som svarta absorberare, dvs alla partiklar med en tillräckligt hög transversell oscillationsamplitud anses absorberas direkt av kollimatorerna. Ett flertal felscenarion har även kunnat testas experimentellt i nuvarande LHC, samt i Super Proton Synchrotron (SPS), den mindre accelerator som ligger ett steg före LHC i acceleratorkedjan. Det senare användes för prototyptester av så kallade *krabbkaviteter*.

Exempel på felscenarion

Ett flertal olika felscenarion, relaterat till olika typer av utrustning och strålparametrar har studerats. Magnetskydd utgör bland de mer kritiska felscenariona. Syftet med magnetskydd är att skydda magneterna från skada när de quenchar. Vid en quench så bildas en liten resistiv zon, där strömmen i magneten börjar deponera energi. För att undvika att denna zon överhettas använder man två olika tekniker för att skynda på quenchningen av hela magneten, så att energin kan deponeras över en större volym. Den ena tekniken bygger på resistiva värmeelement som sitter utanpå magneten och kallas för Quench Heaters (QH, "quenchvärmare"). Den andra tekniken kallas för Coupling Loss Induced Quench (CLIQ, "kopplingsförlust-inducerad quench") och bygger på att man skickar in en stark oscillerande ström i magneten, vilket värmer upp hela magnetvolymen. Båda dessa system skapar dock magnetfält i magnetens center, där strålen befinner sig.

Det är ett designkrav att dessa system inte skall kunna aktiveras innan strålarna har extraherats ur acceleratorn. Dessa system måste dock snabbt kunna agera när en quench upptäckes i en magnet, varpå de är anslutna till en kondensatorbank som ständigt hålles uppladdad. Det förekommer således alltid en risk att de aktiveras spontant, vilket även har observerats tidigare i LHC. För CLIQ så innebär en sådan spontan aktivering i värsta fall att merparten av strålen förloras i kollimatorsystemet på så lite som fyra varv (ca $360\,\mu$s). Det finns inget sätt att skydda acceleratorn vid ett sådant scenario. Istället föreslogs en metod att kraftigt mitigera detta felscenario, genom att ändra kopplingsschemat till magneten. Denna ändring gör att det istället för att skapas ett magnetisk dipolfält där strålen befinner sig, skapas ett oktupolfält, vilka har en mindre inverkan på strålen. Efter mitigering nås skadliga strålförluster först efter 17 varv (ca 1.5 ms). Detta är tillräckligt långsamt för att ett dedikerat system skall kunna upptäcka felet och dumpa strålarna innan skada uppstår.

Angående QHs, så sitter det flera resistiva filmer runt om magneten, och två stycken är alltid kopplade i serie. Vid spontana aktiveringar kan endast en serie med två stycken filmer aktiveras, och beroende på om dessa är kopplade över magnetens tvärsnitt eller inte så blir det inducerade magnetfältet där strålen befinner sig olika starkt. I första hand var således metoden att välja kopplingsscheman som minimerar det magnetfält som strålen ser. Det var dock inte möjligt för samtliga magneter på grund av konkurrerande krav från magnetdesignen. I de senare fallen förekommer några kritiska scenarion där påverkan på strålen riskerar leda till skadliga strålförluster. Givet en viss påverkan på strålens bana genom acceleratorn förloras en viss andel av protonerna i strålen, men eftersom protonerna oscillerar runt centrum av strålen så tar det några varv för alla protoner bortom en viss radie från strålcentrum att förloras. Maskinen kan därmed skyddas genom att dedikerade system för att upptäcka dessa spontana aktiveringar av QH:s installeras, som försäkrar att strålarna med minsta möjliga fördröjning extraheras.

Quenchar i triplet-kvadrupolmagneterna är ett annat kritiskt felscenario. Dessa magneter är en typ av kvadrupolmagneter installerade runt om kollisionspunkterna, vars syfte är att starkt fokusera strålen så att den blir så liten som möjligt i kollisionspunkten. För att få strålen så liten måste den dock bli väldigt stor innan kollisionspunkten, vilket är där triplet-kvadrupolerna befinner sig. Vid positioner i acceleratorn där strålen är stor är effekter på den, som tex den perturbation en magnetquench orsakar, amplifierade. Triplet-kvadrupolerna utgör således bland de mest kritiska komponenterna i LHC. När de quenchar försvagas deras magnetfält, vilket kraftigt påverkar strålens omloppsbana i acceleratorn, så att strålförluster produceras i kollimatorsystemet.

Unidentified falling objects (UFOn) är en typ av event där dammpartiklar kommer in i strålen. Protonerna i strålen interagerar då med dammpartikeln, vilket skapar strålförluster. Dessa strålförluster kan vara så intensiva att de både orsakar automatisk extrahering av strålarna, samt magnetquencher. De har funnits i LHC under flera år och har en stor negativ effekt på tillgängligheten av maskinen. Det är därför viktigt att förstå vad som triggar dessa dammpartiklar, var de kommer ifrån och hur man kan undvika dem. En metod att studera dem utvecklades därmed, som bygger på att med snabba diamantdetektorer mäta strålförlusterna med en hög sampelfrekvens på 650 MHz. Med detta har de första mätningarna av dammpartiklarnas dynamik kunnat utföras, vilket har använts till att validera de teoretiska simuleringsmodellerna.

Ett problem som uppstår vid kollisionspunkterna är den ömsesidiga kraft som strålarna utövar på varandra runt kollisionspunkterna. Vanligtvis är de två motgående strålarna väl separerade i sina egna vakuumrör, men vid kollisionspunkterna går dessa ihop. Eftersom partiklarna i strålarna är laddade så utövar de en repulsiv kraft på varandra. Den inverkan som denna kraft har på strålarnas dynamik genom acceleratorn kompenseras bland annat med hjälp av magneter, så att de följer sina tänkta omloppsbanor. När en stråle dumpas försvinner dock plötsligt denna kraft för den stråle som fortfarande är kvar i

acceleratorn. Borttagningen av denna kraft uppenbarar sig i att strålen börjar oscillera runt sin ursprungliga omloppsbana, vilket kan orsaka strålförluster i kollimatorerna. I nuvarande LHC är denna kraft tillräckligt liten för att inte utgöra något större bekymmer, men i HL-LHC så kommer antalet protoner i strålen att nära på dubbleras. Kraften i sig är proportionell mot antalet protoner i strålen. Detta kommer således att utgöra ett mycket större problem i framtiden.

Så som LHC är utformad i dag kan det dröja ytterligare tre varv för den kvarvarande strålen att dumpas efter den första. I HL-LHC kan kritiska strålförluster dock uppstå redan på andra varvet efter att den första strålen har dumpats. Det är därmed ett krav att tiden mellan att de två strålarna dumpas ej överskrider ett varv ($88.9\,\mu$s). På grund av hur LHC är byggd kan inte strålarna extraheras samtidigt, men inom ett varv är möjligt.

Avslutning

Detta var några exempel på vad som har studerats inom detta arbete. Sammanfattningsvis så har metoderna inom detta arbete möjliggjort kvantifiering av felscenarion och deras konsekvenser för en stor mängd utrustning och varierande strålparametrar. Förslag till mitigeringsstrategier samt krav på implementering av dedikerade förreglingssystem för de mest kritiska scenariona har lagts fram. De mindre kritiska scenariona har också kvantifierats och förreglingsstrategier med existerande system har ansetts vara tillräckliga. Några gränsfall rörande quench heaters och fel som är kombinerade med den perturbation som extraheringen av ena strålen orsakar hos den kvarvarande strålen har upptäckts. Förreglingsstrategier för dessa har lagts fram.

List of abbreviations

ACFCA Crab cavity
ADT Transverse damper
ALICE A Large Ion Collider Experiment
ATLAS A Toroidal LHC ApparatuS
b1 beam 1
b2 beam 2
BBCW Beam-Beam Compensating Wire
BCCM Beam Current Change Monitor
BIC Beam Interlock Controller
BIS Beam Interlock System
BLM Beam Loss Monitor
BPM Beam Position Monitor
CERN Organisation Européenne pour la Recherce Nucléaire, originally Conseil Européen pour la Recherche Nucléaire
CLIQ Coupling Loss Induced Quench
CMS Compact Muon Solenoid
D1 Separation dipole, the first dipole magnet next to an IP
D2 Recombination dipole, the second dipole magnet next to an IP
dBLM diamond Beam Loss Monitor
FMCM Fast Magnet Current Change Monitor
HL-LHC High Luminosity Large Hadron Collider
ICBLM Ionization Chamber Beam Loss Monitor
IP Interaction Point
IR Insertion Region
LBDS LHC Beam Dumping System
LEP Large Electron-Positron collider
LHC Large Hadron Collider
LHC turn Time taken for the beam to circulate the LHC once ($88.9\,\mu$s)
LHCb Large Hadron Collider beauty
LINAC LINear ACcelerator
MAD-X Methodical Accelerator Design, accelerator simulation tool
PIC Power Interlock Controller
PS Proton Synchrotron
PSB Proton Synchrotron Booster
Q1 First Quadrupole magnet next to an IP. One of the final focusing triplet magnets
Q2 Second Quadrupole magnet next to an IP. One of the final focusing triplet magnets

Q3 Third Quadrupole magnet next to an IP. One of the final focusing triplet magnets
Q4 Fourth Quadrupole magnet next to an IP
QH Quench Heater
QPS Quench Protection System
RF Radio Frequency
RHIC Relativistic Heavy Ion Collider
SB Stable Beam
SIS Software Interlock System
SppS Super proton-antiproton Synchrotron
SPS Super Proton Synchrotron
TCDQ Dump absorber
TCP Primary Collimator
TCS Secondary Collimator
TCT Tertiary Collimator
TNT TriNitroToluene
WIC Warm magnet Interlock Controller

Acknowledgements

Four years ago, in September of 2016, I started my doctoral studies. It has been an immensely rewarding time that has taught me a lot. Many people have played a part in realizing this work. Although I find that words are not enough, I would like to take this opportunity to show my appreciation to some of you.

First and foremost, I would like to express my sincerest gratitude to my CERN supervisor Daniel. For entrusting me with this very rewarding and interesting project, for teaching me about machine protection and accelerators, for your guidance throughout these four years and for always making time for me. Thank you!

I thank my University supervisors Roger and Maja, for all the help and support. In particular for providing a different set of eyes on my work, as well as ensuring that my work is understandable to a wider community than the LHC machine protection. You have both been extremely supportive and always made time for me.

I would like to thank Matthieu. You have been a good friend and you have taught me not only accelerator physics, but also helped me become more professional in my work. I sincerely hope that our paths will cross again.

Thank you Philippe, for being a friend and for all your insightful discussions and work on UFOs. I hope to see you at CERN or TRIUMF in the near future.

Andy, thanks a lot for all the nice lunches and discussions outside of work and for showing me your experiments. I wish you the best of luck in preparation for your own defense!

To my colleagues and friends at CERN; Andrea, Anton, Arjan, Christoph, Dimitri, Emmanuele, Karolina, Laura, Lorenzo, Martyna, Mika, Milan, Rudiger. Thank you for all the support with my work and for teaching me about your work. And especially for all the activities outside of work!

All my good friends at CERN, Adam, Alexey, Andrea, Foteini, Kyrre, Miriam, Nikos, Tobias, Veronika, Viktor. Thank you for all the support and for all our interesting discussions about a plenitude of things. My time at CERN would not have been the same without you. I hope to see you all in R1 again.

To all my friends I met at USPAS, Annie, Braulio, Ceci, Davide, Ian, Jorge, Maria. Thank you! USPAS is very enriching and you learn a lot, but it is stressful. Thanks to you it was a lot of fun, making the studying easier. The accelerator community is small, so we will surely meet again before long.

Although my time at Uppsala University was brief, the group here was very welcoming and everyone has been very nice. Thank you Alan, Jim, Jonas,

Max, Mikael, Myrto, Olga, Thomas, Venugopal! A special thanks to my office mates Georgii and Michael, for all the interesting discussions.

Till mina föräldrar. Det var ni som tog mig in på den akademiska banan, och även om jag höll mig undan från Medicin så blir jag åtminstone doktor. Victor, Gustaf och mormor, tack för all er hjälp genom åren.

Tack även till min svärfamilj, Eiji, Kiyoko, Asako, Eiichirou, Yuusaku och Miharu. För ert förtroende och stöd.

Slutligen vill jag tacka min familj. Haruna, Nathan och Felicia. Jag är oerhört tacksam för ert stöd, er förståelse, ert outtömliga tålamod, och framför allt för att ni finns. Det här arbetet är dedikerat till er.

Bibliography

[1] H. Geiger and E. Marsden, "On a diffuse reflection of the α-particles", *Proceedings of the Royal Society of London. Series A, Containing Papers of a Mathematical and Physical Character*, vol. 82, no. 557, pp. 495–500, 1909, ISSN: 09501207. [Online]. Available: http://www.jstor.org/stable/93004.

[2] E. Rutherford, "The scattering of alpha and beta particles by matter and the structure of the atom", *Phil. Mag. Ser. 6*, vol. 21, pp. 669–688, 1911. DOI: 10.1080/14786440508637080.

[3] H. Nagaoka, "Lv. kinetics of a system of particles illustrating the line and the band spectrum and the phenomena of radioactivity", *The London, Edinburgh, and Dublin Philosophical Magazine and Journal of Science*, vol. 7, no. 41, pp. 445–455, 1904. DOI: 10.1080/14786440409463141.

[4] G. Ising, "Prinzip einer Methode zur Herstellung von Kanalstrahlen hoher Voltzahl", *Ark. Mat. Astron. Fys.*, vol. 18, no. 30, pp. 1–4, 1924. [Online]. Available: https://cds.cern.ch/record/433984.

[5] R. Wideroe, "Uber ein neues Prinzip zur Herstellung hoher Spannungen", PhD thesis, Aachen, Tech. Hochsch., 1927. DOI: 10.1007/BF01656341.

[6] E. O. Lawrence and M. S. Livingston, "The production of high speed light ions without the use of high voltages", *Phys. Rev.*, vol. 40, pp. 19–35, 1 1932. DOI: 10.1103/PhysRev.40.19.

[7] *Cyclotron Produced Radionuclides: Physical Characteristics and Production Methods*, ser. Technical Reports Series 468. Vienna: International Atomic Energy Agency, 2009, ISBN: 978-92-0-106908-5. [Online]. Available: https://www.iaea.org/publications/7892/cyclotron-produced-radionuclides-physical-characteristics-and-production-methods.

[8] K. Ziegler, "Material Research with Beams at Cyclotron Energies", in *13th International Conference on Cyclotrons and Their Applications*, Mar. 1993, p. IV01.

[9] H. G. Blosser, "Medical Cyclotrons", *Phys. Today*, vol. 46N10, pp. 70–73, 1993. DOI: 10.1063/1.881366.

[10] E. McMillan and P. H. Abelson, "Radioactive element 93", *Phys. Rev.*, vol. 57, pp. 1185–1186, 12 1940. DOI: 10.1103/PhysRev.57.1185.2.

[11] G. T. Seaborg, A. C. Wahl, and J. W. Kennedy, "Radioactive element 94 from deuterons on uranium", *Phys. Rev.*, vol. 69, pp. 367–367, 7-8 1946. DOI: 10.1103/PhysRev.69.367.

[12] V. Veksler, "A new method for accelerating relativistic particles", Russian, *Dokl. Akad. Nauk SSSR*, 1944. [Online]. Available: http://elib.biblioatom.ru/text/veksler_2003/go,68/.

[13] *LHC design report. Vol. 1.* Geneva: CERN, 2004, (the LHC Collaboration), ISBN: 978-92-9083-224-9.

[14] CUSH, *Standard model of elementary particles*. [Online]. Available: https://commons.wikimedia.org/wiki/File:Standard_Model_of_Elementary_Particles.svg.

[15] "Observation of the top quark", *Phys. Rev. Lett.*, vol. 74, pp. 2632–2637, 1995, (the D0 collaboration). DOI: 10.1103/PhysRevLett.74.2632. arXiv: hep-ex/9503003.

[16] "Observation of top quark production in $\bar{p}p$ collisions", *Phys. Rev. Lett.*, vol. 74, pp. 2626–2631, 1995, (the CDF collaboration). DOI: 10.1103/PhysRevLett.74.2626. arXiv: hep-ex/9503002.

[17] "Observation of tau neutrino interactions", *Phys. Lett. B*, vol. 504, pp. 218–224, 2001, (the DONUT collaboration). DOI: 10.1016/S0370-2693(01)00307-0. arXiv: hep-ex/0012035.

[18] "Observation of a new particle in the search for the standard model higgs boson with the ATLAS detector at the LHC", *Physics Letters B*, vol. 716, no. 1, pp. 1 –29, 2012, (the ATLAS collaboration), ISSN: 0370-2693. DOI: https://doi.org/10.1016/j.physletb.2012.08.020.

[19] "Observation of a new boson at a mass of 125 GeV with the CMS experiment at the LHC", *Physics Letters B*, vol. 716, no. 1, pp. 30 –61, 2012, (the CMS collaboration), ISSN: 0370-2693. DOI: https://doi.org/10.1016/j.physletb.2012.08.021.

[20] "High-Luminosity Large Hadron Collider (HL-LHC): Technical Design Report V. 0.1", in, ser. CERN Yellow Reports: Monographs. Geneva: CERN, 2017, (the HL-LHC Collaboration). DOI: 10.23731/CYRM-2017-004.

[21] N. A. Tahir, B. Goddard, V. Kain, R. Schmidt, A. Shutov, *et al.*, "Impact of 7 TeV large hadron collider proton beam on a copper target", *Journal of Applied Physics*, vol. 97, no. 8, p. 083 532, 2005. DOI: 10.1063/1.1888031.

[22] N. Tahir, R. Schmidt, A. Shutov, I. Lomonosov, A. Piriz, *et al.*, "Large Hadron Collider at CERN: Beams generating high-energy-density matter", *Physical review. E, Statistical, nonlinear, and soft matter physics*, vol. 79, p. 046 410, May 2009. DOI: 10.1103/PhysRevE.79.046410.

[23] V. Ziemann, *Hands-on accelerator physics using MATLAB*. Boca Raton, FL: CRC Press, 2019. DOI: 10.1201/9780429491290. [Online]. Available: https://cds.cern.ch/record/2666607.

[24] M. Conte and W. W. MacKay, *An introduction to the physics of particle accelerators; 2nd ed.* Singapore: World Scientific, 2008. [Online]. Available: https://cds.cern.ch/record/1093376.

[25] S. Peggs and T. Satogata, *Introduction to accelerator dynamics*. Cambridge: Cambridge University Press, 2017. DOI: 1107132843. [Online]. Available: http://cds.cern.ch/record/2266082.

[26] R. D. Maria, R Bruce, D Gamba, M Giovannozzi, and F Plassard, "High Luminosity LHC Optics and Layout HLLHCV1.4", *Proceedings of the 10th Int. Particle Accelerator Conf.*, p. 4, 2019.

[27] E. Mobs, *The CERN accelerator complex - 2019. Complexe des accelerateurs du CERN - 2019*, General Photo, 2019. [Online]. Available: https://cds.cern.ch/record/2684277.

[28] M. Barnes, M. Benedikt, E. W. Blackmore, A. Blas, J. Borburgh, *et al.*, *The PS complex as proton pre-injector for the LHC: design and implementation report*, ser. CERN Yellow Reports: Monographs. Geneva: CERN, 2000. DOI: 10.5170/CERN-2000-003.

[29] "LHC design report. Vol. 1.", in. Geneva: CERN, 2004, ch. 8, (the LHC Collaboration), ISBN: 978-92-9083-224-9.

[30] R. Bailey and P. Collier, "Standard Filling Schemes for Various LHC Operation Modes", CERN, Geneva, Tech. Rep. LHC-PROJECT-NOTE-323, 2003. [Online]. Available: https://cds.cern.ch/record/691782.

[31] V. Kain, W. Bartmann, B. Mikulec, R. Steerenberg, and J. Wenninger, *Injection protection – are we taking it seriously? How can we make it safer?*, Paper presented at the LHC beam operation workshop, Evian, France, Dec. 2010.

[32] R. Schmidt, R. Assmann, E. Carlier, B. Dehning, R. Denz, *et al.*, "Protection of the CERN Large Hadron Collider", *New Journal of Physics*, vol. 8, no. 11, pp. 290–290, Nov. 2006, ISSN: 1367-2630. DOI: 10.1088/1367-2630/8/11/290.

[33] "LHC design report. Vol. 1.", in. Geneva: CERN, 2004, ch. 18, (the LHC Collaboration), ISBN: 978-92-9083-224-9.

[34] R.W. Assmann, "Collimators and Beam Absorbers for Cleaning and Machine Protection", *Proceedings of the LHC Project Workshop - Chamonix XIV, Chamonix, France*, p. 261, 2005.

[35] R.W. Assmann *et al.*, "The Final Collimation System for the LHC", *Proc. of the European Particle Accelerator Conference 2006, Edinburgh, Scotland*, p. 986, 2006.

[36] R. Bruce, R. W. Assmann, V. Boccone, C. Bracco, M. Brugger, *et al.*, "Simulations and measurements of beam loss patterns at the CERN Large Hadron Collider", *Phys. Rev. ST Accel. Beams*, vol. 17, p. 081 004, 8 2014. DOI: 10.1103/PhysRevSTAB.17.081004.

[37] G. Valentino, G. Baud, R. Bruce, M. Gasior, A. Mereghetti, *et al.*, "Final implementation, commissioning, and performance of embedded collimator beam position monitors in the large hadron collider", *Phys. Rev. Accel. Beams*, vol. 20, p. 081 002, 8 2017. DOI: 10.1103/PhysRevAccelBeams.20.081002.

[38] "High-Luminosity Large Hadron Collider (HL-LHC): Technical Design Report V. 1.0", in, ser. CERN Yellow Reports: Monographs. Geneva: CERN, to be published, ch. 5, (the HL-LHC Collaboration).

[39] B. Todd, "A Beam Interlock System for CERN High Energy Accelerators", Presented on 20 Nov 2006, PhD thesis, 2006. [Online]. Available: http://cds.cern.ch/record/1019495.

[40] D. Kramer, "Design and implementation of a detector for high flux mixed radiation fields", PhD thesis, Technical University of Liberec, Sep. 2008. [Online]. Available: http://cds.cern.ch/record/1139227/files/CERN-THESIS-2008-090.pdf.

[41] D. Belohrad, J. M. Belleman, L. K. Jensen, M. Krupa, and A. Topaloudis, "The LHC Fast Beam Current Change Monitor", *Proceedings of the 2nd Int. Beam Instrumentation Conf.*, p. 4, 2013.

[42] O. Stein, "Ultra Fast Beam Loss Mechanisms at the LHC and their Detection for Use in Machine Protection", PhD thesis, U. Hamburg (main), 2018.

[43] A. Gorzawski, S. Redaelli, N. Fuster Martinez, H. Garcia Morales, A. Mereghetti, *et al.*, "Fast loss analysis with LHC diamond detectors in 2017", no. CERN-ACC-NOTE-2018-0041, 2018. [Online]. Available: https://cds.cern.ch/record/2320644.

[44] E. Ciapala, F. Rodríguez-Mateos, R. Schmidt, and J. Wenninger, "The LHC Post-mortem System", CERN, Geneva, Tech. Rep. LHC-PROJECT-NOTE-303, 2002. [Online]. Available: http://cds.cern.ch/record/691828.

[45] B. Goddard, M. Gyr, J. Uythoven, R. Veness, and W. Weterings, "LHC beam dumping system: Extraction channel layout and acceptance", *Conf. Proc. C*, vol. 030512, p. 1646, 2003.

[46] "LHC design report. Vol. 1.", in. Geneva: CERN, 2004, ch. 17, (the LHC Collaboration), ISBN: 978-92-9083-224-9.

[47] R. Filippini, E. Carlier, L. Ducimetiere, B. Goddard, and J. Uythoven, "Reliability analysis of the LHC beam dumping system", in *Proceedings of the 2005 Particle Accelerator Conference*, 2005, pp. 1201–1203. DOI: 10.1109/PAC.2005.1590707.

[48] F. Rodriguez-Mateos and F. Sonnemann, "Quench heater studies for the LHC magnets", in *PACS2001. Proceedings of the 2001 Particle Accelerator Conference (Cat. No.01CH37268)*, vol. 5, 2001, 3451–3453 vol.5. DOI: 10.1109/PAC.2001.988141.

[49] "LHC design report. Vol. 1.", in. Geneva: CERN, 2004, ch. 9, (the LHC Collaboration), ISBN: 978-92-9083-224-9.

[50] *LHC optics website*. [Online]. Available: https://abpdata.web.cern.ch/abpdata/lhc_optics_web/www/index.html.

[51] N. Karastathis, *Report from the run 3 configuration working group*, presented at the 9th LHC Operations Evian Workshop, 2019.

[52] "High-Luminosity Large Hadron Collider (HL-LHC): Technical Design Report V. 1.0", in, ser. CERN Yellow Reports: Monographs. Geneva: CERN, to be published, ch. 3, (the HL-LHC Collaboration).

[53] "High-Luminosity Large Hadron Collider (HL-LHC): Technical Design Report V. 1.0", in, ser. CERN Yellow Reports: Monographs. Geneva: CERN, to be published, ch. 4, (the HL-LHC Collaboration).

[54] E. Metral, S Antipov, R Appleby, G Arduini, J Barranco, *et al.*, "Update of the HL-LHC operational scenarios for proton operation", CERN, Geneva, Tech. Rep. CERN-ACC-NOTE-2018-0002, 2018. [Online]. Available: https://cds.cern.ch/record/2673544/files/thxa03.pdf.

[55] S. Andrés, K. Artoos, S. Belomestnykh, I. Ben-Zvi, C. Boulware, *et al.*, "Design and vertical tests of double-quarter wave cavity prototypes for the high-luminosity LHC crab cavity system", *Physical Review Accelerators and Beams*, vol. 21, Aug. 2018. DOI: 10.1103/PhysRevAccelBeams.21.082002.

[56] S. D. Silva, J. Delayen, Z. Li, T. Nicol, and H. Park, "Design and Prototyping of a 400 MHz RF-dipole Crabbing Cavity for the LHC High-Luminosity Upgrade", in *Proc. 6th International Particle Accelerator Conference (IPAC'15), Richmond, VA, USA, May 3-8, 2015*, (Richmond, VA, USA), ser. International Particle Accelerator Conference, Geneva, Switzerland: JACoW, 2015, pp. 3568–3571, ISBN: 978-3-95450-168-7. DOI: https://doi.org/10.18429/JACoW-IPAC2015-WEPWI036.

[57] V. Kain, R. Schmidt, and R. Assmann, "Equipment failure and beam losses in the LHC", in *8th European Particle Accelerator Conference (EPAC 2002)*, Jun. 2002, pp. 362–364.

[58] A. Niemi, A. Apollonio, J. Gutleber, P. Sollander, J.-P. Penttinen, *et al.*, "Availability modeling approach for future circular colliders based on the lhc operation experience", *Phys. Rev. Accel. Beams*, vol. 19, p. 121 003, 12 2016. DOI: 10.1103/PhysRevAccelBeams.19.121003.

[59] A. Apollonio, M. Jonker, R. Schmidt, B. Todd, D. Wollmann, *et al.*, "Update on Predictions for Yearly Integrated Luminosity for HL-LHC based on Expected Machine Availability", in *5th International Particle Accelerator Conference*, Jul. 2014, TUPRO015. DOI: 10.18429/JACoW-IPAC2014-TUPRO015.

[60] C. Wiesner, W. Bartmann, C. Bracco, E. Carlier, L. Ducimetière, *et al.*, "Asynchronous Beam Dump Tests at LHC", in *Proceedings of the 9th Int. Particle Accelerator Conf.*, 2018, p. 4.

[61] M. Peyrot, J. M. Rifflet, F. Simon, P. Vedrine, and T. Tortschanoff, "Construction of the new prototype of main quadrupole cold masses for the arc short straight sections of LHC", *IEEE Transactions on Applied Superconductivity*, vol. 10, no. 1, pp. 170–173, 2000. DOI: 10.1109/77.828203.

[62] B. Angerth *et al.*, "The LHC beam screen: Specification and design", in *Proc. 4th European Particle Accelerator Conference (EPAC'94)*, (London, United Kingdom), vol. 940627, 1994, pp. 208–210.

[63] C. Wiesner, L. Bortot, B. Lindstrom, M. Mentink, E. Ravaioli, *et al.*, "LHC MD 3205: Beam Screen Shielding from QH Discharge at 70 K", Tech. Rep., 2020. [Online]. Available: http://cds.cern.ch/record/2706481.

[64] P. Fabbricatore, "Quench and protection of D2 magnet (MBRD) for the high luminosity upgrade of LHC", CERN, Geneva, Tech. Rep. EDMS-2222536, version 1.1, 2019. [Online]. Available: https://edms.cern.ch/ui/#!master/navigator/document?D:100450338:100450338:approvalAndComments.

[65] K. Suzuki, N. Higashi, M. Iida, H. Ikeda, Y. Ikemoto, *et al.*, "Performance of the Quench Protection Heater for the HL-LHC Beam Separation Dipole", *IEEE Transactions on Applied Superconductivity*, vol. 30, no. 4, pp. 1–6, 2020. DOI: 10.1109/TASC.2020.2971458.

[66] E. Ravaioli, B. Auchmann, M. Maciejewski, H. H. J. ten Kate, and A. P. Verweij, "Lumped-Element Dynamic Electro-Thermal model of a superconducting magnet", *Cryogenics*, vol. 80, 346–356. 11 p, 2016, ISSN: 0011-2275. DOI: https://doi.org/10.1016/j.cryogenics.2016.04.004.

[67] L. Bortot, B. Auchmann, I. Cortes Garcia, A. M. Fernandez Navarro, M. Maciejewski, *et al.*, "A 2-D Finite-Element Model for Electrothermal Transients in Accelerator Magnets", *IEEE Transactions on Magnetics*, vol. 54, no. 3, pp. 1–4, Mar. 2018, ISSN: 0018-9464, 1941-0069. DOI: 10.1109/TMAG.2017.2748390.

[68] *Simulation of transient effects in accelerator magnets*, 2019. [Online]. Available: https://espace.cern.ch/steam/_layouts/15/start.aspx/.

[69] L. Bortot, B. Auchmann, I. C. Garcia, A. M. F. Navarro, M. Maciejewski, *et al.*, "STEAM: A Hierarchical Cosimulation Framework for Superconducting Accelerator Magnet Circuits", *IEEE Transactions on Applied Superconductivity*, vol. 28, no. 3, pp. 1–6, Apr. 2018, ISSN: 1051-8223, 1558-2515. DOI: 10.1109/TASC.2017.2787665.

[70] R. Bruce, R. Assmann, L. Lari, and S. Redaelli, *Collimator hierarchy limits: Assumptions and impact on machine protection and performance*, in proceedings of Machine Protection Panel Workshop (2013), Geneva. [Online]. Available: https://indico.cern.ch/event/227895/contributions/477324/.

[71] A. Gomez Alonso, "Most Probable Failures in LHC Magnets and Time Constants of their Effects on the Beam.", Tech. Rep. LHC-Project-note-389, 2006. [Online]. Available: https://cds.cern.ch/record/1003375.

[72] B. Lindstrom and E. Ravaioli, "Analysis of the sequence of events in the RQX.R1 circuit on 3 June 2018", CERN, Tech. Rep., 2018, p. 26. [Online]. Available: https://edms.cern.ch/ui/#!master/navigator/document?D:100208033:100208033:subDocs (visited on 11/28/2019).

[73] C. Zanoni, G. Gobbi, D. Perini, and G. Stancari, "Preliminary Mechanical Design Study of the Hollow Electron Lens for HL-LHC", *Journal of Physics: Conference Series*, vol. 874, p. 012 102, Jul. 2017, ISSN: 1742-6588, 1742-6596. DOI: 10.1088/1742-6596/874/1/012102.

[74] D Mirarchi, H. G. Morales, A Mereghetti, S Redaelli, and J. F. Wagner, "Hollow Electron-Lens Assisted Collimation and Plans for the LHC", in *Proc. 61st ICFA Advanced Beam Dynamics Workshop (HB'18), Daejeon, Korea, 17-22 June 2018*, (Daejeon, Korea), ser. ICFA Advanced Beam Dynamics Workshop, Geneva, Switzerland: JACoW Publishing, 2018, pp. 92–98, ISBN: 978-3-95450-202-8. DOI: doi:10.18429/JACoW-HB2018-TUP1WE02.

[75] E. Gorbatchev, I. Ivanov, V. Kossoukhine, N. Lebedev, V. Melnikov, *et al.*, "Transverse damping systems for the future CERN LHC", in *PACS2001. Proceedings of the 2001 Particle Accelerator Conference (Cat. No.01CH37268)*, vol. 2, Chicago, IL, USA: IEEE, 2001, pp. 1237–1239, ISBN: 978-0-7803-7191-0. DOI: 10.1109/PAC.2001.986639.

[76] W. Höfle and D. Valuch, "Transverse feedback: high intensity operation, AGC, IGC, lessons for 2012", in *Proceedings, 3rd Evian Workshop on LHC beam operation: Evian les Bains, December 12-14, 2011*, 2011, pp. 97–100.

[77] T. Baer, A. Cerutti, N. Ferrari, B. Garrel, E. Goddard, *et al.*, "UFOs in the LHC: Observations, studies and extrapolations", in *Proc. 3rd Int. Particle Acc. Conf.*, May 2012.

[78] S. Rowan, "LHC main dipole magnet circuits: sustaining near-nominal beam energies", Presented 27 Sep 2016, PhD thesis, University of Glasgow, 2016. [Online]. Available: https://cds.cern.ch/record/2229989.

[79] F. Zimmermann, J. T. Seeman, M. Zolotorev, and W. Stoeffl, "Trapped macroparticles in electron storage rings", in *Proceedings Particle Accelerator Conference*, vol. 1, 1995, pp. 517–519.

[80] D. Sagan, "Mass and charge measurement of trapped dust in the CESR storage ring", *Nuclear Inst. and Methods in Physics Research, A*, vol. 330, no. 3, pp. 371–379, 1993, ISSN: 01689002. DOI: 10.1016/0168-9002(93)90566-Z.

[81] H. Saeki, T. Momose, and H. Ishimaru, "Observations of dust trapping phenomena in the TRISTAN accumulation ring and a study of dust removal in a beam chamber", *Review of Scientific Instruments*, vol. 62, no. 4, pp. 874–885, 1991, ISSN: 00346748. DOI: 10.1063/1.1142024.

[82] T. Baer, "Very Fast Losses of the Circulating LHC Beam, their Mitigation and Machine Protection", Presented 25 Nov 2013, PhD thesis, Universität Hamburg, 2013. [Online]. Available: https://cds.cern.ch/record/1637966.

[83] B. Goddard, P. Adraktas, T. Baer, M. J. Barnes, F. Cerutti, *et al.*, "Transient beam losses in the LHC injection kickers from micron scale dust particles", *IPAC 2012 - International Particle Accelerator Conference 2012*, no. May, pp. 2044–2046, 2012.

[84] S. Rowan, A. Apollonio, B. Auchmann, A. Lechner, O. Picha, *et al.*, "Interactions between macroparticles and high-energy proton beams", in *6th International Particle Accelerator Conference, IPAC 2015*, 2015, pp. 2112–2115, ISBN: 9783954501687.

[85] J. P. Koutchouk, "Principle of a Correction of the Long-Range Beam-Beam Effect in LHC using Electromagnetic Lenses", CERN, Tech. Rep., 2000, p. 12.

[86] A. Rossi, Y. Papaphilippou, A. Poyet, and G. Sterbini, "Moving of two wire collimators for BBLR compensation from b2 to b1 on IR1 and IR5", CERN, Geneva, Tech. Rep. EDMS-2054712, version 1.1, 2019. [Online]. Available: https://edms.cern.ch/ui/#!master/navigator/document?D:100586254:100586254:subDocs.

[87] G. Sterbini, S. Fartoukh, N. Karastathis, S. Koustoglou, S. Papadopoulous, *et al.*, *MD results during LHC Run-II & plans for Run-III*, Presented at the 9th HL-LHC collaboration meeting, Oct. 2019. [Online]. Available: https://indico.cern.ch/event/844153/contributions/3544317/attachments/1927473/3191212/2019_wire_HLLHC_GS.pdf.

[88] K. Skoufaris, S. Fartoukh, N. Karastathis, Y. Papaphilippou, D. Pellegrini, *et al.*, "Numerical Optimization of DC Wire Compensation in HL-LHC", in *Proc. 10th International Particle Accelerator Conference (IPAC'19), Melbourne, Australia, 19-24 May 2019*, (Melbourne, Australia), ser. International Particle Accelerator Conference, Geneva, Switzerland: JACoW Publishing, 2019, pp. 570–573, ISBN: 978-3-95450-208-0. DOI: doi:10.18429/JACoW-IPAC2019-MOPMP053.

[89] A. Bertarelli, L. Gentini, M. Pasquali, and P. Pastuszak, *Preliminary hardware design of the Wire BBLRC for HL-LHC*, Presented at the 9th HL-LHC collaboration meeting, Oct. 2019. [Online]. Available: https://indico.cern.ch/event/844153/contributions/3544326/attachments/1928465/3193548/BBLR_Wire_DesignStatus_AB_191017.pdf.

[90] S. Fartoukh, A. Valishev, Y. Papaphilippou, and D. Shatilov, "Compensation of the long-range beam-beam interactions as a path towards new configurations for the high luminosity LHC", *Physical Review Special Topics - Accelerators and Beams*, vol. 18, no. 12, p. 121 001, Dec. 2015, ISSN: 1098-4402. DOI: 10.1103/PhysRevSTAB.18.121001.

[91] K. Nakanishi, Y. Funakoshi, and M Tobiyama, "Beam behavior due to Crab Cavity breakdown", *Proceedings of the 1st Int. Particle Accelerator Conf.*, vol. IPAC2010, p. 3, 2010. [Online]. Available: https://accelconf.web.cern.ch/IPAC10/papers/wepec022.pdf.

[92] R. Calaga, O. Capatina, and G. Vandoni, "The SPS Tests of the HL-LHC Crab Cavities", in *Proc. 9th International Particle Accelerator Conference (IPAC'18), Vancouver, BC, Canada, April 29-May 4, 2018*, (Vancouver, BC, Canada), ser. International Particle Accelerator Conference, Geneva, Switzerland: JACoW Publishing, 2018, pp. 846–849,

ISBN: 978-3-95450-184-7. DOI: doi : 10 . 18429 / JACoW - IPAC2018 - TUPAF057.

[93] A. S. García, "Experiment and machine protection from fast losses caused by crab cavities in the high luminosity LHC", PhD thesis, École polytechnique fédérale de Lausanne, May 2018, p. 193. DOI: 10 . 5075 / epfl-thesis-8533.

[94] M. Valette, L. Bortot, A. Fernandez Navarro, B. Lindstrom, M. Mentink, *et al.*, "Impact of Superconducting Magnet Protection Equipment on the Circulating Beam in HL-LHC", *Proceedings of the 9th Int. Particle Accelerator Conf.*, vol. IPAC2018, 4 pages, 2018. DOI: 10.18429/JACOW-IPAC2018-THPAF062.

[95] A. Priebe, B. Dehning, M. Sapinski, M. Tran, and A. Verweij, "Investigations of quench limits of the LHC superconducting magnets", *Applied Superconductivity, IEEE Transactions on*, vol. 23, pp. 4 701 205–4 701 205, Jun. 2013. DOI: 10.1109/TASC.2012.2236378.

[96] R. Calaga, "Crab Cavities for the High-luminosity LHC", in *18th International Conference on RF Superconductivity*, 2018, THXA03. DOI: 10.18429/JACoW-SRF2017-THXA03.

[97] R. D. Maria *et al.*, "SixTrack Version 5: Status and New Developments", in *Proc. 10th International Particle Accelerator Conference (IPAC'19), Melbourne, Australia, 19-24 May 2019*, (Melbourne, Australia), ser. International Particle Accelerator Conference, Geneva, Switzerland: JACoW Publishing, 2019, pp. 3200–3203, ISBN: 978-3-95450-208-0. DOI: doi:10.18429/JACoW-IPAC2019-WEPTS043.

[98] R. Denz, D. B. Serrano, D. Calcoen, V. Froidbise, S. Georgakakis, *et al.*, "Quench detection and diagnostic systems for the superconducting circuits of the HL-LHC", in *Proceedings of the 10th Int. Particle Accelerator Conf.*, 2019, p. 4.

Acta Universitatis Upsaliensis

Digital Comprehensive Summaries of Uppsala Dissertations from the Faculty of Science and Technology 1993

Editor: The Dean of the Faculty of Science and Technology

A doctoral dissertation from the Faculty of Science and Technology, Uppsala University, is usually a summary of a number of papers. A few copies of the complete dissertation are kept at major Swedish research libraries, while the summary alone is distributed internationally through the series Digital Comprehensive Summaries of Uppsala Dissertations from the Faculty of Science and Technology. (Prior to January, 2005, the series was published under the title "Comprehensive Summaries of Uppsala Dissertations from the Faculty of Science and Technology".)

Distribution: publications.uu.se
urn:nbn:se:uu:diva-426416

ACTA
UNIVERSITATIS
UPSALIENSIS
UPPSALA
2020